1-1-2014

Multiparticle Correlations In Pb--Pb Collisions At \snn=2.76 Tev

Jocelyn Mlynarz
Wayne State University,

MULTIPARTICLE CORRELATIONS IN PB–PB COLLISIONS AT $\sqrt{s_{NN}}$=2.76 TEV

by

JOCELYN MLYNARZ

DISSERTATION

Submitted to the Graduate School

of Wayne State University,

Detroit, Michigan

in partial fulfillment of the requirements

for the degree of

DOCTOR OF PHILOSOPHY

2014

MAJOR: PHYSICS

Approved by:

_____

Advisor Date

_____

_____

_____

_____

DEDICATION

To my dear wife, Karen Stover,

for giving me the courage and strength to see this to the end.

ACKNOWLEDGMENTS

A doctorate is an endeavor that cannot be undertaken in a vacuum, and consequently a great number of people deserve my gratitude for teaching me, advising me and showing me the principles and workings of research in physics in general and relativistic heavy ions in particular. Foremost among these is my advisor, Dr. Sergei Voloshin, who granted me with the knowledge and guidance I needed to advance my research. He gave me the chance to reach this point of my academic career, and I can only hope that I will live up to the full potential of the opportunities that he provided me. In making sure I would be able to finish my research and studies, I am extremely grateful to the departmental chair, Dr. Ratna Naik. I would like to thank my committee members, Drs. Sean Gavin, Claude Pruneau, Robert Harr and Po Hu. I wouldn't have made it this far without their steady supply of advice, suggestions, and caffeine. Sean's office is sometimes called the "Vortex of Procrastination", but in truth a large part of my understanding of the Quark-Gluon Plasma comes from my discussions with him. I hope to keep his friendship in the times to come. I extend my gratitude to professor Dr. Rene Bellwied, who is not only an exceptional teacher but put considerable efforts into making life easier for Graduate Students. For an international student such as me, this sort of help can make all the difference.

In all these years, support came not only from the faculty, but from senior graduate students and post-doctorate fellows as well. My early years in Wayne State would have been more difficult without Drs. Sarah Lapointe and Lawrence Tarrini. Drs. Andrew Blechman and George Moschelli have my gratitude for introducing and maintaining the tradition of 'W Fridays', and my French-British rivalry with Dr. Anthony Timmins have made a few of these years entertaining. I would like to thank Ron Belmont and Rosi Reed for the advice and support they gave me during the writing of this dissertation and the preparation of the associated defense presentation. For helping me through a large number of administrative difficulties, I would like to thank Audrey Rumber and Delores Cowen. Finally, Aditya Yechan-Gunja, Dr. Kristopher Healey, and Dr. Vera Loggins entered the graduate program

about the same time I did and were valuable companions throughout the years, and I would like to thank them and wish them luck in their future endeavors.

TABLE OF CONTENTS

LIST OF TABLES

LIST OF FIGURES

Chapter 1

Introduction: Heavy Ion Collisions and the Quark Gluon Plasma

1.1 The Standard Model and Notions of Symmetry

In the past century, with the introduction of the concepts that characterize modern physics, the physical objects and forces found in our universe have been described as being composed of elementary particles of various properties. The theoretical framework used to model the behavior and interactions of these particles is called Quantum Field Theory (QFT). QFT combines the advances of the earlier special relativity and quantum mechanics. In this framework, particles are quanta (excitations) of fields that interact with each other. The quantum field theory that describes the known elementary particles is called the Standard Model [34]. The Standard Model classifies elemetary particles into two categories. Fermions, the particles that compose matter, are caracterized by an intrinsic angular momentum (spin) with a value equal to an half-integer multiple of the reduced planck constant $\hbar$. Fermions obey Fermi-Dirac statistics, which follows from the inability of two fermions to be in the same quantum state. Bosons have integer spin and follow Bose-Einstein statistics. The vectors of the three fundamental interactions described by the model are called gauge bosons. Those three interactions are the electromagnetic interaction, carried by the photon, the weak interaction, carried by the two W-bosons and the Z-boson, and the strong interactions, carried by the gluons. The gravitational interaction is not described by the Standard Model, as attempts to reconcile quantum mechanics and general relativity have not had

experimental verification at this time. The Higgs boson is the result of the Higgs Mechanism, which explains the breaking of the isospin symmetry of the unified electromagnetic and weak (electroweak) interactions. Figure 1.1 shows the elementary particles described by the standard model.

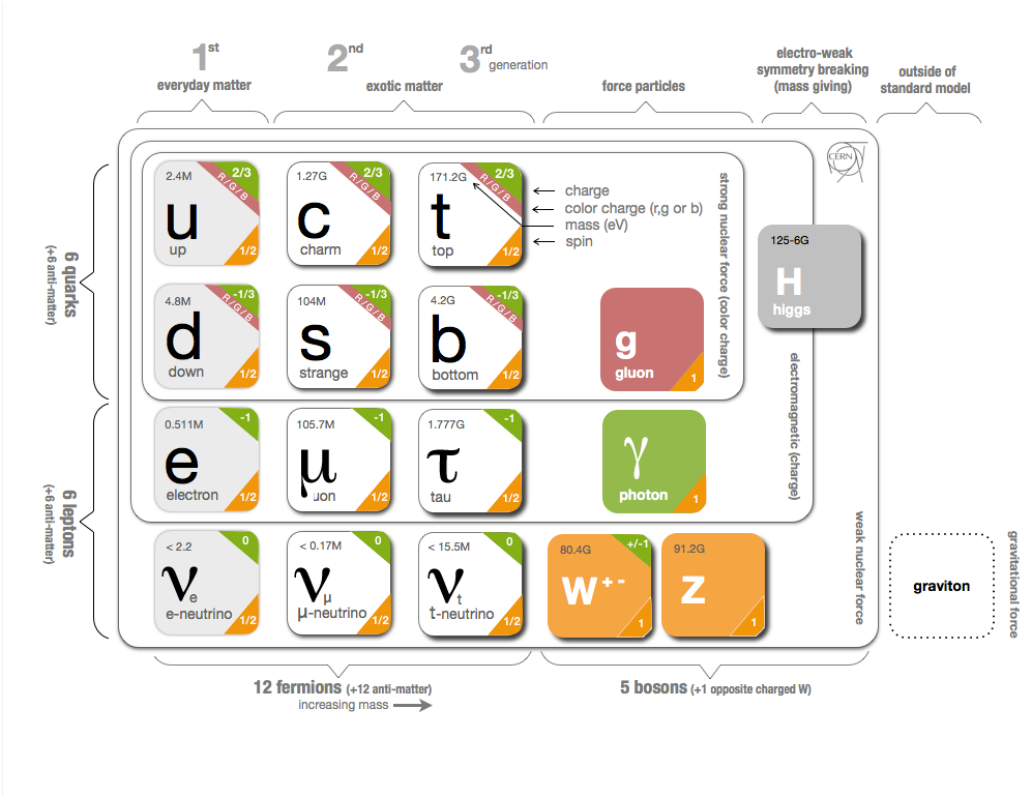

Figure 1.1: Table of fundamental particles as described by the standard model, with the quantum numbers that characterize those particles [1].

Fermions are composed of two families, each including six particles spread in three generations as well as their antiparticles. The first family, leptons, do not participate directly in the strong interaction; it is composed of doublets of the quantum number called weak isospin, with the upper part of the doublets filled by electrons, muons and tau, which can interact via the electromagnetic and potentially weak interactions, depending on their handedness, and the lower parts are filled by their corresponding neutrinos, which are only sensitive to weak interactions. The other family, quarks, is composed of three generations of two quarks. Quarks carry a fractional electric charge and are thus sensitive to the electro-

magnetic interaction; they also participate in the weak and strong interactions.

Interactions between fermions can give rise to situations in which a system of several fermions has lower total energy than if each particle was considered separately; such a system is said to be in a bound state. These bound states constitute the more complex forms of matter that are encountered in particle physics, nuclear physics, and chemistry, e.g. the hundreds of non-fundamental particles, the nuclei, and the atoms.

A core concept of modern physics is the notion of symmetry. Noether's theorem states that to each symmetry of the action describing a physical system corresponds a conserved quantity in that system [35]. The most famous examples are conservation of momentum and conservation of energy, which arise from invariance of the action under space and time coordinate translations, respectively. The mathematical formulation of this theorem is that for a transformation of the coordinates and fields given by

$$\begin{aligned} x^{\mu} &\rightarrow x^{\mu} + \epsilon^{a} A_{a}^{\mu}(x) \\ \phi_{i}(x) &\rightarrow \phi_{i}(x) + \epsilon^{a} F_{i,a}(\phi, \partial\phi) \end{aligned} \tag{1.1}$$

which leaves the action invariant, a being an integer index which can reach arbitrarily high values, there is a conserved current density,

$$j_{a}^{\mu} = \frac{\partial \mathcal{L}}{\partial(\phi_{i,\mu})} \left[A_{a}^{\nu}(x) \phi_{i,\nu} - F_{i,a}(\phi, \partial\phi) \right] - A_{a}^{\mu}(x) \mathcal{L}. \tag{1.2}$$

In Equations 1.1 and 1.2, $\mathcal{L}$ is the Lagrangian density, x^{μ} are the four space-time coordinates, $\phi_{i}(x)$ are the components of a field at point x, A_{a}^{μ} and $F_{i,a}$ are the generators of the transformation and ϵ^{a} are the corresponding parameters.

For instance, the theory describing the interaction of charged particles with the photon field, Quantum Electrodynamics (QED), is modelized by the following Lagrangian (simplified

for only one species of charged particles):

$$\mathcal{L} = \bar{\psi}(i\gamma^\mu D_\mu - m)\psi - \frac{1}{4}F_{\mu\nu}F^{\mu\nu}, \tag{1.3}$$

where the D_μ operator is a shorter notation for $\partial_\mu + iqA_\mu$, ψ is the Dirac spinor field for the charged particles and $F_{\mu\nu} = \partial_\mu A_\nu - \partial_\nu A_\mu$ is the electromagnetic field strength tensor. The local $U(1)$ gauge transformation,

$$\begin{aligned} \psi &\to e^{iq\theta(x)}\psi \\ A_\mu &\to A_\mu - \partial_\mu\theta, \end{aligned} \tag{1.4}$$

leaves the action invariant; applying Equation 1.2 gives a conserved current density vector $j^\mu = \bar{\psi}\gamma^\mu\psi$ and a conserved charge $Q = \int d^3x\psi^\dagger\psi$, which correspond classically to the known electric charge and current conservation laws.

Noether's theorem can be applied to discrete symmetries; in particular, the three symmetries known as time reversal ($x_0 \to -x_0$), parity reversal (in 3 dimensions, $x_i \to -x_i$) and charge conjugation (particle $\to$ antiparticle), noted respectively $\mathcal{T}$, $\mathcal{P}$, and $\mathcal{C}$, are, when conserved by an interaction, associated to conserved quantities. The standard model action is not invariant to parity, time, or charge reversal transformation. The weak interaction sector is known to violate $\mathcal{P}$ and $\mathcal{C}$ as well as the combined $\mathcal{CP}$ transformations, the latter being equivalent to a violation of the $\mathcal{T}$ symmetry. However, a theorem known as the CPT theorem states that Lorentz invariance requires $\mathcal{CPT}$ symmetry. This theorem has so far been confirmed by all experimental evidence.

1.2 The Strong Interaction and Quantum Chromodynamics

The matter composing objects we interact with and observe on a regular basis has been determined to be composed of several successive layers of substructures: molecules composed of atoms, each composed of a nucleus and a cloud of electrons, the former being composed of nucleons (protons and neutrons), and the nucleons being a bound state of quarks exchanging gluons [36]. The electromagnetic interaction cements the two first layers, while nuclei and nucleons are bound by various aspects of the strong interaction.

The nucleon-nucleon interactions that bind the nucleus together are called the nuclear force, or residual strong interaction. The residual strong interaction is an emergent phenomenon that arises from the consequences of the strong interaction. It is modelized by an exchange of pions, rather than gauge bosons, between the nucleons. Pions are massive non-fundamental bosons (i.e., with a substructure and excited states) which are themselves bound states of light quarks. However, the quarks composing a nucleon are directly bound by the strong interaction, which is the interaction of the quark fields and gluon fields. The nucleons contain virtual quark-antiquark pairs, also known as sea quarks, as well as three *valence* quarks [37], the flavor of which determine the type of nucleon. A simplified model represents the nucleon as the result of three *constituent* quarks, which are valence quarks "dressed-up" with the gluons and sea quarks that fluctuate in the nucleon. These features, sea, valence, constituent quarks [38], are generally valid for all other bound states of quarks, called hadrons. Among hadrons, mesons are states composed of one valence quark and one valence anti-quark, and are bosons since they have integer spin, and baryons are the fermionic states composed of three valence quarks or three valence antiquarks with half-integer spin. Quarks and gluons are often collectively named partons.

The theory describing the strong interaction is called Quantum Chromodynamics [39] (QCD). Chromodynamics does not refer to usual concept of color, which is purely in the

electromagnetic sector, but find its origins in the terminology employed to described the strong charges. QCD is an SU(3) gauge theory in which the charge is called *color*. Color can take three values which have been named blue, green, and red.

The QCD Lagrangian is

$$\mathcal{L} = -\frac{1}{4}F_{\mu\nu}F^{\mu\nu} + \bar{\psi}(i\gamma^{\mu}D_{\mu} - me^{i\theta'\gamma_5})\psi. \tag{1.5}$$

A more general form of this Lagrangian would be

$$\mathcal{L} = -\frac{1}{4}F_{\mu\nu}F^{\mu\nu} - \frac{n_f g^2\theta}{32\pi^2}F_{\mu\nu}\tilde{F}^{\mu\nu} + \bar{\psi}(i\gamma^{\mu}D_{\mu} - me^{i\theta'\gamma_5})\psi. \tag{1.6}$$

The θ parameter is usually considered to be null when performing QCD calculations. A non-zero θ would give rise to parity violating effects in QCD, which have not been experimentally demonstrated. However, we choose to include θ it in Equation 1.6 as the analysis described in the future chapters revolve around the search for these parity-violating effects. We will discuss in the next chapter under which conditions the term associated to θ could be non-zero. Calculations based on QCD are complicated by the fact that the perturbative approach, based on a Taylor-like expansion in powers of the coupling constant, is not often applicable in this context. Unlike QED, in which the coupling constant is much smaller than unity, the QCD coupling constant is large, especially at low energies with values on the order of $\alpha_s \sim 1$. Other approaches are often required, such as Lattice QCD, where numerical calculations are performed on a space-time lattice and based on the path integral formalism of quantum field theories.

SU(3) is a non-Abelian group [40], which means that its elements do not systematically commute. In particular, different generators of SU(3) never commute with each other. In QCD, these generators correspond to gluons, which are themselves carriers of the strong charge. This is in contrast with QED, in which photons do not carry the electric charge. Unlike photons, gluons interact directly with each other. Eight gluon eigenstates, corre-

sponding to the generators, exist in QCD, as the color singlet $\frac{1}{\sqrt{3}}\sqrt{\mathrm{b\bar{b}} + \mathrm{g\bar{g}} + \mathrm{r\bar{r}}}$ is not a member of the SU(3) group, e.g. there are no "colorless" gluons. Gluon color charge and the non-Abelian nature of QCD have major consequences in the properties of QCD, the three principals of which are confinement, asymptotic freedom, and chiral symmetry breaking.

When the distance between two quarks, or a quark and an anti-quark, in a hadron increases, color anti-screening arises from the color charges carried by the gluons, increasing the effective charge as distance increases, and creating a field tube between the two quarks. The effective QCD potential increases with distance, and can be approximated as a Coulomb-like term and a linear term [41],

$$V(r) = -\frac{\alpha}{r} + \sigma r, \tag{1.7}$$

known as the Cornell potential, and as a result the further away from each other the quarks are, the stronger the interaction is. "Pulling" the quarks apart requires increasingly more energy until enough energy for a quark-antiquark pair creation is provided, which results in the formation a new hadron. The result is that quarks are confined in bound states with no color charge, and more generally independent color-charged particles cannot be observed.

Similarly to the weak and electromagnetic coupling constants, the renormalized strong coupling constant α_s runs, i.e. it has a dependence on the interaction momentum transfer Q. However, one particularity of QCD, gluon-gluon interactions, give to the coupling constant a logarithmic decrease with energy:

$$\alpha_s = \frac{1}{\beta_0 \ln\left(\frac{Q^2}{\Lambda^2}\right)}, \tag{1.8}$$

where β_0 is a constant based on the number of quark flavors and Λ^2 a cutoff scale. One consequence of this dependence of the coupling constant on the momentum transfer is that at high energy, the regime becomes peturbative and a perturbative expansion approach to QCD calculations becomes effective. Another consequence is the phenomenon called asymptotic freedom; as the energy increases, the coupling constant and thus the interaction strength

decrease; asymptotic freedom is also obtained when the distance between quarks decreases, where the Coulomb-like potential term dominates, and the quarks become quasi-free [42].

Chiral symmetry involves the transformation of the light quark fields,

$$\psi \rightarrow \psi\prime = e^{(i(\alpha\lambda_F/2)\gamma_5)}\psi, \tag{1.9}$$

where $\psi(x) = (u(x), d(x), s(x))$ is the light quark field multiplet, $e^{(i(\alpha\lambda_F/2))}$ performs a flavor rotation and $\gamma_5 = i\gamma_0\gamma_1\gamma_2\gamma_3$. When this transformation is a symmetry of the Lagrangian, the interaction is said to have chiral symmetry. While the interaction term of the QCD Lagrangian is invariant through this transformation, it is not the case of the fermion term:

$$m\bar{\psi}\psi \rightarrow m\bar{\psi}e^{(i(\alpha\lambda_F/2)\gamma_5)}\psi. \tag{1.10}$$

With $m = 0$ this term vanishes and chiral symmetry is a good symmetry of the interaction; the small masses of light quarks mean that this symmetry is broken explicitely, i.e. chiral symmetry is not a symmetry of the QCD Lagrangian. However, experimental evidence, such as masses of hadrons, shows that chiral symmetry is still broken in the limit of vanishing quark masses [43]. In that context, the QCD vacuum state, not the Lagrangian, breaks this symmetry, which is said to be spontaneously broken. In the hot and dense matter created by heavy ion collisions, this symmetry is expected to be restored as the vacuum state would change to another vacuum state that conserves the symmetry with increasing temperature.

1.3 Deconfinement and the Quark-Gluon Plasma

Equation 1.7 and lattice QCD results show that increasing the energy density and temperature of nuclear matter would lower the interaction strength between the quarks bound in a hadron, in effect removing the bound state. A phase transition occurs between a hadronic state of matter where the quarks are confined, and another where quarks are

free and can travel within the partonic medium; we call this phenomenon *deconfinement*. The newly reached state of matter with free quarks is called a Quark-Gluon Plasma (QGP) [44, 45]. The QGP is a state of matter believed to have existed in the first instants of the universe, ending in the first microsecond with the formation of hadrons, called hadronization, as the universe expanded and the quark matter cooled down. The creation of a QGP in a laboratory is sometimes called "little bang" by analogy to the Big Bang. Figure 1.2 shows a chronology of the universe and the times scales at which the QGP phase is assumed to have existed.

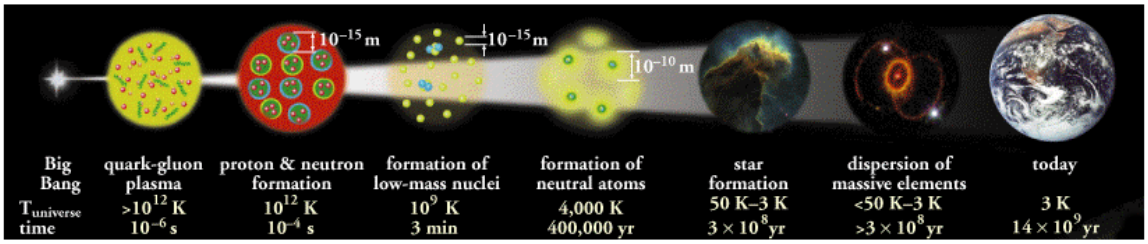

Figure 1.2: Chronology of the early universe, showing the different stages following the big bang and their times scales [2].

Figure 1.3 shows the discontinuity in degrees of freedom, linked to the ratio of the energy density ϵ to T^4, at a certain critical temperature T_c, based on lattice QCD caclulations. This type of discontinuity is characteristic of a phase transition, and the Quark-Gluon Plasma constitutes the phase above that critical temperature. The degrees of freedom are hadronic before the phase transition, and partonic beyond it.

Following the introduction of the concept of phase transitions for nuclear and quark matter, by analogy with the phase transitions of matter around the standard conditions of temperature and pressure, we can explore the phase diagram of nuclear matter over the broad range of temperatures and chemical potential or density that can be found in various contexts such as particle physics experiments or stellar phenomena [46]. This phase diagram is depicted on Figure 1.4. Indicated on this diagram are the results from the energy scan

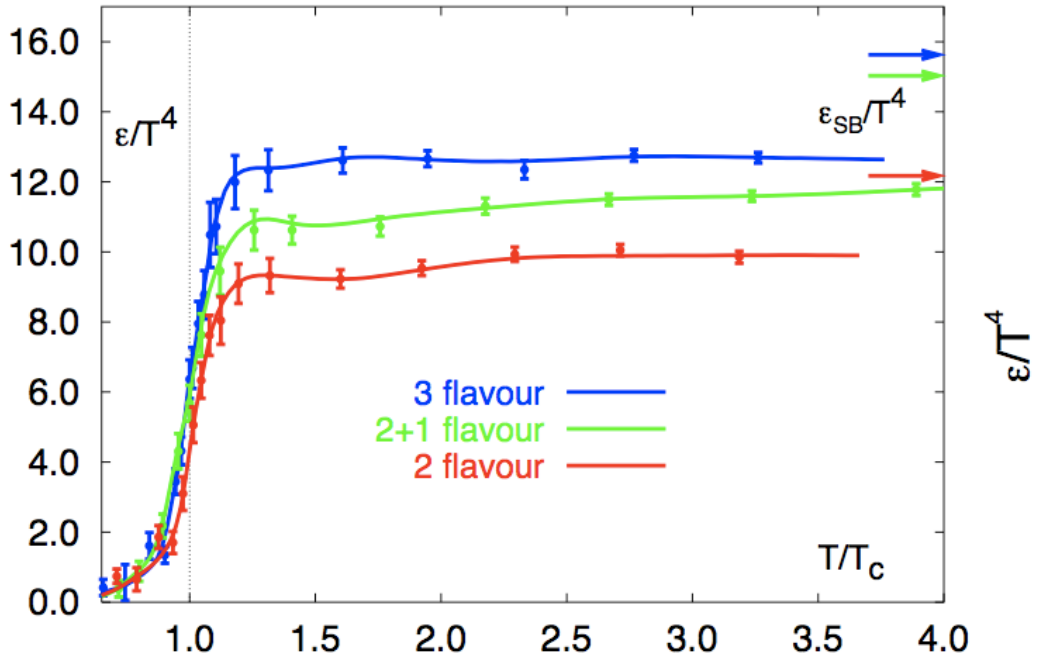

Figure 1.3: The energy density/temperature ratio as a function of temperature in units of the critical temperature T_c, calculated from lattice QCD with staggered fermion action; this is an approximation of the number of degrees of freedom in the medium, and characteristic of a phase transition. This Figure was obtained from [3].

performed by the Relativistic Heavy Ion Collider (RHIC) in the search for the critical point as well as the chemical freezeout temperature, which could be approximated at the phase transition boundary. Chemical freezeout is defined as the stage at which inelastic collisions cease (i.e., when the composition of the system is fixed outside of potential future decays of short-lived resonances), as opposed to kinetic freezeout which is the stage when elastic collisions cease [47]. The lower-right side of the phase diagram, while somewhat out of the scope of relativistic heavy ion collisions and QGP physics, is also an interesting field of investigation, particularly in astrophysics. The "low"-temperature/high-chemical potential region of the diagram is indeed believed to correspond to the matter found in neutron stars.

The Quark-Gluon Plasma is believed to have been obtained and observed on a regular basis in the last fifteen years in ultrarelativistic heavy ion experiments such as the ones performed at RHIC (a collider that specializes in the search for the QGP) and the Large

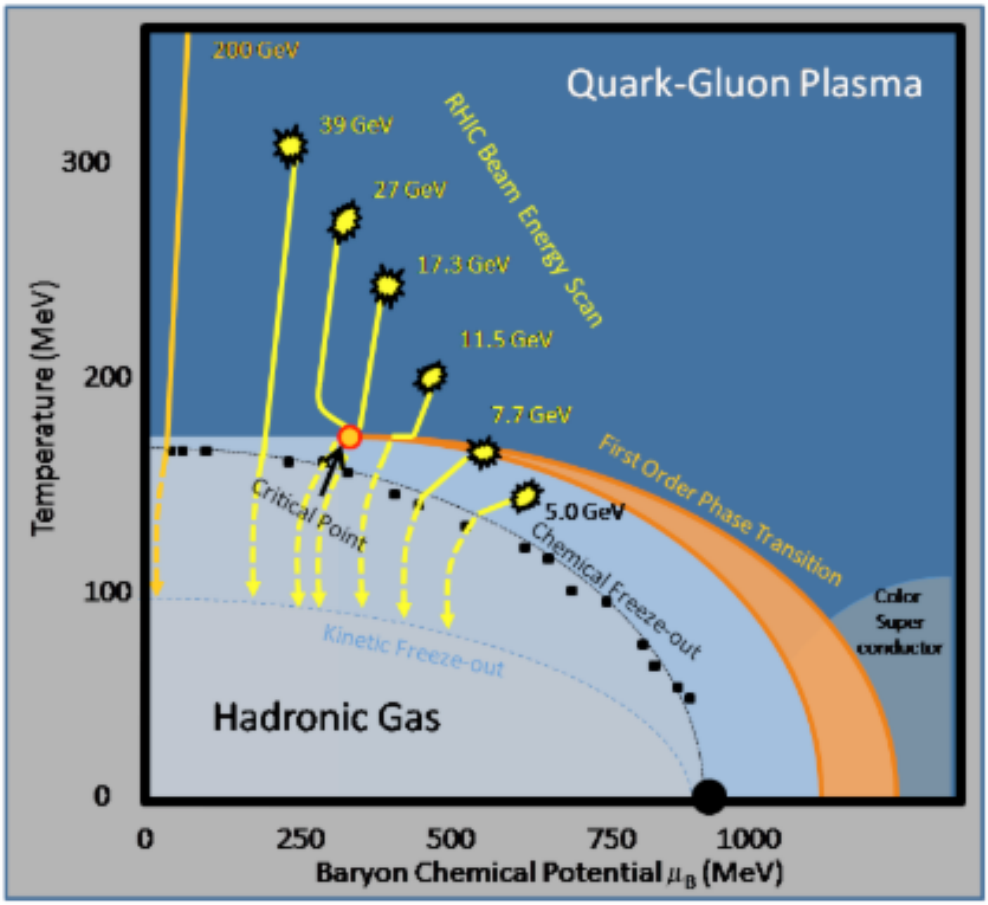

Figure 1.4: The various phases of nuclear matter over a large range of conditions, as a function of energy and density [4].

Hadron Collider (LHC). In these experiments, heavy nuclei corresponding to elements with atomic mass around 200 are accelerated at velocities close to the speed of light, giving them center of mass energies per nucleon pair that can range from tens of GeV to a few TeV. Usually, experiments at RHIC are performed with gold (Au) nuclei accelerated to $E_{\text{beam}} = 100$ GeV and the LHC heavy ion program of 2010 and 2011 used lead (Pb) nuclei accelerated at $E_{\text{beam}} = 1.38$ TeV. Many other center of mass energies have been used at RHIC during the aforementioned energy sweep and for comparison purposes, and other nuclei (protons, deuterons, copper) are sometimes used in symmetrical (A–A) or asymetrical (p–A/d–A) collisions. Recently, experiments involving uranium (U) nuclei have been performed to take advantage of their non-spherical shapes and study the changes in QGP properties

that ensued for the newly obtained collision symmetries [48, 49, 50].

Figure 1.5 depicts the global picture of a heavy ion collision. The flattened shapes of the nuclei in the laboratory frame are due to the very large lorentz-contraction effects in the center of mass, a result of the nuclei being accelerated at speeds above .9999c. The impact parameter b is defined as the distance between the centers of the nuclei. The quantity named centrality, which estimates the overlap between the nuclei and has a major impact on the properties of the medium created by the collision (size, shape, and other consequences) is closely linked to the impact parameters. In general, smaller impact parameters mean lower centrality *central* collisions) and impact parameters that approach the diameter of a nucleus mean higher centralities, *peripheral* collisions. In order to define centrality more quantitatively, we will have to tie its definition to detector signals in later chapters. The nucleons that interact with the nucleons belonging to the other nucleus are called participants, while the others are called spectators. Central collisions have a large number of participants while in peripheral collisions most nucleons are spectators.

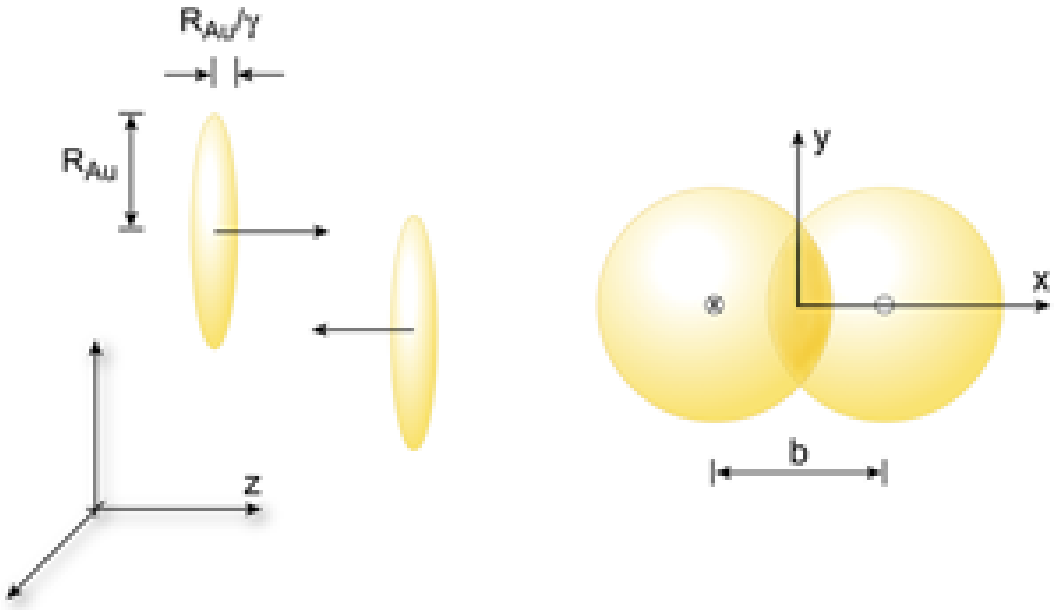

Figure 1.5: The lorentz-contracted nuclei in a non-central heavy ion collision and the definition of the impact parameter [5].

In parallel with the chronology of the big bang shown in Figure 1.2, we can establish a

chronology of the little bang and study the evolution of the system. Figure 1.6 is a light-cone diagram of the evolution of the QGP. In the early stage, the medium created by the collision is not thermalized; as the thermalization takes place, the medium becomes a QGP proper, which then expands under the influence of the very high pressure gradients, and cools down in the process. As the cooling process progresses, the system begins to hadronize, forming first a mixed QGP/hadron phase which becomes a hadron gas, and then crosses the chemical freezeout temperature as the composition of the system is fixed. Finally, kinetic freezeout sets in as the particles' kinetic properties no longer change via elastic collisions. Each of these stages happen at constant proper time [51, 47]. Figure 1.7 shows the same evolution in a cartoon format. It also allows us to understand that it is not possible to observe the QGP directly, as it is very short lived and only the final state particles are collected, long after the QGP has frozen-out. Hence, we will have to use statistical analysis tools and theoretical or phenomenological models to understand the evolution of the system from the partial final state collected by the detectors.

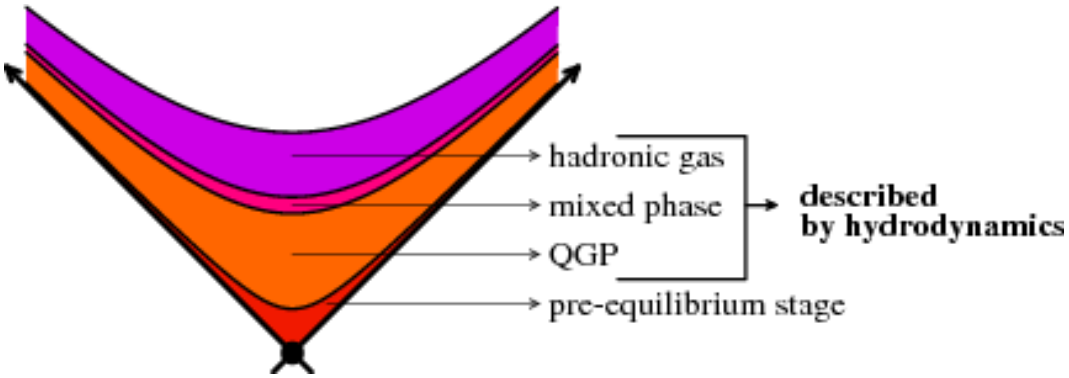

Figure 1.6: Space-time diagram of the evolution of the medium created in ultrarelativistic heavy ion collisions. The boundary between the different phases are located at constant proper time [6].

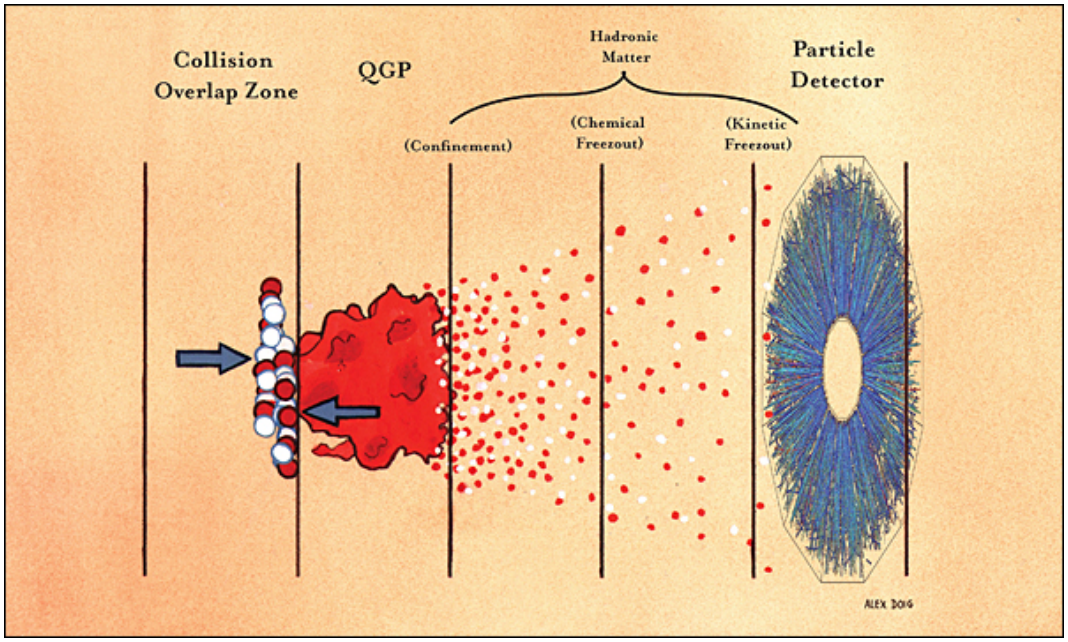

Figure 1.7: The various stages of evolution of the medium created in a heavy ion collision. The system thermalizes to form a QGP, hadronizes until the chemical freezeout, then particle interactions cease at kinetic freezeout and the final particles or their decay products are collected by the detectors [7].

1.4 Main Results from Relativistic Heavy Ion Experiments

In more than a decade of ultrarelativistic heavy ion collision experiments, a large number of seminal experimental results have been obtained by the major collaborations that participate in the research in this field. A large number of properties of the medium have been extracted through analysis, although many questions remain open to this day. Three main categories of results are considered signatures of the Quark-Gluon Plasma. Bulk measurements, via correlation and spectra, bring among other things strong evidence of collective motion. Hard probes use the high-momentum particles created in the medium to probe it, by comparing their characteristics to the ones obtained from scaled *pp* collisions. Resonances can be used to study the yields and spectra of rare particles containing heavy flavors of quarks to extract characteristics of the medium such as temperature.

The bulk consists of low-momentum light quarks and the hadrons they form before freezeout. They are formed through soft interactions of the quarks and gluons from the participant nucleons. The higher transverse momentum limit for hadrons resulting from the bulk is found to be around 1 to 1.5 GeV/c. The bulk includes the vast majority of particles that form the QGP, and the analysis of low-momentum hadrons can give information about the thermodynamic and geometric properties of the system and their evolution. The major points of interest concerning the bulk are the transverse momentum spectra and relative yields of light hadrons and the azimuthal distribution anisotropy in momentum space. The transverse momentum distribution of hadrons at low p_T can be fitted with using a Blast Wave equation or a function obtained from hydrodynamic models, with the fitting degrees of freedom equal to the medium properties (kinetic freezeout temperature, radial expansion rapidity) [52]. The chemical freeze-out can be extracted from the ratios of integrated yields for various particle species [53], based on the fact that heavier hadrons have lower interaction cross-sections and their kinetic freeze-out is closer to the chemical freeze-out (as their kinetic properties vary less after their creation), shown in Figure 1.8. The chemical freeze-out temperature is close to the critical temperature, this indicates that the system underwent a phase transition during its expansion and cooling. Evidence of a thermalized system can be found in the hadron yield ratios. A grand canonical ensemble statistical approach, based upon the assumption of thermal equilibrium, reproduces with good accuracy the ratios found in the ultrarelativistic heavy ion experiments [54]. Finally, the study of particle correlations between low transverse momentum hadrons has provided another major result, evidence of collective phenomena based on the azimuthal anisotropy in momentum distributions, the anisotropic flow. The underlying idea is that in a medium composed of weakly interacting particles, when one pictures each point of the medium as a source of hadrons, each of these points would radiate these hadrons isotropically. No matter what the initial geometry of the system and other initial condition considerations, the final distribution for a given value of p_T (scalar) would be independent of the azimuthal angle modulo fluctuations due to

the finite multiplicity. However, in a strongly interacting medium with steep gradients of pressure in the transverse plane, particles would be pushed by the flowing fluid and the directions of hadrons coming from the same source would be correlated from having received a push in the same direction. In this picture, an initial geometrical anisotropy in the system such as the "almond shape" obtained from non-central collisions (Figure 1.9) translates into an anisotropy in momentum space, as the different values of pressure gradients gives rise to different push rapidities at different azimuthal angles. The study of anisotropic flow is performed via the Fourier expansion of the the particle distribution in momentum space [55]:

$$E\frac{d^3N}{dp_T^3} = \frac{dN^2}{2\pi p_T dp_T dy}\left(1 + \sum_{i=0}^{\infty} v_i \cos\left(n\left(\phi - \psi\right)\right)\right). \tag{1.11}$$

In this equation, ϕ denotes the azimuthal angle, N the number of particles, y is the rapidity along the z-axis and ψ is a reference angle tied to the geometry of the collision, called the reaction plane. The reaction plane is defined by the beam axis and the line that goes through the center of the nuclei (from which the impact parameter is determined). The moments of this Fourier expansion, the v_i coefficients, give information about the system's reaction to the initial conditions, which in turn gives insight into the properties of this system, such as its viscosity. There are notable names given to the four first coefficients of this expansion: directed flow (v_1), elliptic flow (v_2), triangular flow (v_3) and quadrangular flow (v_4). It is worth noting that in the definition given above, the v_i coefficients do not exactly describe flow, i.e. collective motion, as the Fourier coefficients also include non-flow effects. However, colloquially, we will refer to the various components of flow using these coefficients. One notable result from RHIC is the discovery of strong elliptic flow, in addition to a strong mass ordering of v_2. At constant p_T, hadrons of higher mass have lower elliptic flow (Figures 1.10 and 1.11). Figure 1.12 shows evidence of quark scaling [11], in which at low and medium transverse momentum the elliptic flow of hadrons scaled by the number of constituent quarks is identical, and is explained by low-momentum hadron formation via coalescence of flowing

constituent quarks that combine their momenta in the final hadron; this provides further evidence of collective motion. Hydrodynamic models [56, 51] provide a very good description of these aspects of the medium created in relativistic heavy ion collisions. In essence, this medium behaves like a perfect liquid, with a very low shear viscosity to entropy density ratio η/S, very close to the minimal value allowed by quantum mechanics. Strong pressure gradients are found in the medium, and their magnitude is higher along the reaction plane than perpendicular to it, the opposite of the initial space anisotropy. This is evidence that the system is strongly coupled and particles in this medium have a short mean free path. Higher moments of the Fourier expansion are used to study the finer details of spatial anisotropy and reconstruct initial conditions.

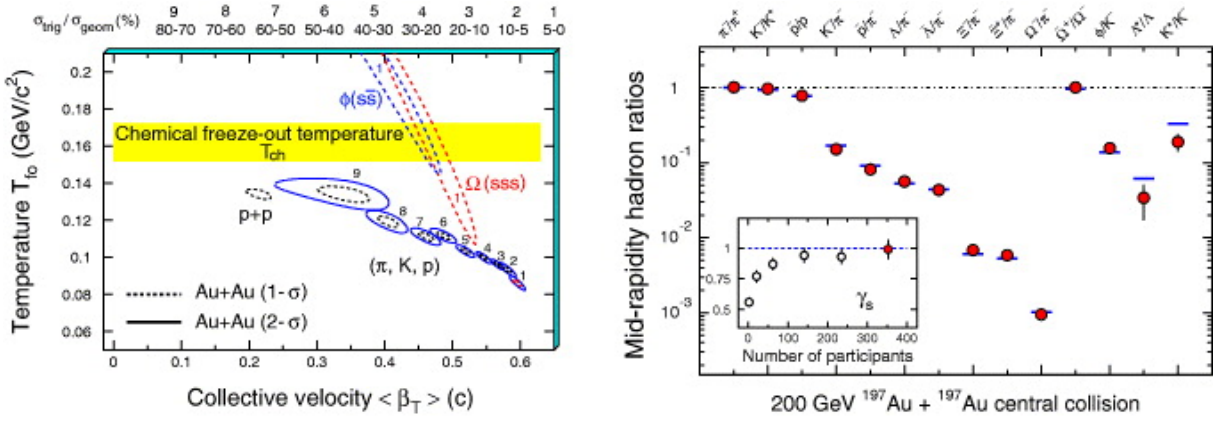

Figure 1.8: Left: Kinetic freeze-out temperature and collective velocity obtained from blast-wave model fits to data based on Au+Au collisions at $\sqrt{s_{NN}} = 200$ GeV. Right: ratios of various hadron species obtained from data based on Au+Au collisions at $\sqrt{s_{NN}} = 200$ GeV, with comparison to thermal models [8].

Hard probes consist of the high-momentum particles created in parton-parton hard scattering in the initial stages of the collision. There are much fewer high-momentum particles than particles belonging to the bulk. The idea behind hard probes is to look at the influence of the medium on the characteristics of high-momenta particles, generally by comparing observables based on these particles in pp, asymetrical (p/d–A) and A–A collisions. The two major results obtained from high-momentum hadrons are the high-$p_T$supression (nuclear modification factor) and jet quenching. The nuclear modification factor R_{AA} is

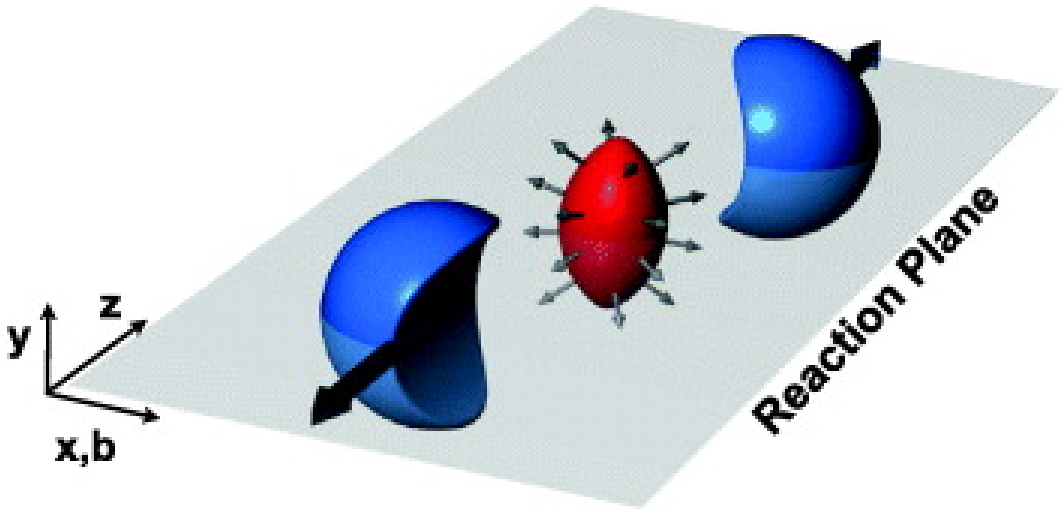

Figure 1.9: Sketch of a heavy ion collision showing the reaction plane and the initial spatial anisotropy of the system. This anisotropy, coupled with the strongly interacting nature of the medium, gives rise to anisotropic flow [9].

defined as:

$$R_{\mathrm{AA}} = \frac{\frac{d^2 N_{\mathrm{AA}}(p_T)}{dp_T dy}}{N_{\mathrm{coll}} \frac{d^2 N_{\mathrm{pp}}(p_T)}{dp_T dy}} = \frac{\sigma_{\mathrm{AA}}}{N_{\mathrm{coll}} \sigma_{\mathrm{pp}}}. \tag{1.12}$$

In Equation 1.12 N_{coll} is the number of independent nucleon-nucleon collisions in a heavy ion collision, $N_{\mathrm{pp}}(p_T)$ the number of particles with transverse momentum p_T in a pp collisions and $N_{\mathrm{AA}}(p_T)$ the corresponding number in a heavy ion event. A heuristic way to understand R_{AA} is as a comparison between the number of high-momentum particles that traversed the medium created by a heavy ion collision (numerator) and the number of high-momentum particles created in a pp-collision scaled by the number of binary nucleon-nucleon collision in the heavy ion event. The same number of such particles should have been initially created, but it is expected that in the heavy ion collisions, these particles would interact with the medium and lose their energy and momentum. Figure 1.13 shows the experimental results for this quantity at RHIC. A strong suppression of high-momentum particles is observed, indicating that they interact with the medium and deposit a significant amount of their energy, indicative of a strongly coupled medium.

High p_T partons from hard-scattering processes produce jets, a phenomenon where the

parton hadronizes by fragmenting into a cone of hadron. Conservation of momentum dictates that in pp collision, jets are produced in back-to-back pairs, called dijets. In heavy ion collisions, since the high-momentum particles have to travel through a strongly interacting medium, some of the momentum can be lost by gluon bremsstrahlung. In the case of jets formed deeper within the medium, both of the jets could be strongly affected, and would either not be found during analysis or be found with a broadening of the cone and lower total energy; jets created in the surface would be less affected but the opposing jet would lose energy to the medium [13]. The experimental result is a disappearance of the back-to-back correlations of high-$p_T$particles normally found in pp collisions as shown in Figure 1.14.

Other notable results include the suppression of heavy resonances such as J/ψ, which is described by the "melting" of these resonances in the QGP. The results are consistent with a QGP temperature around 170 MeV at RHIC [57].

1.5 Thesis Outline

This thesis will discuss two-particle correlations with respect to the reaction plane in an effort to provide evidence for the Chiral Magnetic Effect (CME) and CP-violation in the strong sector as described in chapter 2. It focuses on the estimation of the background effects from local charge conservation using an observable sensitive to these effects but not to the CME. The measurements are based on ALICE Pb+Pb collisions at $\sqrt{s_{NN}} = 2.76$ TeV. The chapter 7 shows a comparison of results with blast wave model calculations.

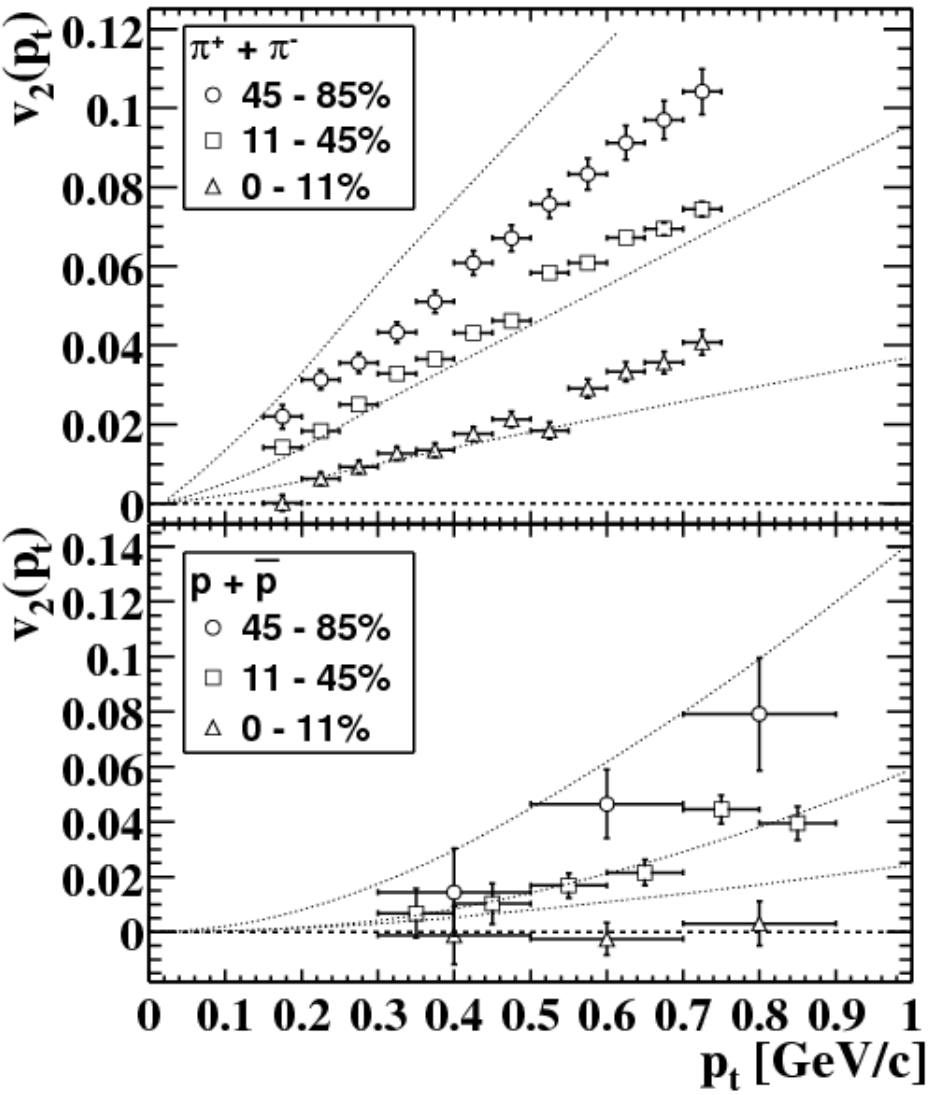

Figure 1.10: Pion (higher panel) and proton (lower panel) differential elliptic flow in $\sqrt{s_{NN}} =$ 130 GeV Au+Au collisions calculated for three different centrality bins. The doted lines are based on caclulations performed with a full hydrodynamical model [10].

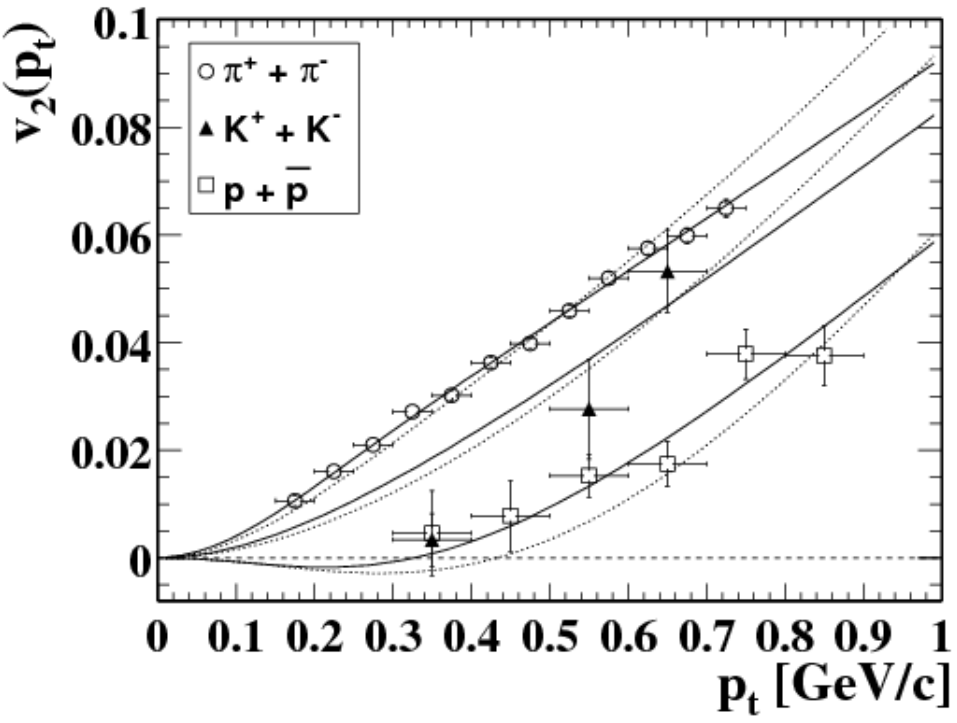

Figure 1.11: Differential elliptic flow calculated for pions, protons and Kaons in $\sqrt{s_{NN}} = 130$ GeV Au+Au collisions. Modified (dotted) and unmodified (solid) blast-wave calculations are also shown [10].

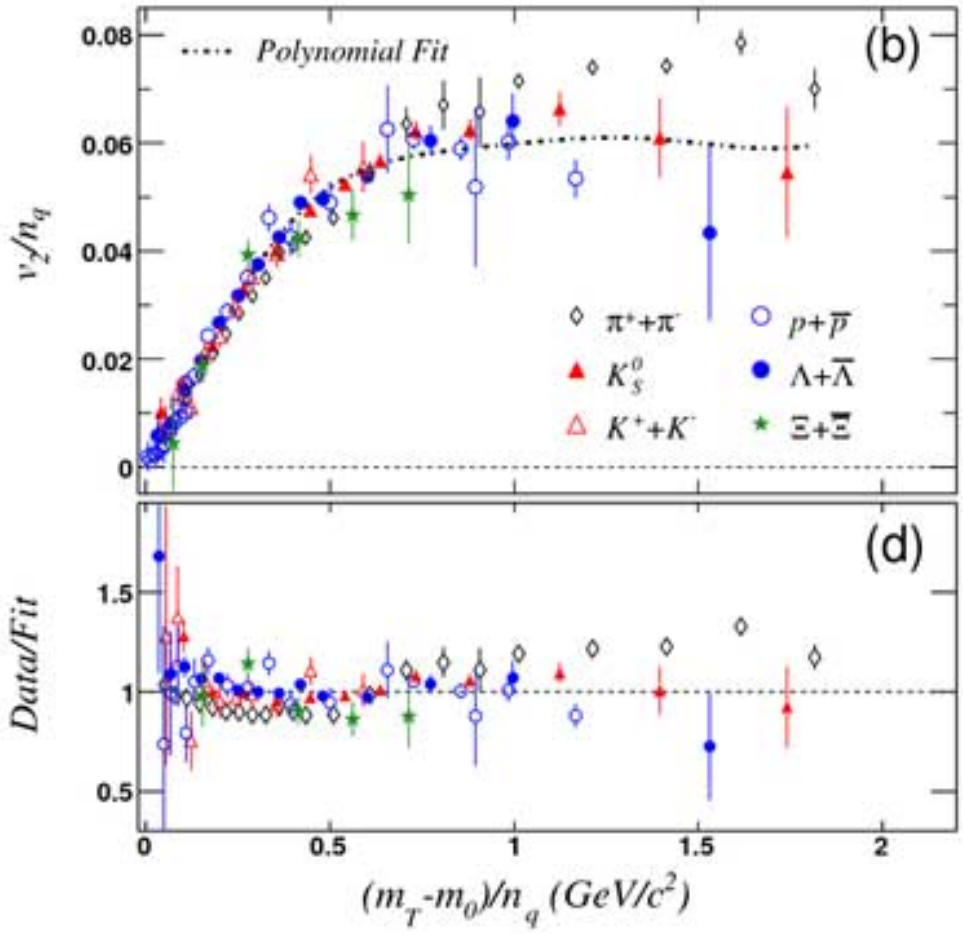

Figure 1.12: Elliptic flow as a function of transverse mass obtained from Au+Au collisions at $\sqrt{s_{NN}} = 62.4$ GeV after scaling by the number of constituent quarks (higher panel). The dotted line is based on a polynomial fit of the scaled elliptic flow data, and the lower panel shows the ration data/fit. [11]

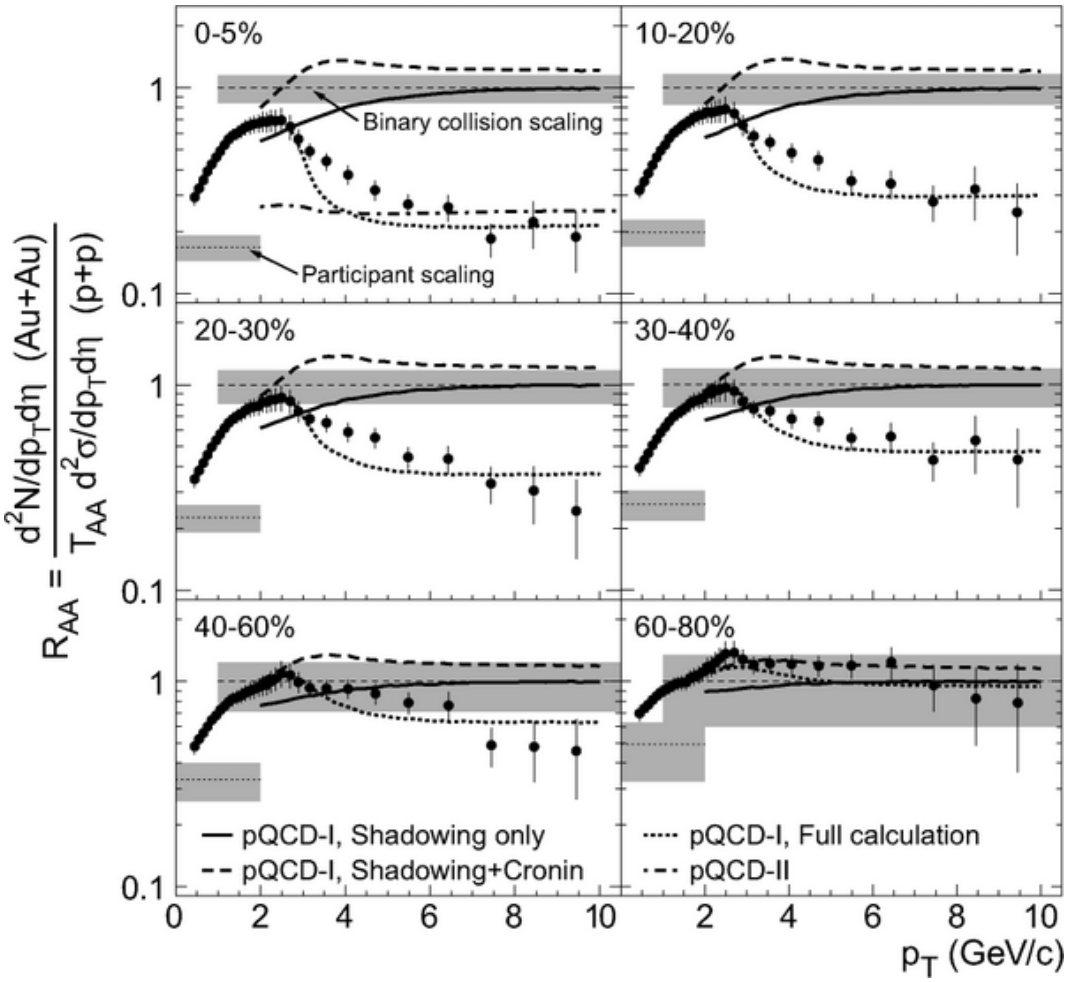

Figure 1.13: R_{AA} from Au+Au collisions at $\sqrt{s_{NN}} = 200$ GeV measured by the STAR experiment, for various centralities. We observe a strong supression of high-momentum particles in central collisions, decreasing at more peripheral centralities. [12]

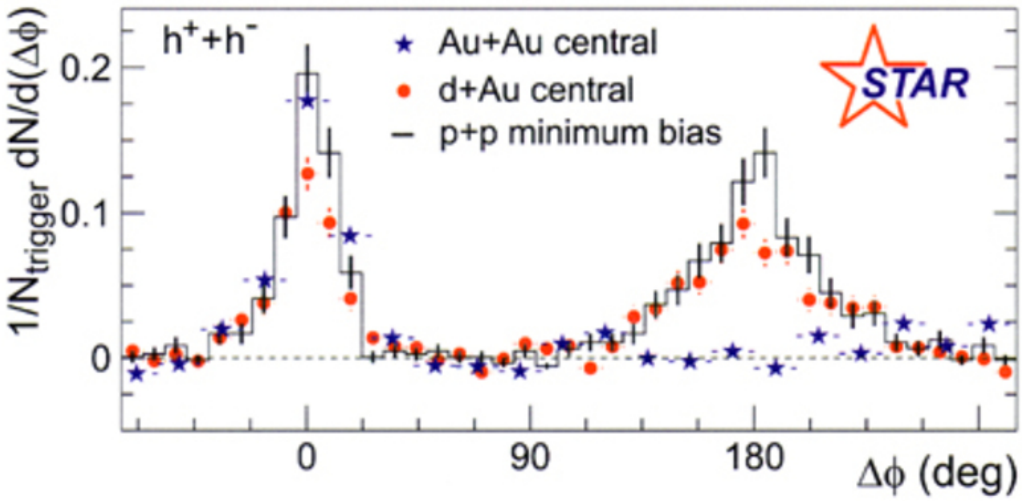

Figure 1.14: Two-particle correlations in $p + p$ and d+Au collisions (a) and $p + p$ and Au+Au collisions (b) at RHIC measured by the STAR experimental. Pedestal have been subtracted in all graphs. The peak found in $p + p$ and d+Au collisions, corresponding to dijets, disappears in Au+Au collisions [13]

Chapter 2

Theoretical Framework

2.1 The Chiral Magnetic Effect

Modern physics find its roots in the notion of symmetry and conserved quantities (currents, charges...). One of the main goals of particle physics is to identify the symmetries involved in interaction processes such as the one found in collisions. This notion of symmetry is the cornerstone of the standard model. As we have seen in the previous chapter, a category of potential symmetries of the action is the set of 3 discrete symmetries $\mathcal{C}$, $\mathcal{P}$, and $\mathcal{T}$, the charge conjugation, the parity reversal and time reversal transformations respectively. $\mathcal{C}$ reverses all internal quantum number (charge, spin...), in 3 dimensions $\mathcal{P}$ reverses space coordinates $\vec{x} \rightarrow -\vec{x}$, and $\mathcal{T}$reverses the time $t \rightarrow -t$. It was initially believed that all interactions were invariant under each of those transformations, but theorists Tsung Dao Lee, Chen Ning Yang and the experimentalist Chien-Shung Wu found evidence that the weak interaction violates the $\mathcal{P}$ symmetry and that parity was not conserved [58, 59]. It was later discovered that $\mathcal{CP}$and $\mathcal{T}$were also violated.

In the QCD Lagrangian

$$\mathcal{L} = -\frac{1}{4}F_{\alpha}^{\mu\nu}F_{\alpha\mu\nu} + \sum_{f}\bar{\psi}_f\left[i\gamma^{\mu}(\partial_{\mu} - igA_{\alpha\mu}t_{\alpha}) - m_f\right]\psi_f, \tag{2.1}$$

where f runs over the 3 colors, ψ is the quark field, t is the set of SU(3) group generators, A being the color field vector potential and F is the associated field strength tensor. This Lagrangian is $\mathcal{C}$, $\mathcal{P}$ and $\mathcal{T}$ invariant, and thus conserves parity. Another term can be added

to this Lagrangian:

$$\mathcal{L}_\theta = -\frac{\theta}{32\pi^2} g^2 F_\alpha^{\mu\nu} \tilde{F}_{\alpha\mu\nu}. \tag{2.2}$$

This term can be rewritten as a 4-divergence $\partial^\mu K_\mu$ and is thus seemingly irrelevant as it should not modify the equations of motion. However, there exist solutions of the euclidian equations of motions, named instantons, which have a non-trivial topological charge:

$$q(F) = \frac{g^2}{32\pi^2} \int d^4x F_\alpha^{\mu\nu} \tilde{F}_{\alpha\mu\nu}, \tag{2.3}$$

$q(F)$ taking integer values [60]. These solutions correspond to a transition (via tunneling) to a different vacuum characterized by a different topological Chern-Simons number:

$$\nu = \int_{-\infty}^{+\infty} dt \frac{dQ_5}{dt}, \tag{2.4}$$

where $Q_5 = \int d^3x K^0$ is the chiral charge. These degenerate vacua introduce a term of the form $e^{i\theta q}$ in the QCD action, adding an effective θ to the Lagrangian.

A non-zero value of θ introduces $\mathcal{P}$ and $\mathcal{CP}$-violation. However, this $\mathcal{P}$-violation has been looked for and never observed. A prediction based on a non-zero value of θ was the existence of an electric dipole moment in neutrons; measurements made on neutrons have set an upper limit to the value of θ: $\theta < 3 \cdot 10^{-10}$. However, this measurement corresponds to an average value of θ, and the conclusion is that there is no *global* $\mathcal{P}$-violation in the strong interaction. It does not exclude the possibility that parity is violated locally, via the transition to a vacuum state different from the ground state. A picture where contributions from different vacuum states to $\mathcal{P}$-violation cancel each other is still consistent with the results obtained for the neutron electric dipole moment. Figure 2.1 shows how the fluctuations in topological charge give rise to a null average dipole moment.

In particular, a $\mathcal{P}$-violating metastable vacuum could be transitioned to in the hot and dense medium created by heavy ion collisions, which would affect the way quarks interact in

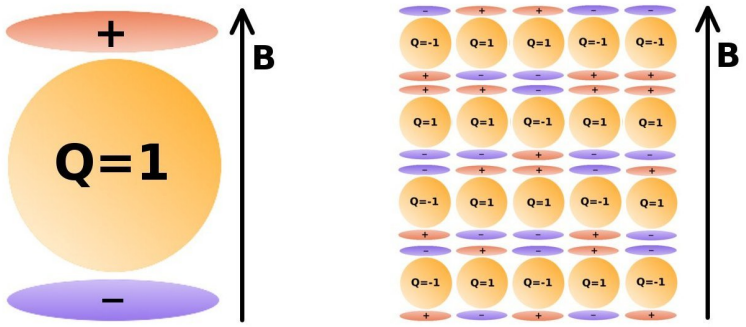

Figure 2.1: Effects of the event-by-event fluctuations of the topological charge. Because of these fluctuation, a measurement of the dipole moment would average to zero [14].

this region. One feature of such a region would be how it affects the chirality of produced quarks. The quark-antiquark pairs produced in the non-trivial vacuum would have a total non-zero chirality $\langle \vec{\sigma} \cdot \vec{p} \rangle$, depending on the topological charge. If we consider the QGP as an axially symmetric domain (with the symmetry axis being the angular momentum vector, perpendicular to the reaction plane), the spins of the quarks orient themselves along the symmetry axis, parallel to the strong magnetic fields created in the medium. The direction of alignment depends on the charge of the quark (Figure 2.3). Positively charged quarks will have spins parallel to the magnetic field, while the spins of negatively charged quarks will be anti-parallel to the magnetic field. Figure 2.2 shows the orientation of this magnetic field and the reaction plane with respect to each other. These magnetic fields, which can reach 10^{14} T, are created by the strong currents from the charged, ultrarelativistic spectators moving in opposite directions on each side of the medium. In the presence of instantons or sphalerons, the combination of the charge-dependence of spin direction and the non-zero chirality would cause the production of up and down quarks to be asymmetrical with respect to that symmetry axis as the momentum of those particles would align preferentially in the same or opposite direction with respect to the spin, depending on the topological charge. This is known as the chiral magnetic effect [61, 62].

A preferential direction along the angular moment for different light quark flavors would be identified as an asymmetry in the azimuthal distribution of some charged hadrons, such

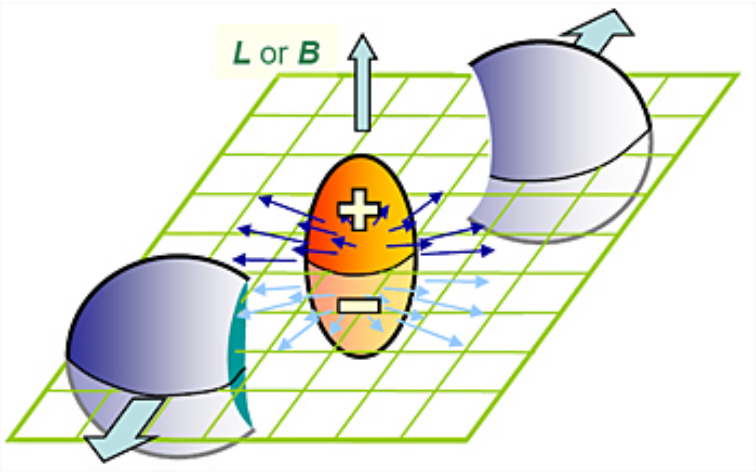

Figure 2.2: Orientiation of the magnetic field and charge separation with respect to the reaction plane [15].

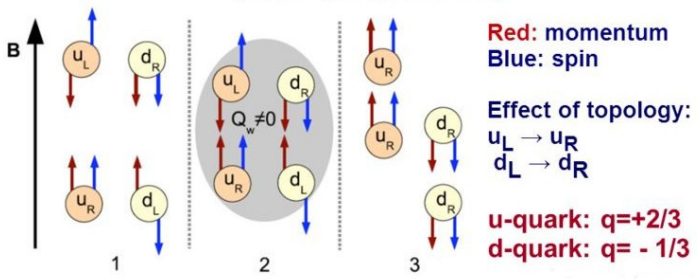

Figure 2.3: Depiction of the Chiral Magnetic Effect. The combination of parity violation, which fixes the helicity of the produced quarks, and magnetic field, which in interacts with the spin of these particles, orients momenta in the direction perpendicular to the reaction plane according to the charges, creating charge separation [16].

as pions.

The complete expression for the Fourier expansion of the particle density azimuthal distribution is

$$E\frac{d^3N}{dp_T^3} = \frac{d^2N}{2\pi p_T dp_T dy}\left(1 + \sum_{n=0}^{\infty}\left(v_n \cos\left(n\left(\phi - \psi\right)\right) + a_n \sin\left(n\left(\phi - \psi\right)\right)\right)\right), \qquad (2.5)$$

where ϕ is the azimuthal angle, ψ is the angle giving the position of the reaction plane. The a_n coefficients are usually omitted in this distribution. The definition of the reaction plane implies that the collision is symmetric with respect to that plane. As a consequence, the

sine coefficients are considered to be 0, although event-by-event statistical fluctuations give them a finite value, and only the v_n coefficients are calculated. However, the asymmetry in charged pion production manifests itself out-of-plane. Thus, in the presence of $\mathcal{P}$ violation and as a consequence of the CME, the value of some of the a_n coefficient (most notably a_1) would be finite.

The magnitude of this effect is expected to be rather small (~ 0.01) and would be impossible to detect in a single event because the large multiplicity of particles and event-by-event fluctuations would mask it. Moreover, the sign of the a_1 coefficient for a specific species of pion with respect to the angular moment of the QGP is not constant, as it depends on the topological charge of the $\mathcal{P}$ violating region. This charge can take both positive and negative signs, and the preferential directions of pion emission reverse when it changes sign. Hence the average of a_{1+} (for π^+) over a large number of events will be null; a similar reasoning applies to a_{1-}.

The study of like- and opposite-charge pions flow correlations, $\langle a_\alpha a_\beta \rangle$ where α and β can correspond to π^+ and π^-, provides a solution to these issues. On the other hand, contributions to this correlator from effects that are not due to $\mathcal{P}$ violations might be significant and need to be evaluated before any conclusion can be drawn from the corresponding results. Evaluating this correlator can be made by calculating $\langle sin(\Delta\phi_\alpha) sin(\Delta\phi_\beta) \rangle$. However, this correlator can be rewritten as $\langle a_\alpha a_\beta \rangle + B_{\text{outofplane}}$, B being a background contribution containing correlations unrelated to the reaction plane. If we instead calculate

$$\begin{aligned} \langle cos(\phi_\alpha - \phi_\beta - 2\phi_c) \rangle &= \langle cos(\Delta\phi_\alpha) cos(\Delta\phi_\beta) \rangle - \langle sin(\Delta\phi_\alpha) sin(\Delta\phi_\beta) \rangle \\ &\approx -\langle a_{1,\alpha} a_{1,\beta} \rangle + [B_{\text{inplane}} - B_{\text{outofplane}}], \end{aligned} \tag{2.6}$$

under the assumption that directed flow is very small, we have eliminated all background contributions unrelated to the reaction plane [63]. Estimates for the magnitude of the parity violation effect give an order of magnitude for the value of this correlator of $\sim 10^{-4}$. Its dependence on the centrality of the event should follow from its dependence on pion multiplicity

and the magnetic fields involved, and decreases faster than $1/N$. The rapidity dependence of the effect is such that it is expected to happen entirely within the central barrel acceptance. In practice, the calculation of this correlator can be made through the use of a third species of particles (three-particle correlation), according to the following equation:

$$\langle cos(\phi_\alpha - \phi_\beta - 2\phi_c)\rangle = v_{2,c}\,\langle \cos(\phi_\alpha + \phi_\beta - 2\Psi_{RP})\rangle\,, \tag{2.7}$$

with c denoting the third species. In order for this formula to hold, the third particle must not have non-flow correlations with the charged pions. Such correlations would introduce a systematic uncertainty which should be limited by a proper choice of the third particle species.

Equation 2.7 requires the calculation of the elliptic flow for the c-particle, but not the direct determination of the event plane from the charged pions. We can thus chose an appropriate third particle with a large flow that will only be correlated to pions through event-plane related correlations. This correlator is indeed a $\mathcal{P}$- even quantity, which means it is sensitive to flow correlations unrelated to $\mathcal{P}$-violations. Identifying the processes in which the pions will be correlated and evaluating their magnitude is thus necessary for a proper interpretation of the results. One of the biggest challenge of the flow coefficient calculation, when looking for evidence of $\mathcal{P}$ violation, will be to eliminate the contributions from non-flow correlations. These contribution can come from several sources, such as jets, clustering, or resonance decays. While most of these effects depend on multiplicity like 1/N , which implies that they will have a lesser impact on the value of the flow coefficients at LHC than at RHIC, some might account for a significant part of the value of those coefficients. The a_1 component of the flow which could arise from parity violations is expected to be, at best, quite small (~ 0.01). Conducting a thorough study of the different sources of correlations is a necessary step of the analysis before any conclusion can be drawn.

Among those processes which contribute to the background affecting the correlator

measurement is the production of particles from cluster decays. By making the assumption that the only contribution to the value of the correlator comes from those decays, we can estimate its influence on the final result:

$$\langle \cos(\phi_\alpha + \phi_\beta - 2\Psi_{RP}) \rangle = \frac{N_{\frac{clust}{event}} \cdot N_{\frac{pairs}{clust}}}{N_{\frac{pairs}{event}}} \cdot \langle cos(\phi_\alpha + \phi_\beta - 2 \cdot \phi_{clust}) \rangle_{clust}, \tag{2.8}$$

where the "clust" index indicates that we are only taking the average over pairs coming from the same clusters. This quantity can be estimated using simulations and then compared to the experimental value of the correlator.

2.2 Local Charge Conservation

One source of background expected to affect Equation 2.6 is the interplay of local charge conservation and the strong elliptic flow found in non-central collisions. The principle behind local charge conservation (LCC) is that particles created in a heavy ion collision, be they of partonic or hadronic nature, are created in opposite charge pairs [64]. The main tool used for the study of balancing charge is the balance function:

$$B\left(p_2|p_1\right) = \frac{N_{+-}\left(\mathbf{p_2}|\mathbf{p_1}\right) - N_{++}\left(\mathbf{p_2}|\mathbf{p_1}\right)}{dM/d\mathbf{p_1}} + \frac{N_{-+}\left(\mathbf{p_2}|\mathbf{p_1}\right) - N_{--}\left(\mathbf{p_2}|\mathbf{p_1}\right)}{dM/d\mathbf{p_1}}, \tag{2.9}$$

where $N_{\alpha\beta}$ is the number of pairs composed of a particle of charge α and one particle of charge β, and M is the charged particle multiplicity. It can be interpreted the following way: given a charged particle with momentum p_1, it is the probability that a particle with momentum p_2 has opposite charge rather than same charge. Experimental evidence has shown that initial spatial correlations, when combined with elliptic flow, gave rise to correlations in momentum space [65]. In general, all particles created in the same nucleon-nucleon binary collisions receive momentum space correlations from having been created in proximity of each other and are collimated by flow. However, the strong spatial correlations of the

balancing charges introduces an additional azimuthal correlation between these two particles. The various moments of anisotropic flow give a reaction-plane dependence to these correlations. For instance, elliptic flow will give rise to stronger correlations in-plane than out-of-plane, which translate in a contribution to the mixed-harmonic correlators introduced in Equation 2.6. Similarly, the effect of quadratic flow on local charge conservation will affect the charge-dependent double-harmonic correlator $\langle\cos\left(2\phi_a + 2\phi_b - 4\psi\right)\rangle$. When calculating the opposite-charge pair correlations, one has to remember that local charge conservation is not the only source of correlation that arises from the interplay of spatial proxmity and flow. In particular, local charge conservation would express itself as a background to the correlators used in the search for the CME via a difference between the opposite- and like-charge correlator:

$$2\langle\cos\left(\phi_+ + \phi_- - 2\psi\right)\rangle - \langle\cos\left(\phi_- + \phi_- - 2\psi\right)\rangle - \langle\cos\left(\phi_+ + \phi_+ - 2\psi\right)\rangle. \tag{2.10}$$

As a consequence, while LCC could potentially explain the difference between the opposite and same sign versions of the second harmonic correlator from Equation 2.6, the strong same-sign signal alone cannot be explained in this fashion and requires another mechanism. A proposed candidate is the effect of momentum conservation, as discussed in [66].

This dissertation is centered around the estimation of the LCC background affecting the charge-dependence of the second harmonic correlator using the fourth harmonic correlator. The latter is not sensitive to the CME, allowing the measurement of purely non-CME contributions. A comparison of the ratio of the fourth to second harmonic correlators with phenomenological calculations can help us determine the magnitude of the contribution of LCC to the second harmonic correlator.

Chapter 3

Experimental Setup

3.1 The Large Hadron Collider

The results presented in this dissertation are based on ultrarelativistic heavy ion collision data collected by the ALICE experiment at the Large Hadron Collider (LHC). The LHC is a colliding beam facility that first became operational in 2009. It is the result of an international effort to build a high-energy physics experimental facility that would reach center-of-mass energies greater than those of other existing colliders and provide new experimental results that would help confirm (or infirm) a series of theoretical predictions. The most widely known of such predictions is the Higgs mechanism (more accurately Englert—Brout—Higgs mechanism) which provides an explanation for the electroweak symmetry breaking, and was confirmed in 2012 with the experimental discovery of the Higgs boson. The LHC might provide the first experimental steps leading beyond the standard model, although no such results have been obtained as of yet. The LHC facilities are located at the European Center of Nuclear Research near Geneva (better know as CERN based on the French initials). The LHC ring is 27km in circumference, crosses the French-Swiss border multiple times, and uses the same tunnel that was previously used by a lepton collider named the LEP. The main component of the LHC is a synchrotron capable of accelerating two beams of either protons or lead ions at velocities very close to c, and energies of several TeV. Currently, beam energy has reached values as high as 4 TeV for protons and 2.76 TeV for lead ions, but a run of pp collisions at $\sqrt{s_{NN}}$= 14 TeV is planned for 2015. The LHC operates as follow: protons are obtained by stripping away electrons from a hydrogen gas using an electric field;

a similar procedure is applied to obtain lead ions for the relevant experiments. They are then injected in a linear accelerator (LINAC 2) which brings them to an energy of 50 MeV. Following this, they are transfered through a series of 3 synchrotrons which each accelerates the beam to higher energies: first the PSB (Proton Synchrotron Booster) brings it to 1.4 GeV, then the PS (Proton Synchrotron) brings it to 25 GeV, and finally the SPS (Super Proton Synchrotron) brings the beam to 450 GeV before injecting it into the main LHC ring where they will reach the energy required for the experiment. Figure 3.1 shows the locations of the various components and facilites of the LHC.

Figure 3.1: Location of the large hadron collider accros the Swiss-French border [17].

3.2 The ALICE Experiment

ALICE is general-purpose detector optimized for the study and analysis of ultra-relativistic heavy-ion collisions. It is designed to enable particle identification of a large number of particle species (charged and neutral pions, kaons, protons, electrons, muons, photons...) anticipated to be produced in these collisions. While the main purpose of this detector is to study Pb+Pb collisions ($\sqrt{s_{NN}}$= 5.5 TeV per nucleon pair energy), collisions at lower energies and involving lighter ions will also be analyzed to study the dependence of the QGP properties on energy density and nucleus size. p+p collisions will also be studied both as a reference for Pb+Pb collisions and for the physics specific to those collisions.

The ALICE detector distinguishes itself from the other detectors installed at the LHC

by its ability to track and identify particles over a large momentum range (from $p_T \sim 100$ MeV to ~ 100 GeV) in a high-multiplicity environment, and to allow for the reconstruction of short-lived particles such as heavy mesons. The multiplicity density (number of particle produced in the collision per unit pseudorapidity) is expected to be as high as $dN/d\eta = 4000$, but the detector has been tested in simulations with twice as much density [23]. The high-precision, slower detectors used in ALICE limit the heavy ion collisions to a reduced rate relative to the other LHC experiments ($\sim$ 10 kHz for Pb+Pb). A set of triggers makes it possible to select specific rare events, such as those containing high-momentum jets. Up to $\sim$ 10 million events can be selected and stored this way each year of operation (effectively during a few weeks allocated to Pb+Pb runs).

The central part of the detector covers a pseudorapidity range of $-0.9 < \eta < 0.9$. It is composed of several detectors which are, from the inside out: the Inner Tracking System (ITS) detectors, the Time-Projection Chamber (TPC), a Time-of-Flight (TOF) array, a ring imaging Cherenkov High Mometum (HMPID) detector, Transition Radiation (TRD) detectors, a calorimeter called the Photon Spectrometer (PHOS) and another Electromagnetic Calorimeter (EMCal). Aside from the EMCal, PHOS and HMPID, the other detectors cover the full azimuthal range (not taking into account the acceptance effects due to the construction of the detector). The central barrel is surrounded by a solenoid magnet that produces a magnetic field of 0.5 T, whose purpose is to give a curvature to the tracks of the charged particles, allowing the measurement of the momentum.

Aside from the central barrel, ALICE also contains a set of small angle detectors: a forward muon spectrometer, associated with a dipole magnet to bend the muon tracks, a Zero-Degree Calorimeter, a Photon and Forward Multiplicity detectors (PMD, FMD), a T0 (measuring the event time) and a V0 (to trigger on minimum bias and reject ion-gas collisions background) detector, that are part of the trigger system and allow the characterization of the event. The trigger system is composed of several levels which allow the selection or rejection of the events based on desired properties. If desired conditions are satisifed, a

software, High-Level trigger reads the data from the TPC (a slow detector) and analyses it "online" to achieve a finer selection of events and reduce the amount of data of each event to be writtent to storage. Figure 3.2 shows the detectors composing the ALICE experiment.

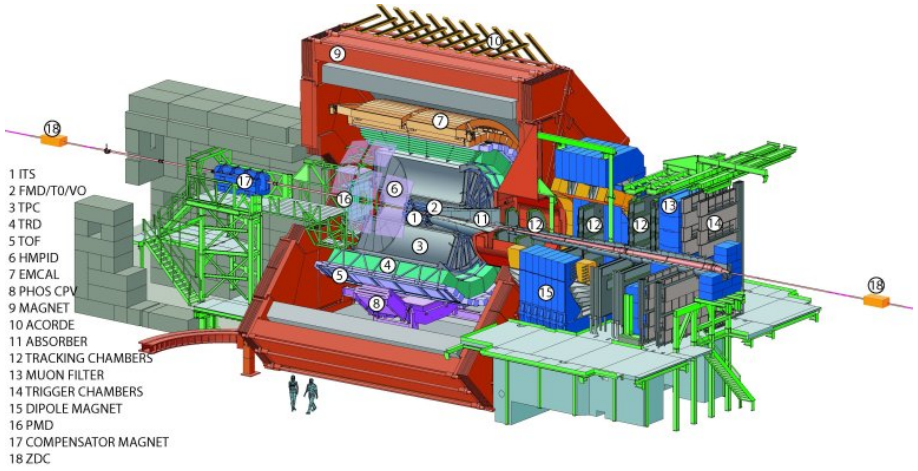

Figure 3.2: Schematics of the ALICE experiment, showing the disposition of the various detectors [18].

3.3 The Inner Tracking System

The innermost set of detectors directly surrounding the interaction vertex is called the Inner Tracking System (ITS). It is composed of six layers of silicon-based detectors, arranged in three pairs of two layers, disposed as shown on Figure 3.3. Each of these pairs is designed based on a different technology, due to the rapid change in particle density with increasing radius. Predictions on the upper limits of multiplicities in the most central collisions give values of 8000 tracks per rapidity unit. The requirement to keep the channel occupancy low prompted the design of detectors with very high granularity. The pseusdorapidity coverage varies for each detector, but the whole ITS provides $|\eta| < 0.9$ for collision vertices within the interaction diamond; all the layers cover the full azimuthal range. The main design goals of the Inner Tracking System are to locate the collision vertex with good accuracy (resolution better than 100 μm and to provide high-resolution tracking of charged particles. The ITS

adds to the tracking capability provided by the TPC, by extending the tracking of high-momentum particles (increasing the resolutions in angle and momentum), by expanding the acceptance to the dead regions of the TPC,and by allowing low-momentum (< 100 MeV) tracking thanks to the analogue readout of the four outermost layers. The high spatial resolution provided by the ITS close to the interaction vertex also enables the reconstruction of secondary vertices of short-lived resonances decay. All these detectors share similar basic principles: charged particles that traverse through the detector cause ionization, and create electron-holes pairs in number proportional to the particle energy loss. These are collected at the electrodes to form a signal that will then be treated and output by the readout electronics.

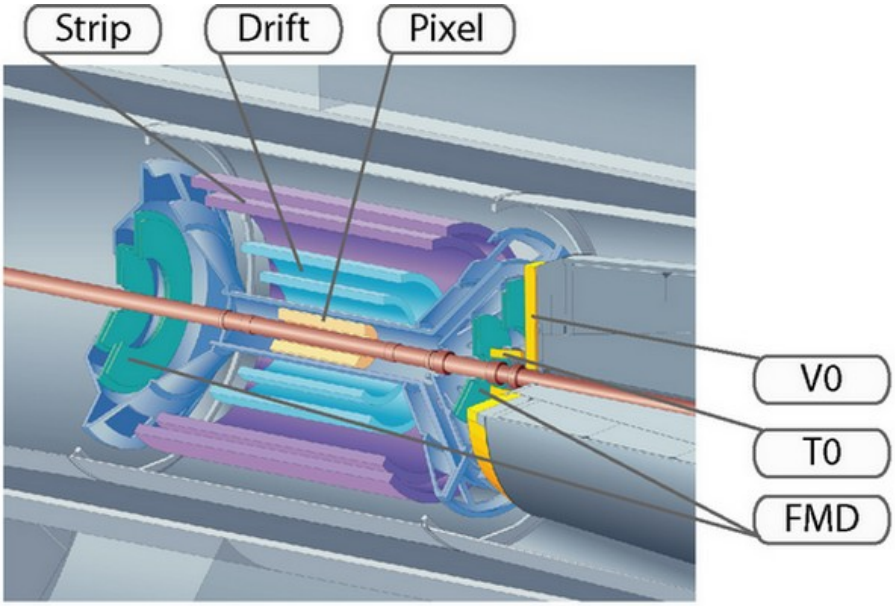

Figure 3.3: Disposition of the six layers of the ITS detectors [19].

The detector composed of the two innermost layers is named Silicon Pixel Detector. Its first layer is located at a radius or 3.9 cm from the beam axis, while the second layer is located at a radius of 7.9 cm. Each layer consists of a 2-dimensional matrix of hybrid silicon diodes (which act as pixels) in reverse bias mode, each bonded to a readout cell on a readout chip. Each readout cell contains a pre-amplifier-shaper and a discriminator. The readout is binary, the value depending on the shaped signal reaching a certain threshold. The logical

level is sent to a delay line until the arrival of the L1 trigger, and then stored in a front-end buffer. The detector is composed of 240 ladders of 256×160 cells and five readout chips (each chip serves 256×32 cells), for a total of about 9.8 million pixels. Such a high density of cells is required in the high particle densities this close to the collision vertices, which could reach 80 tracks.cm^{-2}. An added advantage of this very high granularity is the very high diode signal-to-noise ratio. In order to minimize the material budget the readout chips and sensor matrix are as thin as possible while still allowing for enough yield to obtain a proper signal; the total silicon budget of a ladder is 350 μm. In order to minimize the radiation of heat towards the next two layers of the ITS, whose operation is negatively affected by temperature change, the SPD is surrounded by a shield composed of aluminum-coated carbon fibre, which brings the total material budget to $\sim .02X_0$ for a track perpendicular to the beams. The ladders were designed to withstand in excess of 100 kGy, well above the 2.2 kGy of radiation expected over 10 years of operation. The readout chips (ALICE1LHCb) are programmable, application-specific integrated circuits (ASIC). The values of leakage current compensation, individual and global threshold voltages for the cell readout binary output, current and voltage bias references and trigger delay can be adjusted by modifying the global and individual cell registers. The outputs of readout cell discriminators provide a fast-OR signal when at least one pixel registers a hit. This functionality enables the SPD to be used as a part of a L0 trigger which can be particularly useful for low-multiplicity pp events. Like the pixels themselves, the fast-OR runs on a 10 MHz system clock. As the bunch crossing frequency is 40 MHz, the fast-OR signal is integrated over 4 bunch crossings. When the L2 trigger signal is received by the readout chips, the data located in the first location of the buffers are sent to shift registers, then sent to the PILOT chip in 256 (one for each row) 32-bit words. At each clock cycle, the data for a particular row are output, and each chip of a pair of ladders composing a half-staff is read sequentially, and all half-staves are read in parallel, giving a total readout time of 256 μs. This allows the SPD to operate on a 1 kHz L2 trigger, where only it and the muon arm are readout.

The two intermiediary layers form the Silicon Drift Detectors (SDD). They are composed of 260 wafers with a sensitve area of 70.17 mm $\times$ 75.26 mm, located at a radius of 15 cm and 23.9 cm from the beam axis respectively, where particle density could reach 7 cm^{-2} for the most central collisions. The SDDs have a material budget of $.011X_0$ for each layer, and $.029X_0$ for the supporting structure. Each element of the SDD is composed of a Neutron Transmutation Doped silicon ladder arranged in two drift regions separated by a central cathode. On each drift regions and on both sides of the wafer are found 291 other parallel, regularly spaced p^+ cathode strips with a pitch of 120 μm. A voltage bias of 2.4 kV is applied to the central cathode, and voltage dividers provide a decreasing voltage between each cathode to generate a drift field parallel to the wafer. At both extremities, a row of anodes form the collecting region. This region contains on one surface a pull-up cathode and on the other an array of 256 anodes connected to the front-end electronics, arranged in a line parallel to the cathode strips, with a pitch of 294 μm. A separate power supply ensures that independently of the central cathode bias, a -40 V voltage difference exists between the last cathode and the anodes. When a charged particle crosses the silicon, it frees electrons which are then subject to the drift field and carried to the nearest collection region and the anodes [67]. The integral of the signal collected from the interaction of one particle with the SDD is proportional to the dE/dx energy loss; unlike SSD signals, the amplitude of the signal is relevant for these detectors and will be digitized via ADC. The front-end electronics consist of three successive sets of ASICs. The so-called PASCAL ASICs sample the signal from the anodes row at $\sim$ 40 MHz, amplify and digitize it upon receiving a trigger signal. The data output by a PASCAL chip are then sent to an AMBRA chip, which perform 10-to-8 bits data compression on the signal and stores it on a 4-deep buffer. The signal finally reaches a CARLOS ASIC, which performs zero suppression and data compression. The position of a hit by a charged particle can be reconstructed using the position of the anode that produced the signal, which gives one of the coordinates (z) in a straightforward fashion, as well as the drift time, which can be used to extrapolate the other coordinate (rphi) assuming constant drift

velocity of 8.1 μm.ns^{-1} produced by a -2.4 kV central anode bias voltage. Because knowledge of the drift velocity is critical to the hit localization and track reconstruction processes and since it can vary significantly with temperature, MOS charge injectors are located in each drift region to monitor drift velocities. The 40.08 Mhz sampling rate of the anode signal by the PASCAL chips coupled with the anodes pitch gives a cell size of 294 μm $\times$202 μm, for a total number of cells of 2316×10^6. These characteristics ensure the SDDs have good spatial resolution and multitrack capabilties, with the ability to distinguish clusters from different particles with a relative separation of 800 μm around the central cathode with $\sim$ 70% efficiency. The SDDs also participates in momentum reconstruction via energy loss (dE/dx) information, offering a good compromise between track information and granularity.

The two outermost layers of the ITS are composed of Silicon Strip Detectors (SSD). The sensors composing the SSD are 73×40 mm2 active area silicon wafers covered with 768 p-strips on one side and 768 n-strips on the other. All the strips on one side are parallel, with a pitch of 95 μm. However the p- and n-strips make an angle of 35 mrad with each other, with the p-strips and n-strips making an angle of 7.5 mrad and 27.5 mrad with the beam axis respectively, creating a net which will allow the location of a hit matching p- and n- strips signals. The sensors operate along the following principles: charged particles going through the wafer will create charge carriers (electrons and holes), which are then collected by the n- and p-strips respectively. The relatively small angle between n- and p-strips (so-called stereoscopic angle) was determined by simulations to minimize ambiguity from multiple hits, as shown in Figure 3.4.

The 5$^{\text{th}}$ and 6$^{\text{th}}$ ITS layers are mounted with the n- and p-sides facing the interaction vertex, which results in a total of four different orientations for the strips, allowing greater accuracy in the localization of hits. The hit precision is $\sim$ 20 μm in the rϕ direction and 820 μm along the beam (z) axis. The front-end electronics of the SSDs are composed of 12 HAL25 ASIC per sensor. These chips pre-amplify and shape the signal into a voltage step with a magnitude dependent on the amount of charge collected by the strips. The HAL25

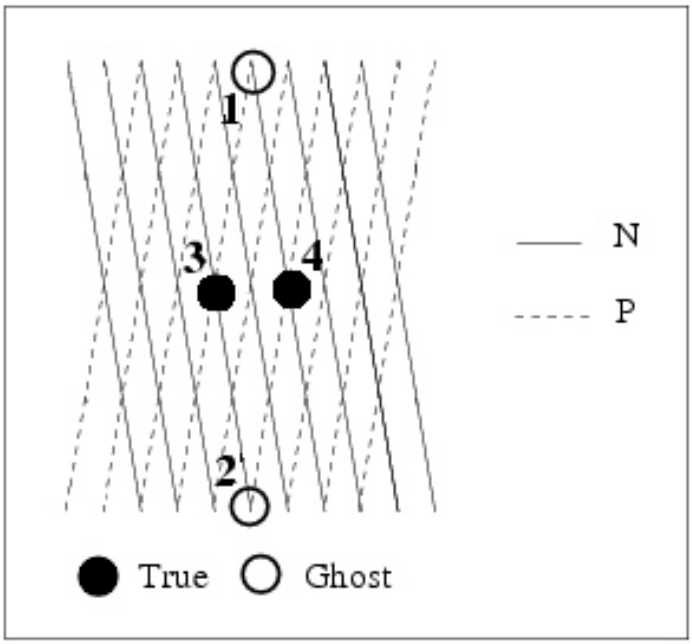

Figure 3.4: Multiple particle hits fire several pairs of strips creating ambiguities ("ghosts"). The small stereoscopical angles allows an easier discrimination between real and fictive hits using charge correlations between both sides of the sensor [20].

hold the signal upon reception of a L0 trigger-derived HOLD signal, awaiting a L1 trigger. A L1-reject ends the readout the sequence and removes the HOLD signal, while a L1-accept triggers the digitization and zero-suppression of the signals. Provided a L2-accept trigger has been received, the signal is stored in a multi-event buffer once the digitization and zero-suppression are complete, which allows a new trigger cycle to take place while the data are transferred to the DAQ system.

3.4 The Time Projection Chamber

The main detector of the central barrel (and, by extension, the tracking system) is the Time-Projection Chamber. Its purpose is to provide accurate tracking of charged particles with 2π azimuthal coverage, allowing track reconstruction over a large range of momenta and particle identification via specific energy loss (dE/dx) in the low momentum region

(less than a few GeV/c) and in the very high momentum region (a few dozen GeV/c), the so-called "relativistic rise" region. It was designed to provide a momentum resolution $< 1\%$ in the 100 MeV to 1 GeV region in a 0.5T field, and, when used in combination with the other tracking detectors, to attain a resolution of $\sim 10\%$ for very high-momentum tracks (100 GeV/c), to provide discrimination of charged tracks with similar momenta if their momentum difference is at least on the order of 5 MeV/c, and a dE/dx resolution of $< 5\%$ in the low momentum region, and $\sim 7\%$ in the relativistic rise at large multiplicities. It is able to operate in central events approaching a charged particle density of $dN_{\mathrm{ch}}/d\eta = 8000$ for a total of 20000 tracks in the TPC. In such events, the occupancy reaches $\sim 40\%$ at the innermost radius and $\sim 15\%$ at the outermost radius. In the much higher rate of interaction during pp runs, the tracks for ~ 60 events are registered together with the triggering event in the TPC, and rejected by discriminating tracks with the wrong vertices. The tradeoff for the outstanding tracking abilities and momentum resolution is the relative slowness of the detector. Its maximum rate of operation is a 400 Hz for minimum bias Pb–Pb events, 200 Hz for central Pb–Pb events and 1000 Hz for pp events. The TPC is a cylindrical field cage divided into two regions by a central electrode, covering the rapidity region between -0.9 and 0.9 (although it reaches 1.5 if we include partial tracks with reduced momentum resolution). Its inner radius is ~ 85 cm, its outer radius ~ 2.50 m, and its length in the z direction is 5 m. It is filled with a gas mixture of 90% Ne and 10% CO_2. Readout is provided by multi-wire proportional chambers with cathode pad, located in the 18 end-plate sectors. The TPC is separated in two regions along the z axis by a central electrode at z=0. This electrode is brought to a 100 kV potential (while the endcaps are kept at the reference voltage), with voltage dividers located in the inner and outer support rods of the TPC, aligned with the "dead zones" between the readout chambers. This creates a field cage with a strong uniform electric field, insulated from the rest of ALICE by CO_2 containment vessels surrounding the drift cage. Schematics of the TPC are shown on Figure 3.5.

When a charged particle travels through the gas filling the TPC, it loses energy while

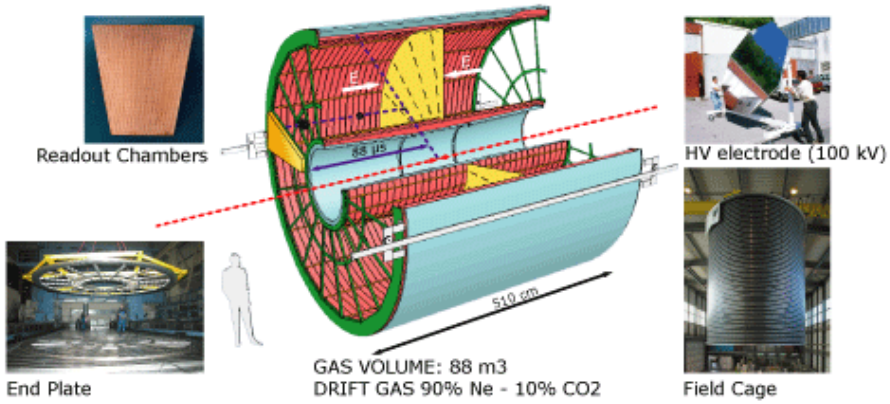

Figure 3.5: Schematics of the TPC (showing the electric field orientation) and pictures of some of its various components [21].

ionizing the gas, separating electrons and ions. The 400 V.cm^{-1} electric field drifts the electrons towards the end plates and the readout proportional chambers where they are collected to provide a signal. This provides a 3D-picture of the track: two dimensions are given by the x and y position of the hits on the readout chambers, while the z-axis location of the track is obtained from the time distribution of hits and extrapolating using the known drift velocity of 2.94 cm.μs^{-1}. The stability of drift velocity is critical to the tracking resolution, which in turn means that the temperature of the gas needs to be stable as well, as it significantly affects drift velocity. The collected charge is amplified and integrated, then processed by a shaper in a "PASA" ASIC chip, each of which contains the readout electronics for 16 channels. The signal is then sent to an ALTRO ASIC, where each channel's output is digitized by a separate 10-bit pipelined ADC, then stored in memory upon reception of an L1 trigger signal. It is then either discarded if an L2 reject is received, or the latest event data are frozen and processed furthered. Following this, the signal undergoes channel-to-channel gain equalization, tail cancellation baseline subtraction and zero-supression. Time stamps and size information are added to the data packet containing the final, corrected signals, and the output is sent to a data memory before being transmitted to DAQ. For a very large

multiplicity event, the TPC data could reach a total size of 60 MB[23].

3.5 The VZERO Detectors

The VZERO (or V0) detector provides ALICE with centrality identification and triggering for the central barrel, minimum bias triggering, luminosity measurements and a pp validation signal for the muon trigger. The triggers provided by the VZERO are of L0 level. It is composed of 2 arrays called VZEROA and VZEROC, located on both sides (A and C) of the interaction vertex (Figure 3.6). The VZEROC is placed on the muon spectrometer side, in ahead of the front absorber, 90 cm from the interaction point, while the VZEROA array is located 340 cm from the interaction point on the other side. Because of their location, special care is taken to remove secondaries due to electrons generated by the material located in front of the arrays when calculating centrality/multiplicity or for triggering purposes. Beam gas interactions are rejected by comparing the time-of-flight for both arrays.

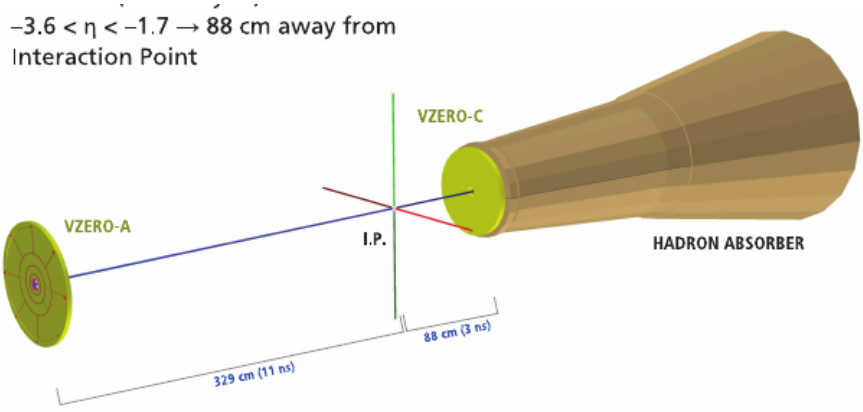

Figure 3.6: Localization of the VZEROA and VZEROC arrays on both side of the interaction point. The VZEROC is fixed to the front absorber [22].

The arrays are composed of 32 counters in 4 concentric rings, covering between 0.4 and 0.6 units of pseudorapidity. Each sector is composed of a scintillator connected via WaveLenght-Shifting fibres and clear fibres to a photomultiplier located several meters away, for a time resolution of less than 1 ns. The output from the photomultiplier is separated

into two signals, one of which is amplified tenfolds and sent to the frontend electronics. The amplified signal is processed by a Time Digital Converter (which digitizes the signal pulse time) while the unamplified one is processed by an ADC. Discrimination between beam-beam and beam-gas interactions is done using pre-adjusted time windows in coincidence with the output of the TDC, while the ADC output can be used for triggering based on the total signal output by each array, such as centrality triggering.

3.6 Brief descriptions of the other detectors

- Transition Radiation Detector (TRD)

  The Transition Radiation Detector, located around the TPC at a radius of 2.9 m, is the main detector for electron identification. It uses the photons emitted via transition radiation to distinguish between particles of different masses. It is used to discriminate electrons from hadrons (usually pions), and reconstruct light and heavy hadron from semi-leptonic or leptonic decay channels.

- Electromagnetic Calorimeter(EMCAL)

  The EMCAL, located outside of the TOF detector, identifies particles using the electromagnetic showers they trigger in scintillators. Using the cell locations and energy deposited in each cell, shower shapes can be reconstructed and analyzed. Direct photons and decay photons from neutral pions can be reconstructed. It can also be used for jet energy reconstruction and jet events triggering. It covers the $|\eta| < 0.7$ region with a 107°azimuthal coverage.

- Photon Spectrometer (PHOS)

  The PHOS detector is similar in purpose and principle to the EMCAL, but with a smaller acceptance in exchange for a higher spatial resolution. It can be used for jet triggering and reconstruction. It covers the $|\eta| < 0.14$ region with a 110°azimuthal coverage opposite to the EMCAL.

- Zero Degree Calorimeter (ZDC)

  The ZDC detector is a set of four calorimeters located 115m away from the vertex diamond on both A and C sides. Two of these calorimeters are used to detect proton spectators, and two are used to detect neutron spectators. They are mainly used to determine centrality from the number of collected spectators.

- Time-of-Flight (TOF)

  The Time-of-Flight identifies charged particles in the intermediate momentum region (a few GeV). This identification is made by combining the signal time measurement from the TOF detector with the momentum and track length from the corresponding central barrel track. It has full azimuthal coverage and a pseudorapidity coverage of $|\eta| < 0.9$. It is located around the TRD detector, at a radius of 3.7.

- T0

  The T0 detector is a set of two Cherenkov radiation detectors located on each side of the vertex diamond. It is mainly used as an early triggering (L0 level) and timing detector with a time resolution of 50 ps.

- Muon Spectrometer

  The muon spectrometer is a large forward detector aimed at reconstructing heavy quarkonia resonances via their muon decay channels (high-momentum muons). It is composed of an absorber that filters out the background made of other (non-muon) particles, a set of tracking chambers surrounded by a magnet, and a muon trigger to select heavy quarkonia events. It covers the $-4 < \eta < -2.5$ region.

- Forward Multiplicity Detector (FMD)

  The FMD is a forward detector composed of 5 rings of semiconductor detectors. It is aimed at detecting the multiplicity of charged particles emitted at forward rapidities ($1.7 < |\eta| < 5.1$). It is also used for the study of elliptic flow and multiplicity fluctuations.

3.7 Triggering Systems

The trigger system is designed to select events displaying desired features as well as accomodate the limitation of the DAQ system's bandwith when transfering the large amounts of data created by high-multiplicity central Pb-Pb events. Previous sections of this chapter have discussed a sample of the detectors found in the ALICE expriment, and in particular the varying readout and data transfer speed, data size and in general busy time. The ALICE trigger system's complexity arises from being designed around this constraint. Three levels of hardware trigger are used in ALICE, called Level 0 (L0), Level 1 (L1) and Level 2 (L2). The first two triggers are "fast" triggers. The L0 trigger is sent to the relevent detectors to instruct them to start the readout, while the L1 trigger instruct them to either continue proceeding with the readout, or discard the event. The necessity for the existence of two triggers arises from the different speed of trigger input detectors and the necessity for some readout detectors (that is, detectors on the receiving end of the trigger) to start processing the event early. The L0 trigger is sent 1.2μs after the event, while the L1 trigger is sent 6.5 μs later and is based on detectors that are two slow to participate in the L0 decision. The L2 trigger is of a different nature. It is sent after a much longer time has passed since the collision ($\sim 88\mu$s) and serves the role of past-future protection. It sends the signal that the event has been rejected or accepted based on the presence or absence of pile-up, i. e. multiple collisions registered as a single event by the readout detectors. The main component of the trigger system is the Central Trigger Processor (CTP). It receives input from triggering detectors, computes the triggering decision and dispatches it to the various detectors. The CTP is capable of handling 50 trigger classes, which are configurations of trigger input conditions, i. e. which detectors are required and the logic operation between those signals; the triggering decision can be made differently and independently to six "groups", or clusters, of detectors. Because there are so many classes, and up to 24 L0 inputs, 20 L1 inputs and 6 L2 inputs, it is not possible to simply refer to a table for the trigger decision of an event, and the CTP's

decision is based on logical AND gates.

3.8 The ALICE Online Systems

The ALICE experiment contains five online systems, Data Acquisition (DAQ), High-Level Trigger (HLT), Detector Control System (DCS), Experiment Control System (ECS) and the CTP. Figure 3.7 shows a representation of the DAQ and trigger systems and Figure 3.8 depicts the organisation of the ALICE online systems. The purpose of the DAQ system is to collect the data readout from the detectors, process it and archive it. It is designed to provide the bandwith required for the large data size of frequent Pb-Pb trigger (Pb-Pb minbias, central or mid-central events), as well as collecting the highest possible event count for rare triggers, such as dimuons or dielectrons. It performs a selection of events with high-level trigger algorithms, compresses the selected events which are then collected by the publish agent, which sends them to the Grid storage where they are referenced on the AliEn catalog; they are also eventually archived on tape by the CASTOR system.

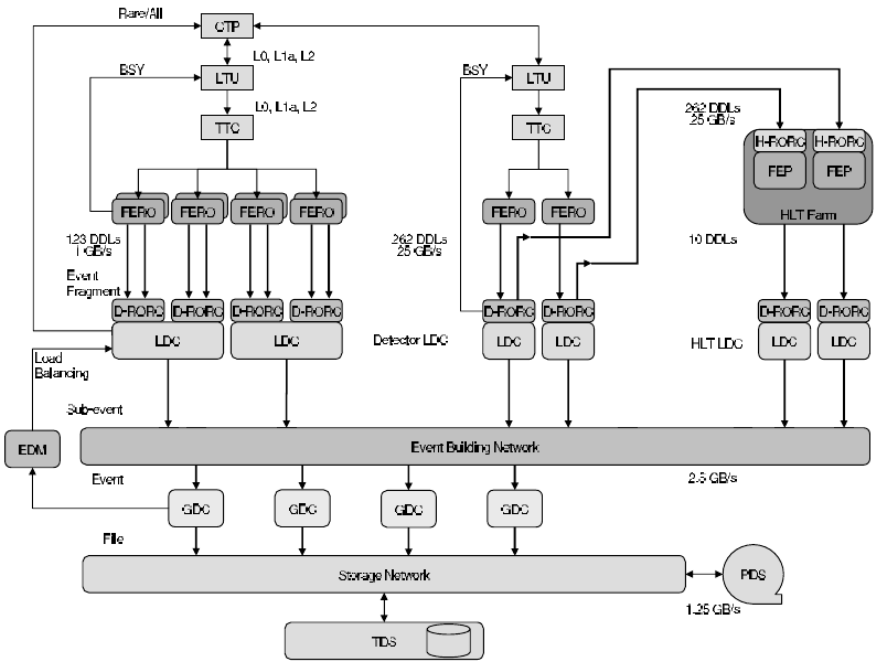

Figure 3.7: Schematics of the DAQ and trigger systems [23].

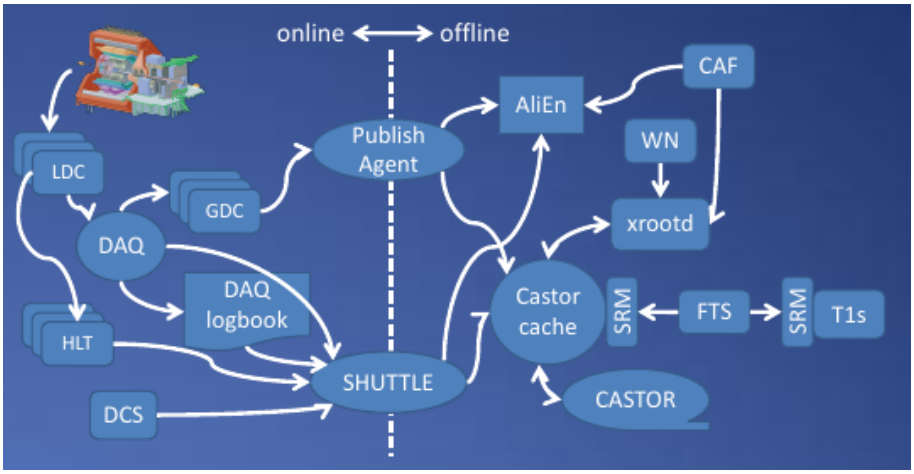

Figure 3.8: Schematics of the ALICE online systems and the online-offline transition [24].

The data transfer between the detector readout systems and the DAQ is carried out by Detector Data Links (DDL) using the same standard protocol. The front-end electronics (Local Datal Concentrators, LDCs) assemble this data into sub-events and ship them to a farm of machines called Global Data Collectors (GDCs), which collect the sub-events into a whole event before eventually sending them to the storage network. The DAQ is also able to send BUSY signals to the CTP, as well as enable (or disable) some triggers to maximize detector availability of rare events. The High-Level Trigger system receives the data in parrallel to the DAQ, through a set of DDLs. The High-Level Trigger is a system designed to sift through events that contain the signature of a rare probe or phenomenon (obtained from rare event triggers) and perform a stricter selection, rejecting fakes; it does so by performing an online analysis of these events. It can also select parts of an event while rejecting the rest (for instance filtering low-momentum tracks or cleaning pp pile-up) and compresses the data without loss of physics information. The motivation behind the use of the HLT is the limitations of the ALICE data storage, which cannot host the entirety of the data collected by the DAQ.

In addition, each detector produces condition data, which includes information relevant to its status (for instance, noisy or bad channels) and the environmental conditions (temperature, high-voltage levels) during its operation. Condition data are extracted online

by the online systems using dedicated algorithms for each detector. The requirement for the condition data to be gathered on the online side, rather than reconstructed via offline analysis, arises from the limits of the computing resources available. At the end of each run, the ECS triggers the Shuttle framework which collects the condition data from the DAQ, HLT and DCS, processes it and converts it to ROOT format, then posts it to the Offline Conditions DataBase (OCDB) located on the computing Grid storage and referenced by the AliEn catalog.

3.9 Software Aspects of the ALICE experiment

3.9.1 Vertex and Track Reconstruction

The required first step of the track reconstruction process is the determination of the event vertex, which correspond to an estimation of the collision spatial coordinates. The vertex reconstruction is conducted via the two innermost layers of the ITS which constitue the SPD. This reconstruction is conducting in two steps. The first of these steps involves a rough determination of the vertex on the z axis via the determination of the centroid (z_{cen} of hit distribution on the SPD. For vertices close to z=0, z_{cen} deviates very little from the true vertex z_{true}. However, for values z_{true} far from the center, this approximation becomes increasingly unreliable partly due to the SPD's acceptance and asymmetrical hit losses. Because of this, a polynomial relationship is used to estimate the first-order approximation of the vertex z coordinate, z_v^0. The second step involves taking the z coordinates of all the hits on the first layer (z_1) and all the hits of the second layer (z_2) and correlating each pairs of hit to obtain, in each case, a vertex position z_v (Figure 3.9). Only pairs that give a vertex position within the condidence interval of z_v^0 and within $\Delta\Phi = \phi_1 - \phi_2$ azimuthal angle cuts are considered. A distribution in z_v is obtained, which is then fitted with a gaussian function plus a constant $f(z_v) = A \cdot e^{-(z_v - z_{\text{found}})^2/\sigma^2} + C$ as shown on Figure 3.10. The value of z_{found} is taken as the z coordinate of the collision vertex. Similar processes are applied to find the

coordinates of the vertex in the transverse plane.

There are two classes of methods for the track reconstruction processes, local and global. Global track finding methods are mainly used in the HLT system and use the measurements pertaining to one track from all the detectors, simultaneously. In ALICE, global track finding is performed using a Kalman-filtering approach. Before the reconstruction proceeds, 2-dimensional clusters are found in the TPC and their center-of-gravity identified (after corrections for threshold effects) to determine the cluster's position. Similarly, ITS clusters are reconstructed and their position determined. The reconstruction proper starts with track candidates on the outer boundary of the TPC, where the track density is the lowest. The track reconstruction progresses towards the center of the TPC, assigning clusters to track candidates using the Kalman filter; each cluster added to a track improves the estimation of track parameters. The tracking is prolongated in the ITS and as close as possible to the collision vertex. Another ITS-only track reconstruction is then conducted in order to reconstruct tracks that cannot be found in the TPC (because of decays, dead zones, or momentum cuts). The tracking procedure is then restarted from the inner ITS layer to the outer TPC boundary, then tracks are extrapolated into the TOF, TRD, HMPID and PHOS detector to acquired PID information. Finally, a final Kalman-filter fit is performed from the outer radius towards the inner radius, and the information collected is used to determine secondary vertices.

3.9.2 Centrality Determination

We have seen in previous chapters the strong influence the initial geometry of the collision could have on observables. Unlike protons, nuclei are finite objects with a non-negligeable volume and this strongly influences the characteristics of collisions. The dependence of observables such as the anisotropic flow or jet quenching on the geometry and size of the system is very strong, and as a consequence there is a need for a reliable and consistent way to determine an impact-parameter related quantity that would provide information on

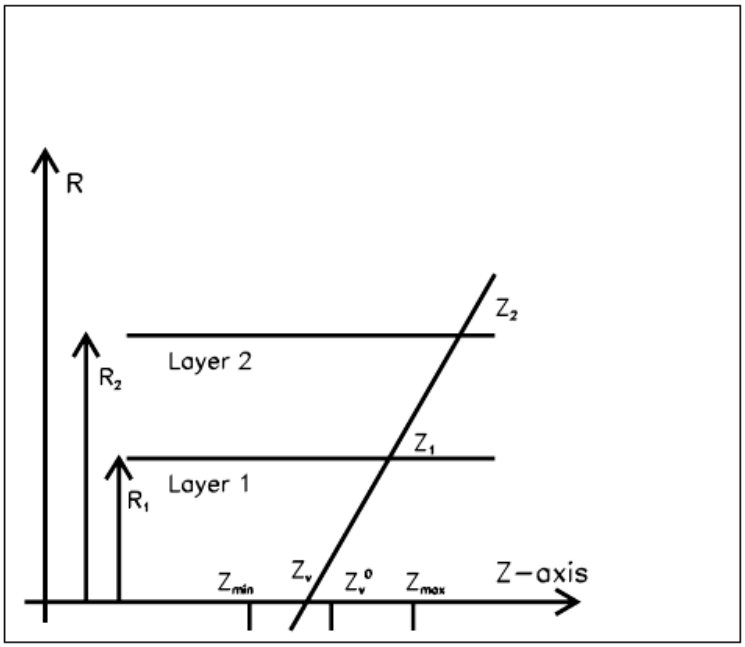

Figure 3.9: Graphical representation of the determination of the z vertex from one pair of ITS hit [23].

how close to "head-on" the collision has been and how many participants were involved in the collision.

The quantity used to estimate the overlap between the two nuclei in the collision is called centrality. It is defined as the percentage of the total nuclear interaction cross section that corresponds to an impact parameters below a certain value b_0:

$$c\left(b_0\right) = \frac{\int_0^{b_0} db \frac{d\sigma}{db}}{\int_0^{\infty} db \frac{d\sigma}{db}} = \frac{\int_0^{b_0} db \frac{d\sigma}{db}}{\sigma_{\text{tot}}}. \tag{3.1}$$

However, neither the impact parameter nor many of the quantities that would allow one to estimate it are directly measurable, such as the number of binary collisions N_{coll}, or the number of participants and spectators N_{part} and N_{spec}. However, multiplicity or total energy deposited in a calorimeter are monotonic functions of centrality (modulo fluctuations), as a lower impact parameter translates into more binary collisions and a larger number of created particles, with larger total center-of-mass energy. The definition of centrality becomes the hadronic cross section for a multiplicity above a certain value M_0 or a deposited energy above

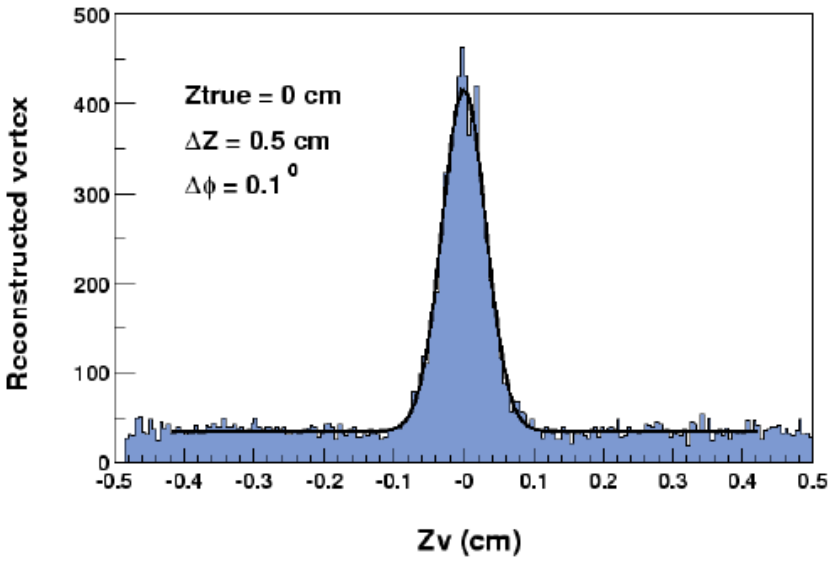

Figure 3.10: Fits of the z_v distribution obtained via ITS hit pair correlations. The centroid of this distribution is taken as the final value of the z coordinate of the vertex [23].

a value E_0:

$$c_{\text{meas}}(M_0) = \frac{\int_0^{N_0} dN \frac{d\sigma}{dN}}{\sigma_{\text{tot}}} \tag{3.2}$$

$$c_{\text{meas}}(E_0) = \frac{\int_0^{E_0} dE \frac{d\sigma}{dE}}{\sigma_{\text{tot}}}. \tag{3.3}$$

These quantities are estimated by finding the proportion of measured events with multiplicities (typically in VZERO detectors) or deposited energy (typically in the ZDC) and correcting for trigger efficiency and rejection of the most peripheral events, where the hadronic cross sections are contaminated by QED processes. This correction is done by fitting the obtained distributions with a function based on a Monte-Carlo Glauber-model of nuclear collisions. This fit also allows for the extraction of the centrality-related parameters mentioned above. However, the event-by-event detector-dependence of the centrality estimation remains and the resulting systematic uncertainties will have to be taken into account in analyses that study the centrality dependence of an observable.

In the analysis presented in this dissertation, centrality for the main measurements will be based on the multiplicity obtained in the VZERO detector, which is the standard

multiplicity used in ALICE heavy ion runs. Measurements performed using other detectors will be made for systematic error estimations. Figure 3.11 shows the VZERO multiplicity distribution and the resulting centrality definition after the Glauber model fit.

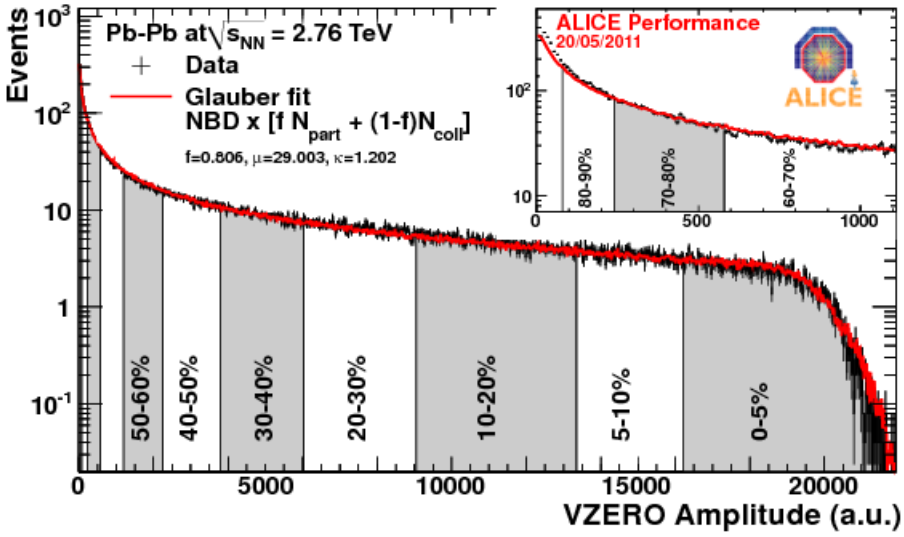

Figure 3.11: VZERO estimated multiplicity distribution and fit based on a Glauber model. The various common centrality bins used in analyses are shown [25].

3.9.3 The Analysis Framework

The analysis presented in this thesis and many others performed by the ALICE collaboration are centered around two software systems named ROOT and AliRoot. ROOT is an object-oriented software toolkit including a set of statistical analysis libraries, a C interpreter and a GUI. ROOT is widely used in the field of high-energy physics, in many experiments. It is written in C++ with an interface to FORTRAN. ROOT stores analysis data structures in objects equiped with methods appropriate for the convenient treatment of these data structures and extraction of usual parameters. Objects corresponding to many common statistical analysis data stuctures exist, such as histograms of arbitrary dimension, profiles, n-tuples, and tree-like structures. It includes mathematical libraries for integration, fourier transform, minimization and fitting, and many other complex operations. ROOT is also equiped with a power graphing tool for the display of its data structres which has been

used for many of the figures presented in this thesis.

The ALICE experiment uses a set of software libraries built on top of the ROOT system, called AliRoot. It is a set of software classes, usually written in C++, written specifically to analyze data collected by the various detectors of the ALICE experiment and related tasks including reconstruction, use of the calibration data stored on the OCDB, simulation of the detectors, quality analysis and visualization of events. The library structure of ALIROOT is shown in Figure 3.13. Its core analysis functionalities are based on the processing of events stored in 3 types of data structures, called MC (for events created by Monte Carlo simulations), Event Summary Data (ESD) and Analysis Object Data (AOD). The ESD format is the result of the event reconstruction process (i.e. tracking, etc.) and contains all the data produced by that process. It includes a header containing general event and run information such as run number, magnetic field configuration, trigger information, reconstruction software version, various collision vertex and centrality estimations, multiplicity, etc. It also contain the complete arrays of tracks, V^0 vertices and clusters found in all all the detectors. Details on AliRoot and the various event data structure can be found in [68]. A diagram depicting the organisation of the ALICE offline framework is shown on Figure 3.12.

The AOD format is obtained by filtering ESD events and selecting specific tracks, vertices and clusters. The filters obey specifications decided by the workgroups working on ALICE data based on specific analysis requirements. One particular set of filters is applied to the tracks obtained from the central barrel. These tracks are selected or rejected based on parameters and what detector data is available for this track, and then assigned a binary mask composed of filter bits. Each track can have potentially two sets of parameters (and be stored in potentially 2 track objects in an AOD): global parameters and parameters extracted from TPC clusters only. In this analysis, we will mainly use the filter "128" (so-called "TPC-only"), which corresponds to tracks containing TPC-only information without ITS cluster presence requirements, in order to preserve uniform track quality but with azimuthal "dead zones" due to the geometry of the TPC. For systematic uncertainties estimation purposes,

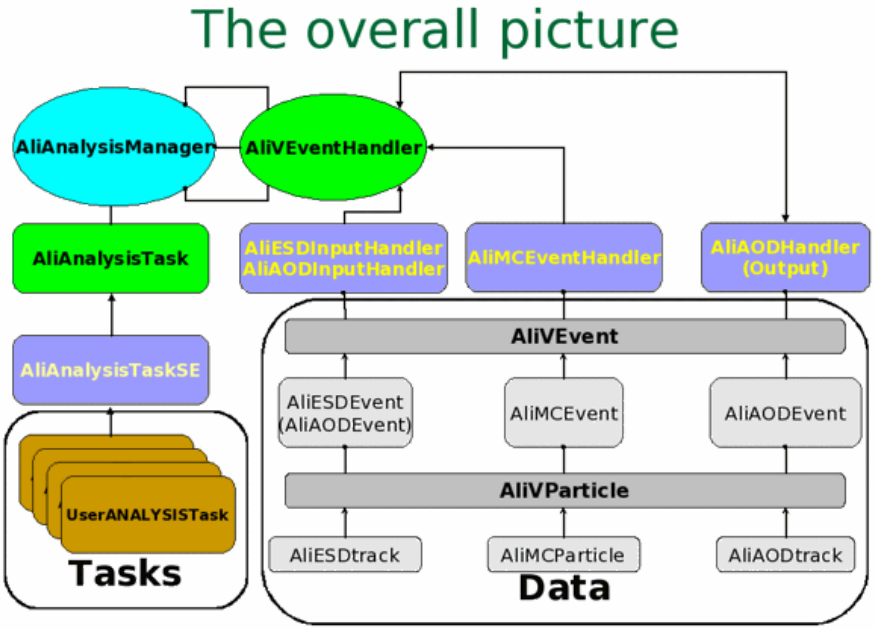

Figure 3.12: Schematics of the ALICE offline analysis framework [26].

we will also look at the 768 filter bit in 2011 Pb-Pb data (so-called "hybrid") which uses global parameters, with more uniform ϕ coverage.

In order to facilitate analysis tasks, which often have to process millions of Pb-Pb events with hundreds or thousands of tracks or clusters, often with a quadratic (or worse) time cost, CERN provides for the LHC users a distributed computing network called the Grid. It is based on a collaboration of computing centers found in many places around the world (their locations can be found on the Grid status page found in [69]. Each computing center provides data storage, which, when taken globally, can host the 15 yearly petabytes of data produced by the LHC. These centers also provide computing power for analysis tasks. The ALICE Environment software (AliEn) provides an interface to the Grid for ALICE users, including various routines and shell environments to browse the catalog of files stored on the Grid and manage them, as well as submit analysis "jobs" to the dispatcher, which will separate them into smaller subjobs that each process a limited amount of data. The job submission is done through the creation and execution of a script written in the Job Description Language,

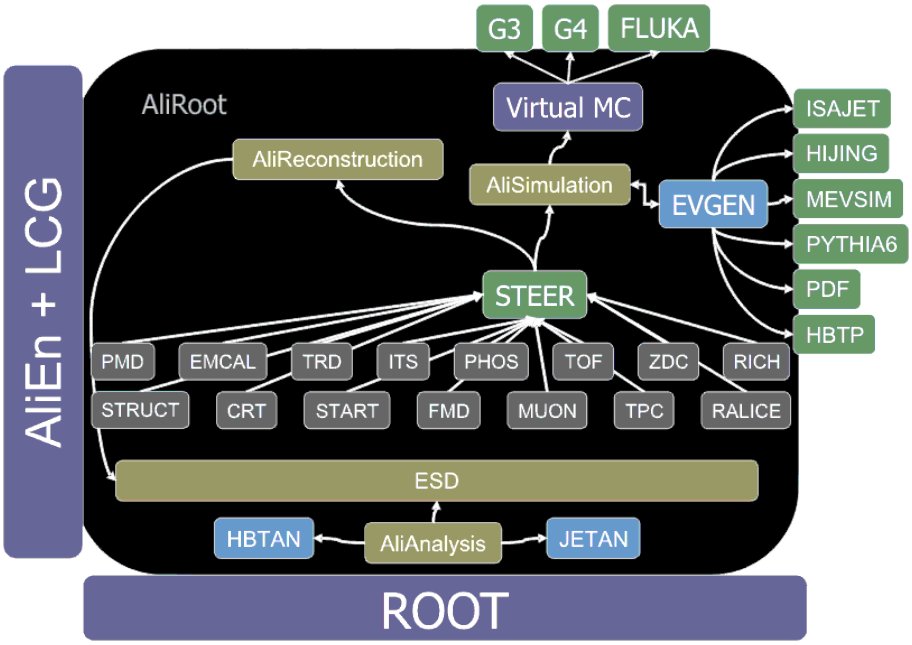

Figure 3.13: Library structure of AliRoot [27].

which tells the Grid infrastructure which versions of ROOT and AliRoot are needed as well as suplemental source files, where to store the output and which data to analyse via a catalog file written in XML.

Chapter 4

Flow Coefficients and Mixed Harmonics Calculation Methods

Over the years, a variety of methods have been devised to calculate flow and flow-like observables. While we will mainly discuss the event plane and Q-cumulant methods, others exist with different advantages and drawbacks, such as the Lee-Yang Zeros or Bessel Transform methods which remove nonflow correlations such as jet correlations.

4.1 The Event Plane Method

The first method we will discuss is also one of the earliest one to have been used to study collective phenomenon in heavy-ion collisions, the event plane method. Its principle lies in the determination of an estimate of the reaction plane for a particular subevent, composed of particles that we will call reference particles, followed by the calculation of the correlation of the particles whose azimuthal distribution we are studying, *flow particles*, with respect to that event plane.

We define the two-dimensional flow vector (also known as Q-Vector) as

$$X_n = Q_n^x = \sum_i w_i \cos(n\phi) \tag{4.1}$$

and

$$Y_n = Q_n^y = \sum_i w_i \sin(n\phi), \tag{4.2}$$

where the index i runs over all the reference particles. The weights w_i are chosen in such a way as to optimize the determination of the event plane by lowering its resolution. In general, the selection of a particular set of particles can be used as a weight, as will be the case in this analysis. From this flow fector, we define the nth order event plane as:

$$\psi_n = \frac{1}{n}\tan^{-1}\left(\frac{X_n}{Y_n}\right) = \frac{1}{n}\left(\frac{\sum_i \sin(n\phi)}{\sum_i \cos(n\phi)}\right). \tag{4.3}$$

Several remarks can be made concerning this definition. Firstly, while there is a unique reaction plane in a heavy ion collision, we can define a large number of event planes, based on the chosen order and set of reference particles. Secondly, the event plane method involves the use of anisotropic flow itself to calculate an estimation of the reaction plane.

In this analysis, the event plane is determined using data collected by the VZERO detectors. However, we have seen that this detector does not give data pertaining to individual particles, but rather a signal proportional to the number of particles going through separates sectors of the azimuthal space at the rapidities covered by the VZERO acceptance. This implies that the above definition of the flow vector will not be used when calculating an event plane with the VZERO detectors. Instead, when calculating a VZERO-based event plane, we will use the following equations:

$$X_n = Q_{nx} = \sum_i g_i \cos(n\phi_i) \tag{4.4}$$

and

$$Y_n = Q_{ny} = \sum_i g_i \sin(n\phi_i), \tag{4.5}$$

where i is an index that runs over all 32 of sectors of one of the VZERO detectors, and g_i is the corresponding gain. We have seen that the VZERO detectors have a $\pi/4$ rotational

symmetry. When we will calculate the 4th order event plane, these equations will become:

$$X_4 = Q_{4x} = \sum_i g_i \cos\left(4\phi_i\right) = \sum_i g_i \cos\left(4 \cdot \left(k + 1/2\right)\pi/4\right) = 0 \tag{4.6}$$

$$Y_4 = Q_{4y} = \sum_i g_i \sin\left(4\phi_i\right) = \sum_i g_i \sin\left(4 \cdot \left(k + 1/2\right)\pi/4\right) = \pm 1, \tag{4.7}$$

and

$$\psi_{4,\ \mathrm{VZERO}} = \lim_{x \to 0^+} \frac{1}{4} \tan^{-1}\left(\frac{\pm 1}{x}\right) = \pm\frac{\pi}{8}. \tag{4.8}$$

The fourth order event plane calculated from the VZERO detectors (both A and C sides) can only take 2 discrete values; this will have consequences on the fourth order event plane resolution and the uncertainty of our 4th-harmonic measurements using VZERO detectors.

Once the event plane has been obtained, the calculation of the flow harmonics coefficients can be performed. Using an m$^{\mathrm{th}}$order event plane, any n$^{\mathrm{th}}$order flow coefficient v_n such that $n = k \cdot m, k \in \mathbb{N}$ can be calculated as The flow coefficients are obtained from the following equation:

$$v_n^{\mathrm{obs}} = \langle \cos\left(n\left(\phi - \psi_m\right)\right)\rangle. \tag{4.9}$$

In this equation, v_n^{obs} differs from v_n in that it is calculated using an estimate of the reaction plane rather than the reaction plane itself. However, correction methods exist to obtain the latter quantity from v_n^{obs}. In this analysis, flow and reference particles used for the calculation of event planes will always be distinct. When this is not the case, a correction to the event plane must be made to remove auto-correlation effects due to a particle being used both for flow coefficient and event plane calculation. When calculating the average from Equation (4.9) via a sum over all flow particles $\sum_i cos\left(n\left(\phi - \psi_m\right)\right)$, one has to recalculate the event plane, omitting the i particle.

Writing the azimuthal distribution with respect to the event plane as a Fourier distribution gives

$$\frac{dn}{d\left(\phi - \psi_m\right)} = \frac{1}{2\pi} \sum_k 1 + 2v_{k \cdot m}^{obs} \cos\left(k \cdot m \cdot \left(\phi - \psi_m\right)\right). \tag{4.10}$$

4.2 Event Plane Resolution

Obtaining v_n from this step is done via the calculation of an event plane resolution. We can rewrite Equation (4.9) as :

$$v_n^{obs} = \langle \cos\left(k\left(\phi - \psi_m + \psi - \psi\right)\right)\rangle = \langle \cos\left(k\left(\phi - \psi\right)\right)\rangle \langle \cos\left(k\left(\psi_m - \psi\right)\right)\rangle, \tag{4.11}$$

where we assumed that the sine terms cancel out. We identify, in Equation (4.11), the flow coefficient v_n:

$$v_n = \frac{v_n^{obs}}{\langle \cos\left(m\left(\psi_m - \psi\right)\right)\rangle}, \tag{4.12}$$

where $\langle \cos\left(m\left(\psi_m - \psi\right)\right)\rangle$ is called the event plane resolution for ψ_m. This equation involves the reaction plane angle, which we cannot know exactly. However, we can estimate this quantity from event planes (which can be of different order) calculated with a set of different, independent subevents:

$$\langle \cos\left(m\left(\psi_m^a - \psi_k^b\right)\right)\rangle = \langle \cos\left(m\left(\psi_m^b - \psi\right)\right)\rangle \langle \cos\left(m\left(\psi_k^a - \psi\right)\right)\rangle. \tag{4.13}$$

In Equation (4.13) a and b are indices denoting different subevents used to calculate the respective event planes. For "equal" subevents, of equal average multiplicity and expected event plane resolution, e.g. tracks from the A and C sides of the TPC η rang, this would reduce to

$$R_{a,m} = \langle \cos\left(m\left(\psi_m^a - \psi\right)\right)\rangle = \sqrt{\langle \cos\left(m\left(\psi_m^b - \psi_m^a\right)\right)\rangle}, \tag{4.14}$$

where $R_{a,m}$ is the m$^{\text{th}}$order event plane resolution for event planes calculated from particles belonging to the a set. However, in the case of VZERO event planes, because the A and C side detectors are not symmetrical in their pseudorapidity coverage, we do not expect the event plane resolutions to be equal, and cannot use this equation. If we were to use a third subevent, e.g. calculated using TPC tracks, we could combine the associated instances of

equation (4.13) into a single one:

$$\frac{\langle\cos\left(m\left(\psi_m^a-\psi_m^b\right)\right)\rangle\langle\cos\left(m\left(\psi_m^a-\psi_m^c\right)\right)\rangle}{\langle\cos\left(m\left(\psi_m^b-\psi_m^c\right)\right)\rangle}=\left(\langle\cos\left(m\left(\psi_m^b-\psi\right)\right)\rangle\right)^2, \tag{4.15}$$

or

$$\langle\cos\left(m\left(\psi_m^b-\psi\right)\right)\rangle=\sqrt{\frac{\langle\cos\left(m\left(\psi_m^a-\psi_m^b\right)\right)\rangle\langle\cos\left(m\left(\psi_m^a-\psi_m^c\right)\right)\rangle}{\langle\cos\left(m\left(\psi_m^b-\psi_m^c\right)\right)\rangle}}. \tag{4.16}$$

We can thus obtain all three event plane resolutions (for the a, b and c subevents) by measuring the correlation between the respective event planes over a large number of event. However, this resolution contributes to the uncertainty in the flow harmonic measurement. In particular, in the case of the 4^{th}order event plane for the VZERO detectors, the event planes correlation $\cos\left(k\left(\psi_{4,\text{V0A}}-\psi_{4,\text{V0C}}\right)\right)$ will take the values 1 or -1 almost equally often, averaging to a quantity close to 0 with a relatively large uncertainty, which is the cause of the very large systematic errors we obtain at this order for calculations involving these detectors.

4.3 Q-Cumulants Method

Another method for flow coefficient and mixed harmonics calculations is the direct use of the flow vectors introduced in Section 4.1 via cumulants. We denote $c_n\{2\}$ the two-particles cumulant and $v_n\{2\}$ the nth flow coefficient measured using a 2-particles cumulant. It can be shown [70] that :

$$v_n\{2\}=\sqrt{c_n\{2\}}\quad\text{and}\quad v_n\{4\}=-\sqrt[4]{c_n\{4\}}. \tag{4.17}$$

Reference [70] also gives the expression for the 2- and 4-particle cumulants:

$$c_n\{2\}=\langle\langle e^{in(\phi_1-\phi_2)}\rangle\rangle \tag{4.18}$$

where the inner brackets represent an average over the particles of one event or subevent, and the outer brackets the average over a large number of events. Let us look in closer details at these averages.

$$\langle e^{in(\phi_1-\phi_2)}\rangle = \frac{1}{M\,(M-1)}\sum_{\substack{i,j=0\\ i\neq j}}^{M} e^{in(\phi_i-\phi_j)} = \frac{1}{M\,(M-1)}\left(\sum_{i,j=0}^{M} e^{in(\phi_i-\phi_j)} - M\right), \tag{4.19}$$

where the M diagonal terms have been subtracted in the right hand side of the equation. This quantity can be expressed in terms of the flow vectors that have been introduced in section 4.1, since $\sum_{i=0}^{M} e^{(in\phi_i)} = Q_n^x + iQ_n^y = Q_n$, the complex notation of the flow vector. Our 2-particles correlations can thus be expressed in terms of the Q-vectors:

$$\langle e^{in(\phi_1-\phi_2)}\rangle = \frac{Q_n Q_n^* - M}{M\,(M-1)} = \frac{|Q_n|^2 - M}{M\,(M-1)}. \tag{4.20}$$

When averaging this quantity over many events to obtain the 2-particles cumulant, one can use event weights. Typically, these will be equal to the number of terms in the sum, in this case $M\,(M-1)$:

$$c_n\{2\} = \frac{\sum |Q_n|^2 - M}{\sum M\,(M-1)}. \tag{4.21}$$

The 4-particles cumulant can be shown [70] to be given by:

$$c_n\{4\} = \langle\langle e^{in(\phi_1+\phi_2-\phi_3-\phi_4)}\rangle\rangle - 2\cdot\langle\langle e^{in(\phi_1-\phi_2)}\rangle\rangle^2, \tag{4.22}$$

where, similarly to the 2-particles cumulant discussed previously, we can express the 4-particles correlations in terms of flow vectors [71]:

$$\begin{aligned}&\langle e^{in(\phi_1+\phi_2-\phi_3-\phi_4)}\rangle = \\ &\frac{|Q_n|^4 + |Q_{2n}|^2 - 2\Re\left(Q_{2n}Q_n^*Q_n^*\right) - 2\,(M-2)\,|Q_n|^2 - M\,(M-3)}{M\,(M-1)\,(M-2)\,(M-3)},\end{aligned} \tag{4.23}$$

where the terms on the right side of $|Q_n|^4$ again represent the removal of diagonal terms.

4.4 Acceptance Corrections

We have so far assumed perfect detectors and neglected acceptance effects in the flow calculation equations. In reality, the efficiency of the detectors will be a function of the phase space variables, and in particular, in this analysis, azimuthal angles. For a detector with uniform acceptance, we should have $\langle Q_n^x \rangle = 0$, $\langle Q_n^y \rangle = 0$. The impact of the dominant contribution to these acceptance effects is proportional to $\langle\langle \cos(n\phi) \rangle\rangle$ and $\langle\langle \sin(n\phi) \rangle\rangle$, and introduces an extra term to Equation 4.21 [71]:

$$\begin{aligned} c_n\{2\} = \frac{\sum |Q_n|^2 - M}{\sum M(M-1)} - \Re\big[(\langle\langle \cos(n\phi) \rangle\rangle + i\langle\langle \sin(n\phi) \rangle\rangle) \times \\ (\langle\langle \cos(n\phi) \rangle\rangle - i\langle\langle \sin(n\phi) \rangle\rangle) \big] \\ = \frac{\sum |Q_n|^2 - M}{\sum M(M-1)} - \langle\langle \cos(n\phi) \rangle\rangle^2 - \langle\langle \sin(n\phi) \rangle\rangle^2. \end{aligned} \tag{4.24}$$

In Equation 4.24, $\langle \cos(n\phi) \rangle = X_n$, $\langle \sin(n\phi) \rangle = Y_n$ and $\langle\langle \cos(n\phi) \rangle\rangle = \bar{X}_n$, $\langle\langle \sin(n\phi) \rangle\rangle = \bar{Y}_n$. We will correct for acceptance effects by recentering the distribution of the flow vectors components X_n and Y_n. The procedure for this recentering involves the subtraction of the average of these components over all events, calculated independently for each data run number to account for the variation in azimuthal coverage. The new flow vector is

$$\mathbf{Q_n} = \left(\frac{X_n - \bar{X}_n}{\sqrt{\bar{X}_n^2 - \bar{X}_n{}^2}}, \frac{Y_n - \bar{Y}_n}{\sqrt{\bar{Y}_n^2 - \bar{Y}_n{}^2}} \right). \tag{4.25}$$

The recentered components verify $\langle\langle \cos(n\phi) \rangle\rangle = 0$ and $\langle\langle \sin(n\phi) \rangle\rangle = 0$, and we can use Equation 4.21 with the recentered Q-vectors without additional corrections.

4.5 VZERO Gain Corrections

The geometry of the VZERO detectors is such that for a large number of events, one would expect the average gain for every sector of a layer to be equal, due to the azimuthal symmetry of the detector. However, as can be seen in Figure 4.1, the average gain fluctuates from channel to channel. VZERO gain recalibration corrects these effects by equalizing the

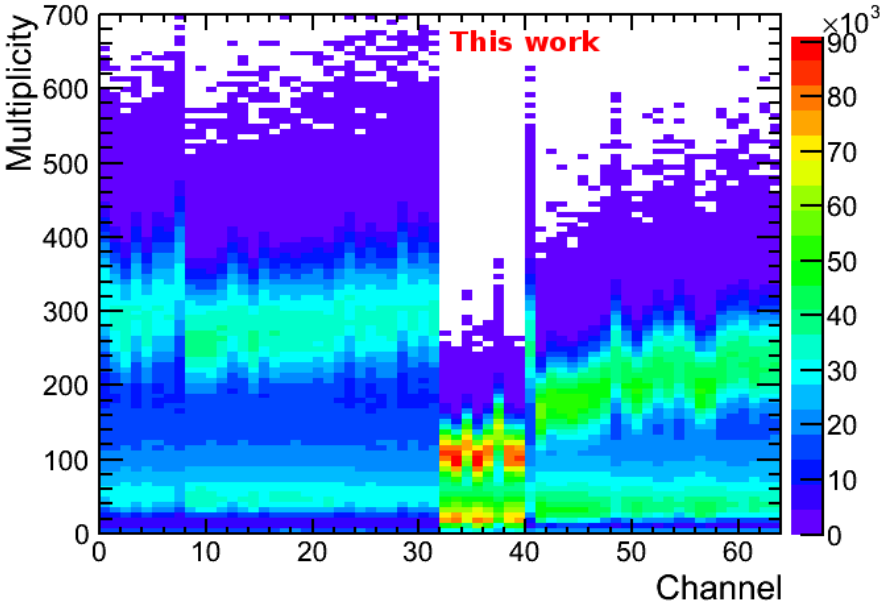

Figure 4.1: Number of counts (color scale) for each value of multiplicity (y-axis) in each channel (x-axis) of the VZERO detector, during run 170040.

average gain of all channels and setting it to the global average (over all channels) for the detector. This procedure is performed separately for the A and C sides. The procedure for this recalibration is the following: after collecting the gain data for all channels in a single run, the average gain for each side is obtained via a linear fit. Thereafter, new gains are calculated for each event and each channel:

$$G'(i) = G_i \cdot \frac{\bar{\bar{G}}}{\bar{G}_i}. \tag{4.26}$$

In Equation 4.26, G_i is the gain of channel i for a single event, $\bar{G}_i$ the gain for the same channel over all events in the run, and $\bar{\bar{G}}$ the average over all events and all channels.

4.6 Event and Particle Selection

The analysis presented in this thesis is based on Pb-Pb data taken by the ALICE experiment at $\sqrt{s_{NN}} = 2.76$ TeV. The data are composed of the second reconstruction pass of runs from years 2010 and 2011, LHC10h and LHC11h. 2010 events are selected using the minimum bias trigger, while 2011 events consists of minumum bias, central and mid-central triggers.

List of 2010 runs used in the analysis: 137161 137162 137231 137232 137235 137236 137243 137366 137430 137431 137432 137434 137439 137440 137441 137443 137530 137531 137539 137541 137544 137546 137549 137595 137608 137638 137639 137685 137686 137691 137692 137693 137704 137718 137722 137724 137751 137752 137844 137848 138190 138192 138197 138201 138225 138364 138396 138438 138439 138442 138469 138534 138578 138583 138621 138624 138638 138652 138653 138662 138666 138730 138732 138837 138870 138871 138872 139028 139029 139036 139037 139038 139042 139104 139105 139107 139173 139309 139310 139311 139314 139328 139329 139360 139437 139438 139439 139440 139465 139503 139505 139507

List of 2011 runs used in the analysis: 168464 169099 169550 169588 170207 168512 169555 169969 170268 169045 169515 169586 170040 170311 169506 168076 169238 170084 170228 168105 170312 168311 167987 169138 167920 168511 170163 168069 170159 169846 170089 169094 169040 169156 168208 168207 170390 168318 169498 170204 170306 169148 170081 170270 170091 168361 170203 169420 169035 169145 170309 169838 170388 168342 168108 169835 170027 169504 167915 169417 169160 168206 169167 167988 170556 168467 168181 168175 168322 168514 168341 170155 169965 169144 168107 170315 168362 169044 169533 169590 169858 168213 170036 169418 170085 170308 169859 167985 169557 170193

169411

Track selection is based on the AOD filter mask 128. This includes a minimum number of 70 TPC clusters, and a tracking fit χ^2 of less than 4. The estimated closest distance between the track and the vertex, called distance of closest approach (DCA) is lower than 2.4 cm in the radial direction and 3.2 cm along the beam axis. The pseudorapidity range is restricted to $-0.8 < \eta < 0.8$, smaller than the $0.9 > |\eta|$ nominal TPC range, to reduce systematic errors from border effects.

4.7 Observables Used in this Analysis

In the analysis presented in this dissertation, we measure the second- and fourth-harmonic correlators. The following is a description of the various methods used to obtain these measurements. The equation used to perform the calculation of the correlators based on the VZERO event planes can be obtained from the general expression of the correlator $\langle\cos(\phi_\alpha + \phi_\beta - 2\psi)\rangle$:

$$\begin{aligned}
\langle\cos(\phi_\alpha + \phi_\beta - 2\psi)\rangle &= \langle\Re\left(\exp\left(i\left(\phi_\alpha + \phi_\beta - 2\psi\right)\right)\right)\rangle \\
&= \Re\left(\frac{\sum_{\substack{\alpha,\beta=0 \\ \alpha\neq\beta}}^{M_\alpha, M_\beta} \exp\left(i\left(\phi_\alpha + \phi_\beta - 2\psi\right)\right)}{n_{\text{pairs}}}\right) \\
&= \Re\left(\frac{\sum_{\substack{\alpha,\beta=0 \\ \alpha\neq\beta}}^{M_\alpha, M_\beta} e^{(i\phi_\alpha)} e^{\left(i\phi_\beta\right)} \left(\cos(2\psi) - i\sin(2\psi)\right)}{n_{\text{pairs}}}\right).
\end{aligned} \tag{4.27}$$

We use α and β indices to qualify the set of particles of a particular charge within selection cuts. n_{pairs} corresponds to the number of pairs that can be made with the running α and β indices; it corresponds to the number of terms in the sum. Two cases arise at this point: in the equation corresponding to opposite-charge correlators, the α and β sets of particles are distinct and no diagonal terms have to be accounted for; in the equation corresponding to same-charge correlator, the $\alpha = \beta$ terms need to be removed when simplifying the sum in the last line of Equation 4.27. Let us consider the latter case. Replacing the exponential terms in Equation 4.27 with the Q-vector equivalents :

$$\begin{aligned}
&\langle \cos(\phi_\alpha + \phi_\alpha - 2\psi)\rangle = \\
&\Re\left(\frac{\left(\left(\sum_{\alpha=0}^{M_\alpha} e^{(i\phi_\alpha)}\right)^2 - \sum_{\alpha=0}^{M_\alpha} e^{(2i\phi_\alpha)}\right)(\cos(2\psi) - i\sin(2\psi))}{M_\alpha(M_\alpha - 1)}\right) \\
&= \Re\left(\frac{((X_{1,\alpha} + iY_{1,\alpha})(X_{1,\alpha} + iY_{1,\alpha}) - (X_{2,\alpha} + iY_{2,\alpha}))(\cos(2\psi) - i\sin(2\psi))}{M_\alpha(M_\alpha - 1)}\right) \\
&= \frac{1}{M_\alpha(M_\alpha - 1)}\left[\left(X_{1,\alpha}^2 - Y_{1,\alpha}^2 - X_{2,\alpha}\right)\cos(2\psi) + (2\cdot X_{1,\alpha}Y_{1,\alpha} - Y_{2,\alpha})\sin(2\psi)\right].
\end{aligned} \tag{4.28}$$

When deriving the equation for the opposite-charge correlator, no diagonal terms have to be subtracted. The final expression for this correlator is then:

$$\begin{aligned}
&\langle \cos(\phi_\alpha + \phi_\beta - 2\psi)\rangle = \\
&\frac{1}{M_\alpha M_\beta}\left[(X_{1,\alpha}X_{1,\beta} - Y_{1,\alpha}Y_{1,\beta})\cos(2\psi) + (X_{1,\alpha}Y_{1,\beta} + X_{1,\beta}Y_{1,\alpha})\sin(2\psi)\right].
\end{aligned} \tag{4.29}$$

The ψ event plane angle is estimated using the second order event plane obtained from the VZERO detectors, $\psi_{2,\text{VZERO}}$, and dividing $\langle \cos(\phi_\alpha + \phi_\beta - 2\psi_{2,\text{VZERO}})\rangle$ by the corresponding event plane resolution. The fourth-harmonic correlator is calculated following the same guidelines, but a final step must be added after obtaining the fourth-order equivalent to the last line of Equation 4.28. Because of the geometry considerations of the VZERO detector,

$\cos(\psi_{4,VZERO}) = 0$. This is a detector effect that needs to be corrected for. This can be done by noting that the sine and cosine terms of the final line of Equation 4.28 should be equal due to azimuthal symmetry, after averaging over all events. The opposite-charge and same-charge correlators become:

$$\begin{aligned}\langle\cos(2\phi_\alpha + 2\phi_\beta - 4\psi)\rangle &= \frac{2\left[(X_{2,\alpha}Y_{2,\beta} + X_{2,\beta}Y_{2,\alpha})\sin(4\psi_{4,\mathrm{VZERO}})\right]}{R_{4,\mathrm{VZERO}}M_\alpha M_\beta} \\ \langle\cos(2\phi_\alpha + 2\phi_\alpha - 4\psi)\rangle &= \frac{2\left[(2\cdot X_{2,\alpha}Y_{2,\alpha} - Y_{4,\alpha})\sin(4\psi_{4,\mathrm{VZERO}})\right]}{R_{4,\mathrm{VZERO}}M_\alpha(M_\alpha - 1)}.\end{aligned} \tag{4.30}$$

Another measurement of the correlators will be calculated using exclusively TPC particles:

$$\langle\cos(\phi_a + \phi_b - 2\phi_c)\rangle = v_{2,c}\langle\cos(\phi_a + \phi_b - 2\psi)\rangle \tag{4.31}$$

In the analysis presented in this thesis, we will calculate the event-plane dependent correlator using the left-hand side of Equation 4.31 and $v_{2,c}$ ($v_{4,c}$) measurements published by the ALICE collaboration.

$$\begin{aligned}\langle\cos(\phi_\alpha + \phi_\beta - 2\phi_c)\rangle &= \langle\Re\left(\exp\left(i\left(\phi_\alpha + \phi_\beta - 2\phi_c\right)\right)\right)\rangle \\ &= \Re\left(\frac{\sum_{\substack{\alpha,\beta,c=0 \\ \alpha\neq\beta\neq c}}^{M_\alpha,M_\beta,M_c}\exp\left(i\left(\phi_\alpha + \phi_\beta - 2\phi_c\right)\right)}{n_{\mathrm{terms}}}\right).\end{aligned} \tag{4.32}$$

Using the Q-vector components similarly to the derivation of Equation 4.28, we obtain a set of four equations, depending on the overlap between particle sets α, β and c. If α and β

belong to the same set and overlap with c:

$$\begin{aligned}
&\langle \cos\left(\phi_\alpha + \phi_\beta - 2\phi_c\right)\rangle = \\
&\frac{1}{M_\alpha\left(M_\alpha - 1\right)\left(M_c - 2\right)}\Bigg[\left(\sum_{\alpha=0}^{M_\alpha} e^{(i\phi_\alpha)}\right)^2\left(\sum_{c=0}^{M_c} e^{(-2i\phi_c)}\right) - \\
&\left(\sum_{\alpha=0}^{M_\alpha} e^{(2i\phi_\alpha)}\right)\left(\sum_{c=0}^{M_c} e^{(-2i\phi_c)}\right) - \\
&2\left(\sum_{\alpha=0}^{M_\alpha} e^{(i\phi_\alpha)}\right)\left(\sum_{c=0}^{M_c} e^{(-i\phi_c)}\right) + 2\cdot M_\alpha\Bigg] \\
&= \frac{1}{M_\alpha\left(M_\alpha - 1\right)\left(M_\alpha - 2\right)}\Big[X_{1,\alpha}X_{1,\alpha}X_{2,\alpha} - Y_{1,\alpha}Y_{1,\alpha}X_{2,\alpha} + \\
&X_{1,\alpha}Y_{1,\alpha}Y_{2,c} - X_{2,\alpha}X_{2,c} - Y_{2,\alpha}Y_{2,c} - 2X_{1,\alpha}X_{1,c} - 2Y_{1,\alpha}Y_{1,c} + 2M_\alpha\Big].
\end{aligned} \tag{4.33}$$

If α and β belong to different sets with the c set composed of α and β combined:

$$\begin{aligned}
&\langle \cos\left(\phi_\alpha + \phi_\beta - 2\phi_c\right)\rangle = \\
&\frac{1}{M_\alpha M_\beta\left(M_\alpha + M_\beta - 1\right)}\Bigg[\left(\sum_{\alpha=0}^{M_\alpha} e^{(i\phi_\alpha)}\right)\left(\sum_{\beta=0}^{M_\beta} e^{\left(i\phi_\beta\right)}\right) \\
&\left(\sum_{\alpha=0}^{M_\alpha} e^{(-2i\phi_\alpha)} + \sum_{\beta=0}^{M_\beta} e^{\left(-2i\phi_\beta\right)}\right) - \\
&\left(\sum_{\alpha=0}^{M_\alpha} e^{(i\phi_\alpha)}\right)\left(\sum_{\beta=0}^{M_\beta} e^{\left(-i\phi_\beta\right)}\right) - \left(\sum_{\alpha=0}^{M_\alpha} e^{(-i\phi_\alpha)}\right)\left(\sum_{\beta=0}^{M_\beta} e^{\left(i\phi_\beta\right)}\right)\Bigg] \\
&= \frac{1}{M_\alpha M_\beta\left(M_\alpha + M_\beta - 1\right)}\Big[X_{1,\alpha}X_{1,\beta}\left(X_{2,\alpha} + X_{2,\beta}\right) + \\
&\left(X_{1,\alpha}Y_{1,\beta} + Y_{1,\alpha}X_{1,\beta}\right)\left(X_{2,\alpha} + X_{2,\beta}\right) - Y_{1,\alpha}Y_{1,\beta}\left(X_{2,\alpha} + X_{2,\beta}\right) - \\
&2X_{1,\alpha}X_{1,\beta} - 2Y_{1,\alpha}Y_{1,\beta}\Big].
\end{aligned} \tag{4.34}$$

If the c particle set does not intersect with the α or β particle sets, we can extrapolate

from 4.28

$$\begin{aligned}&\langle\cos\left(\phi_\alpha+\phi_\alpha-2\phi_c\right)\rangle=\\&\frac{1}{M_cM_\alpha\left(M_\alpha-1\right)}\left[\left(X_{1,\alpha}^2-Y_{1,\alpha}^2-X_{2,\alpha}\right)X_{2,c}+\left(2\cdot X_{1,\alpha}Y_{1,\alpha}-Y_{2,\alpha}\right)Y_{2,c}\right]\end{aligned}\tag{4.35}$$

for the same-charge correlator and

$$\begin{aligned}&\langle\cos\left(\phi_\alpha+\phi_\beta-2\phi_c\right)\rangle=\\&\frac{1}{M_cM_\alpha M_\beta}\left[\left(X_{1,\alpha}X_{1,\beta}-Y_{1,\alpha}Y_{1,\beta}\right)X_{2,c}+\left(X_{1,\alpha}Y_{1,\beta}+X_{1,\beta}Y_{1,\alpha}\right)Y_{2,c}\right]\end{aligned}\tag{4.36}$$

for the opposite-charge correlator. The fourth-harmonic correlators are calculated from Equations 4.33 to 4.36 by doubling the indices of the Q-Vector components.

Chapter 5

Experimental Results

5.1 Previous STAR and ALICE Results for the CME correlators

Several sets of results based on heavy ion collisions have been published in the past concerning the search for strong-CP violation [28, 72]. A large part of these results are based on the charge-dependent mixed-harmonic correlators with respect to the reaction plane introduced in Chapter 4. A simular pattern arises both in results gathered by the STAR experiment (Au-Au at $\sqrt{s_{NN}} = 200$ GeV) and ALICE (Pb-Pb at $\sqrt{s_{NN}} = 2.76$ TeV): significant correlations appear in the case of same-charge pairs while the opposite-charge correlators are closer to zero in central and mid-central collisions. Simple HIJING Monte-Carlo simulations, which do not model $\mathcal{P}$-violating effects, do not reproduce this difference (Figures 5.1 and 5.2).

This difference can be explained by a phenomenon similar to jet quenching: same-charge pairs created on the surface of the medium coud have similar momentum due to the CME, and fly off in a direction nearly perpendicular to the surface. However, for an opposite-charge pair created close to the surface, one of the particles has to travel through the medium and scatter with the particles composing it, and the correlation is mostly lost. The signal is stronger at lower multiplicities, but does not drop at high-$p_T$as we could expect from the non-perturbative nature of the phenomenon (Figure 5.3). The signal has a strong dependence in $\Delta\eta$. This is an interesting characteristic, as such dependences are signatures

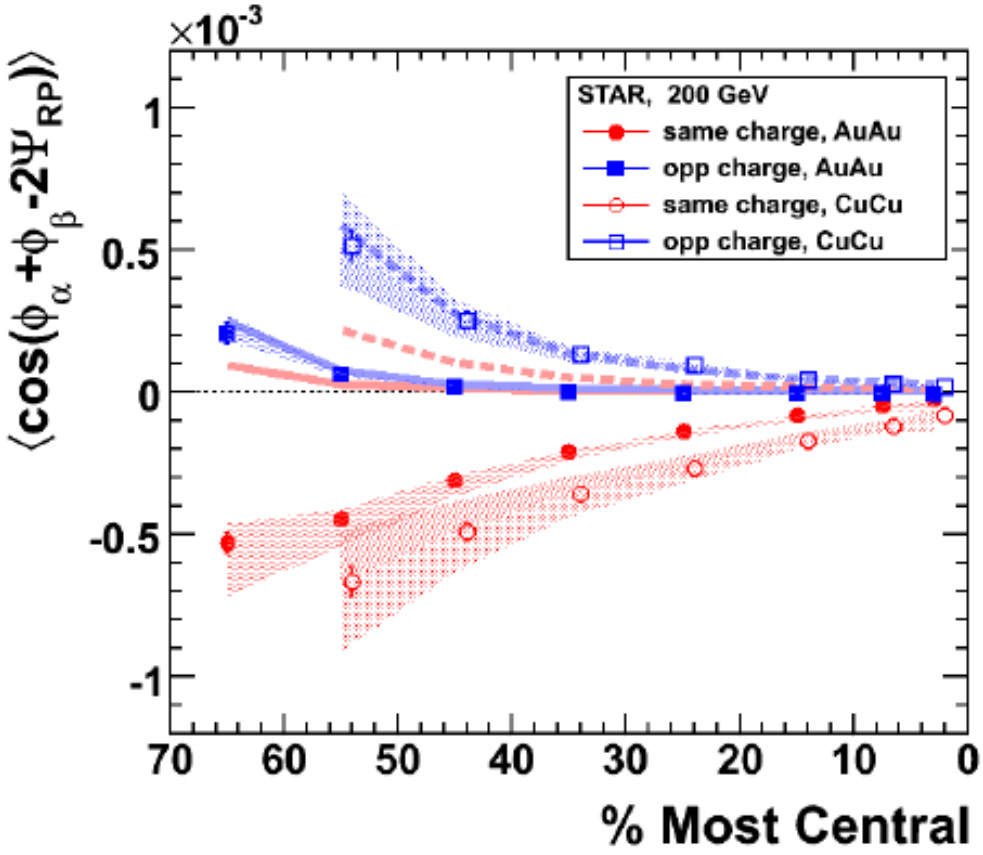

Figure 5.1: Same- and opposite-charge second harmonic correlators measured in Au-Au and Cu-Cu collisions in STAR [28].

of the range and time at which the correlation was established.

The main conclusions from the current results are:

- The correlator involving pions of different charges has a smaller value than for same-sign pions. This was expected because of the supression of back-to-back correlation observed in the medium created in those collisions (due to the strong couplings involved in the medium). This effect is weaker for Cu+Cu collisions.

- The magnitude of this effect is larger at lower energy. This is in agreement with the 1/N dependence of the P-violation effect on multiplicity. Similarly, the value is smaller

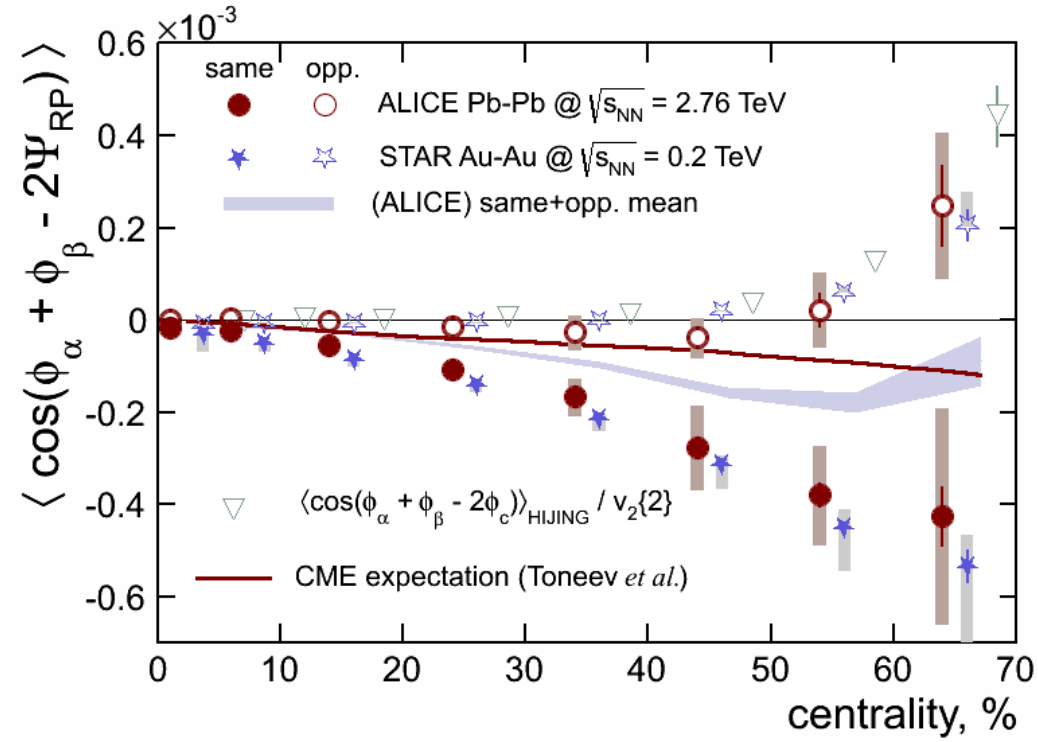

Figure 5.2: Same- and opposite-charge second harmonic correlators measured in Pb-Pb collisions in ALICE [28].

for central collisions.

- The value of the contribution from cluster correlations mentioned in Chapter 2 appears to be smaller than the experimental values of the correlator. This would tend to indicate that those contributions are not the only ones involved, but does not rule out the possibility of other non $\mathcal{P}$-violating contributions.

- One would expect the $\mathcal{P}$-violation process to only happen at low p_T, since its causes (the instantons) are inherently a non-perturbative effect. The coupling constant of QCD becoming smaller with higher energies, at high p_T, this effect should become smaller. However, the value of the correlator is higher at high transverse momentum.

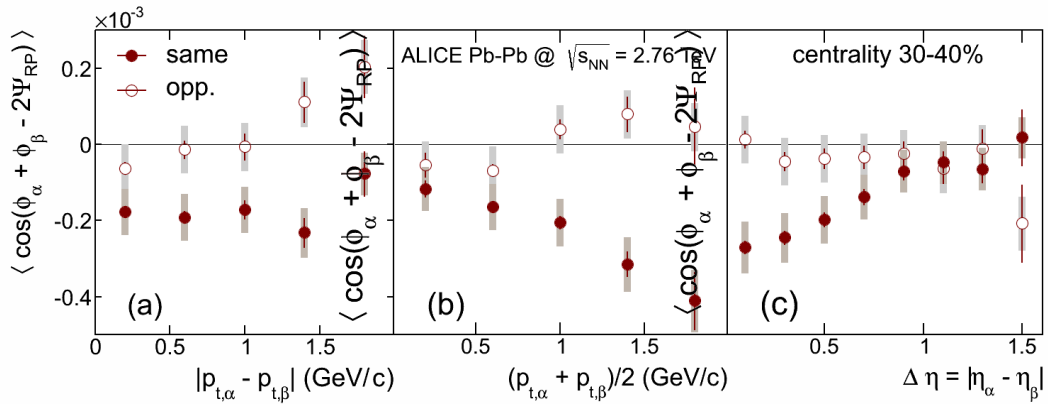

Figure 5.3: Left panel: momentum difference dependence of the same and opposite-charge second harmonic correlators. Center panel : average momentum dependence of the same and opposite-charge second harmonic correlators. Right panel: $\Delta\eta$ dependence of the same and opposite-charge second harmonic correlators [28].

5.2 Event Plane

Some of the measurements made in this analysis involve event planes calculated from the VZERO detector. It is therefore relevant to study the event plane distributions first. These distributions are shown in Figures 5.4 to 5.7. In the first two of these figures, the distribution is close to flat in the $-\pi < \psi < \pi$ range, as these are second-order event planes, with minor substructures due to residual acceptance effects that weren't completely removed by the recalibration of the VZERO channels and the recentering of the Q-Vectors used in event plane calculations. The two latter figures are fourth-order event planes. As noted in Chapter 4, at this order, due to the VZERO geometry, the distribution in event plane angles for both sides of the detector consists of two delta-function-like structures at $-\pi/8$ and $\pi/8$. This unusual event plane distribution is thus expected and not indicative of any unforeseen issue.

Figures 5.8 and 5.9 show the corresponding event plane resolutions at the second and fourth order. These resolutions are calculated using Equation 4.16, using TPC tracks ($|\eta| < 0.8$) as the 3rd subevent. The TPC event planes will not be used in this analysis and are thus not shown in the figures. We can see on Figure 5.9 the consequence of the event plane

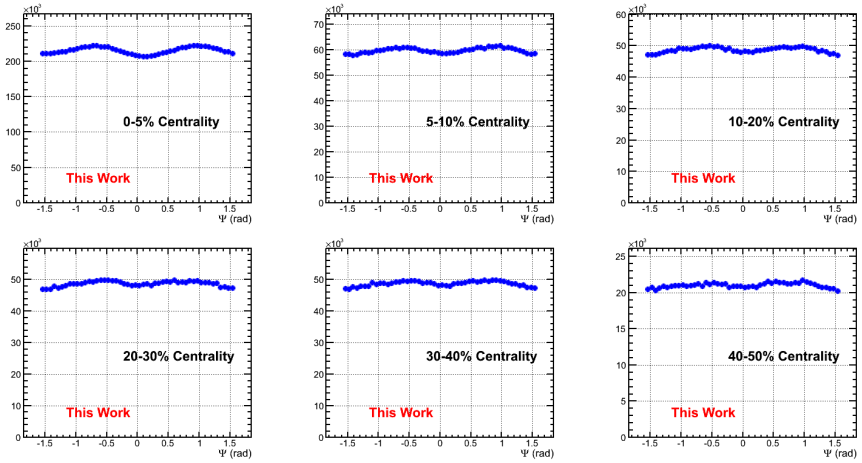

Figure 5.4: Second-order event plane $\psi_{2,V0A}$ azimuthal distribution.

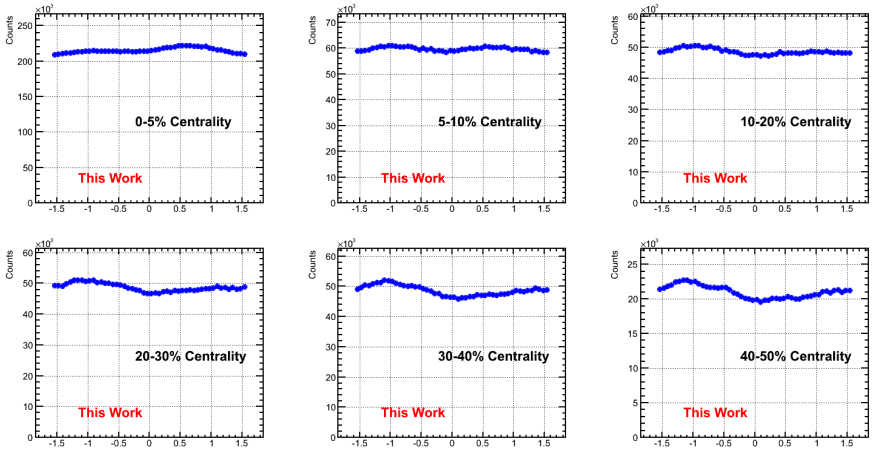

Figure 5.5: Second-order event plane $\psi_{2,V0C}$ azimuthal distribution.

distributions from Figures 5.6 and 5.7. The fourth-order event plane resolution for VZERO is quite low, with somewhat large errors; this will affect the measurements based on the VZERO event planes.

5.3 Second- and Fourth-Harmonic Correlators

The calculations of the second- and fourth-harmonic calculators presented here were introduced in Equations 4.27 to 4.36. The Q-Cumulant results shown in this section are obtained by correlating particles a and b (in $\langle\cos(\phi_a + \phi_b - 2\phi_c)\rangle$, $\langle\cos(2\phi_a + 2\phi_b - 4\phi_c)\rangle$)

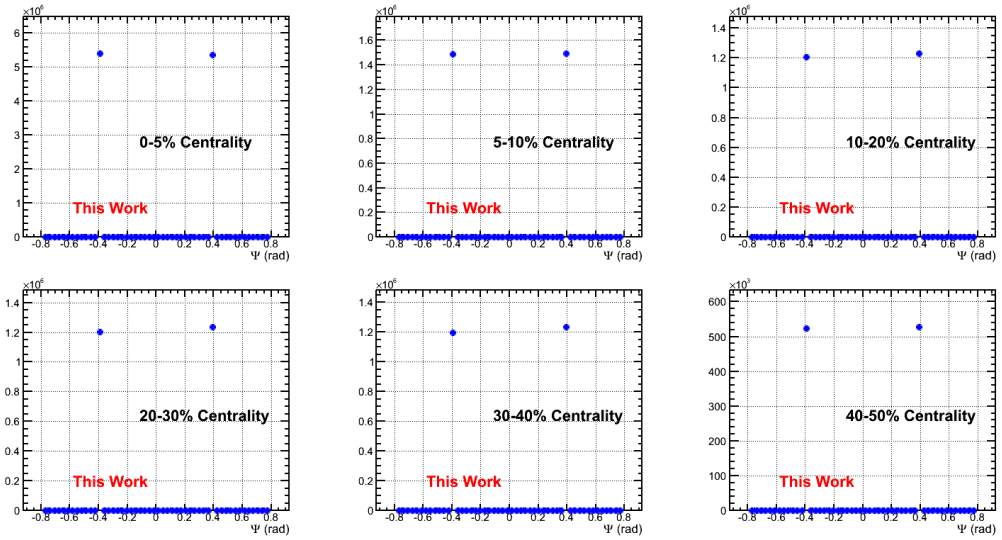

Figure 5.6: Fourth-order event plane $\psi_{4,V0A}$ azimuthal distribution for various centrality bins.

from the negative η part of the TPC with the c-particle from the positive η, then vice-versa; both results are then averaged and divided by $\frac{1}{2}\left(v_2\{2\} + v_2\{4\}\right)$ (second harmonic) or $v_4\{2\}, |\Delta\eta| > 1$ published in [32]. The results based on VZERO event planes likewise use a and b particles from half the TPC correlated with the event plane, then likewise with the other half before averaging both results and dividing by the event plane resolution.

Figure 5.10 shows the same- and opposite-charge second harmonic correlators at both the second and fourth order. The signal we observe shows similar properties to previously published analyses: a strong same-charge correlator and an opposite-charge correlator with values closer to zero between 0 and 40% centralities. The fourth harmonic signal, on the other hand, is strong and almost identical in both the same- and opposite charge correlators.

If we investigate the charge-dependence of both harmonics, we observe a significant signal in the second harmonic (Figure 5.11), but a signal consistent with zero or close to zero for the fourth harmonic5.12, which might be indicative of weak contributions from LCC. However, two things moderate this conclusion: it is necessary to understand how the LCC background scales from the fourth to the second harmonic, which will be the subject of the final chapter of this thesis; and systematic errors might change this conclusion. In particular,

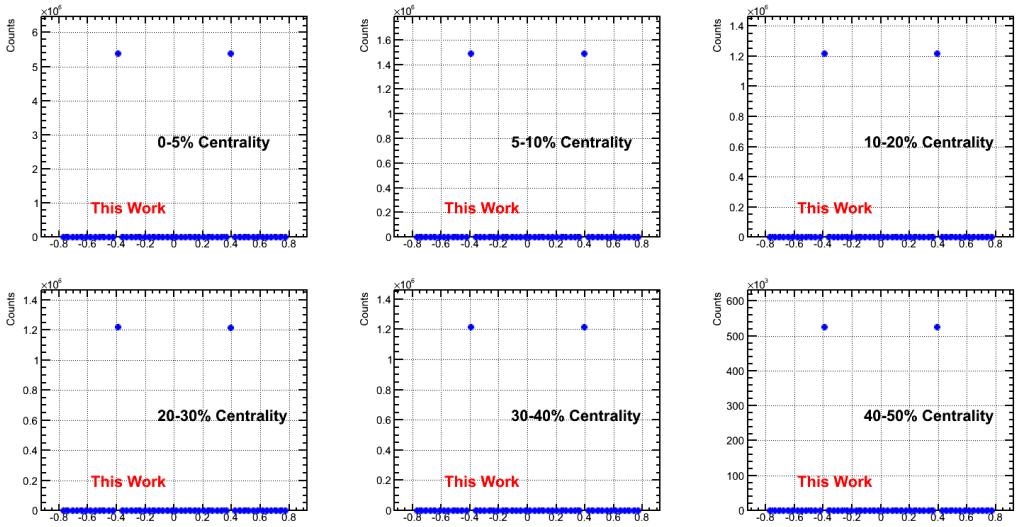

Figure 5.7: Fourth-order event plane $\psi_{4,V0C}$ azimuthal distribution for various centrality bins.

a first-order approximation tells us that

$$\frac{\Delta\langle\cos\left(2\phi+2\phi-4\psi\right)\rangle}{\Delta\langle\cos\left(\phi+\phi-2\psi\right)\rangle}\sim\frac{v_4}{v_2}\sim 0.1. \tag{5.1}$$

In Equation 5.1, the Δ sign denotes the charge-dependence, which is the difference between opposite and same charge correlators.

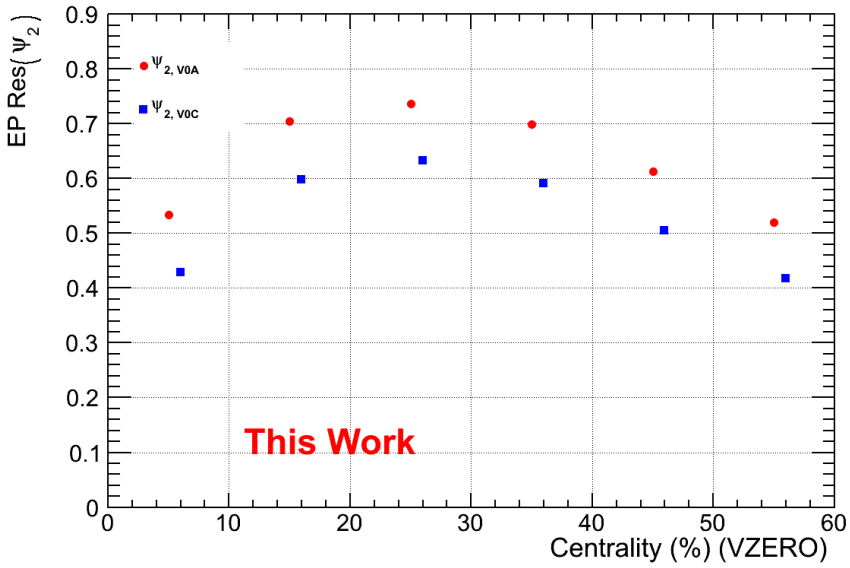

Figure 5.8: Second-order event plane resolution as a function of V0 Centrality for $\psi_{2,V0A}$ and $\psi_{2,V0A}$.

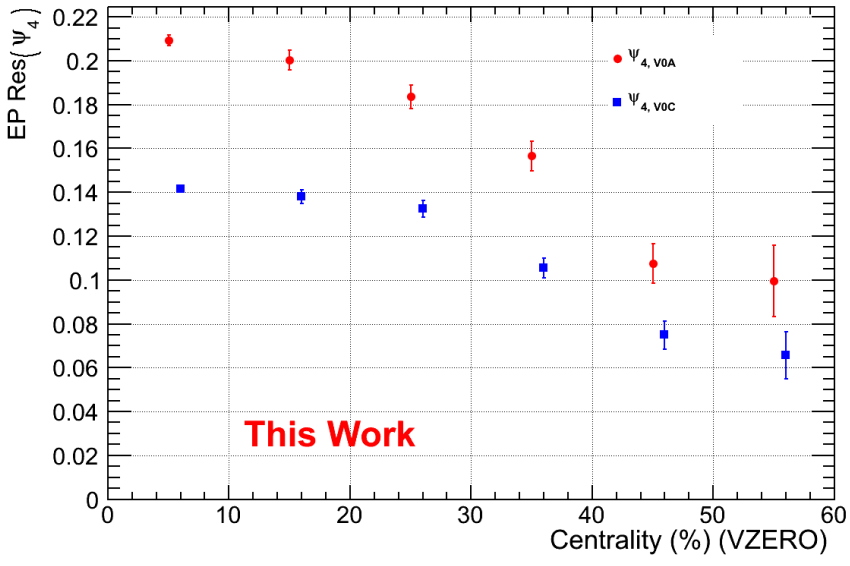

Figure 5.9: Fourth-order event plane resolution as a function of V0 Centrality for $\psi_{4,V0A}$ and $\psi_{4,V0A}$.

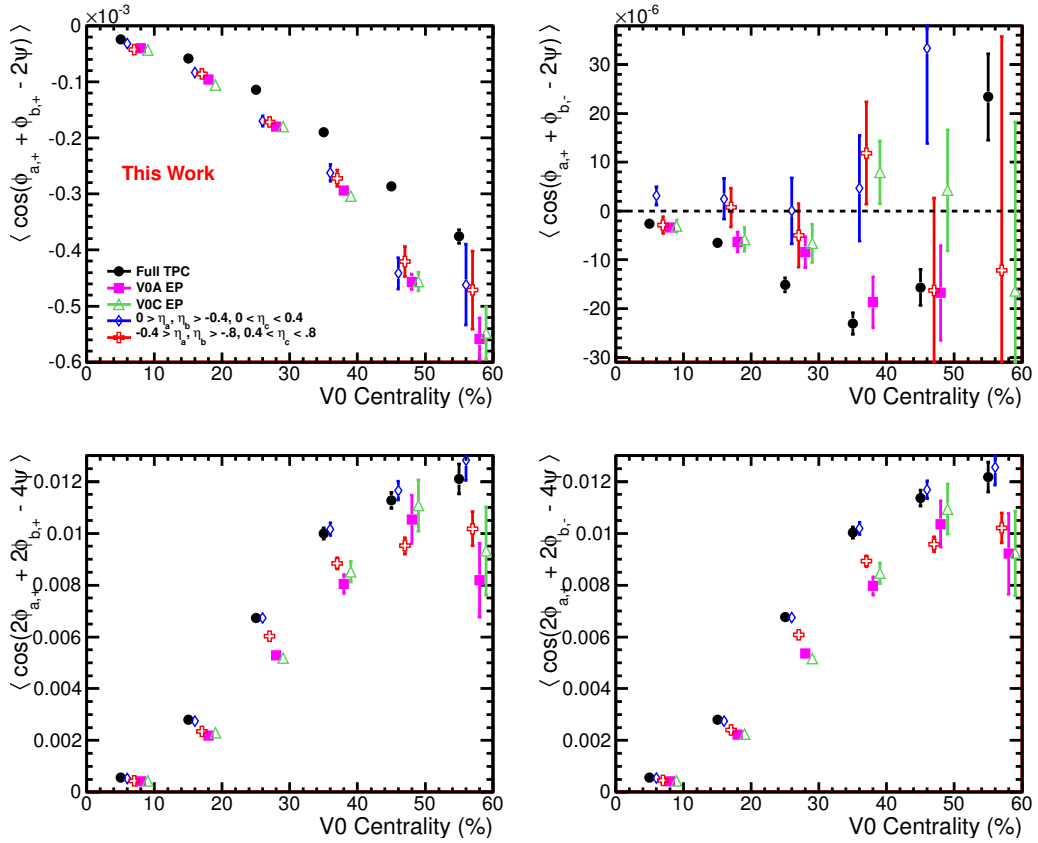

Figure 5.10: Comparison of the correlators calculated using various methods. Top-left panel: same-charge second harmonic correlator. Top-right panel: opposite-charge second harmonic correlator. Bottom-left panel: same-charge second fourth correlator. Bottom-right panel: opposite-charge fourth harmonic correlator. Pseudorapidity gaps will be discussed in the next chapter. Statistical errors only.

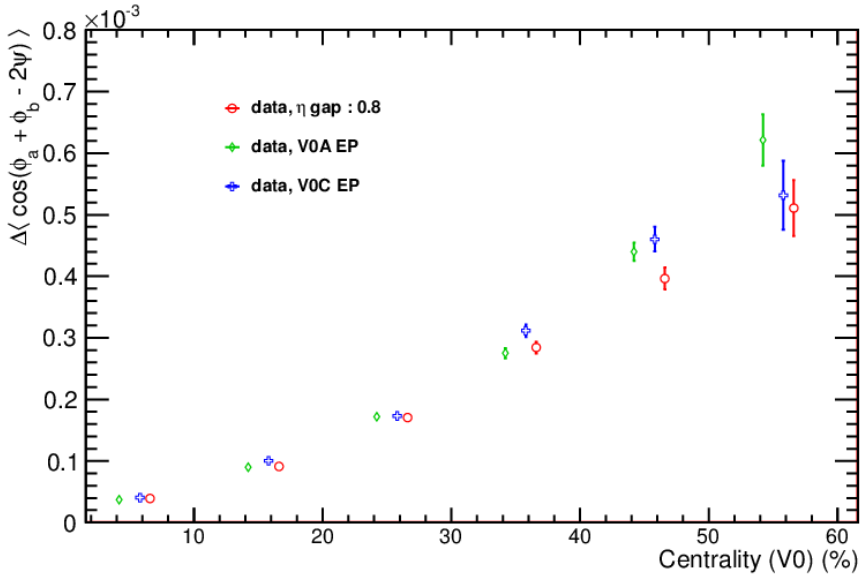

Figure 5.11: Charge-dependence of the second harmonic correlator ($\langle\cos(\phi+\phi-2\psi)\rangle_{\text{opp.}} - \langle\cos(\phi+\phi-2\psi)\rangle_{\text{same}}$) calculated with the VZERO event plane method and TPC Q-Cumulant methods (with and without pseudorapidity gaps)

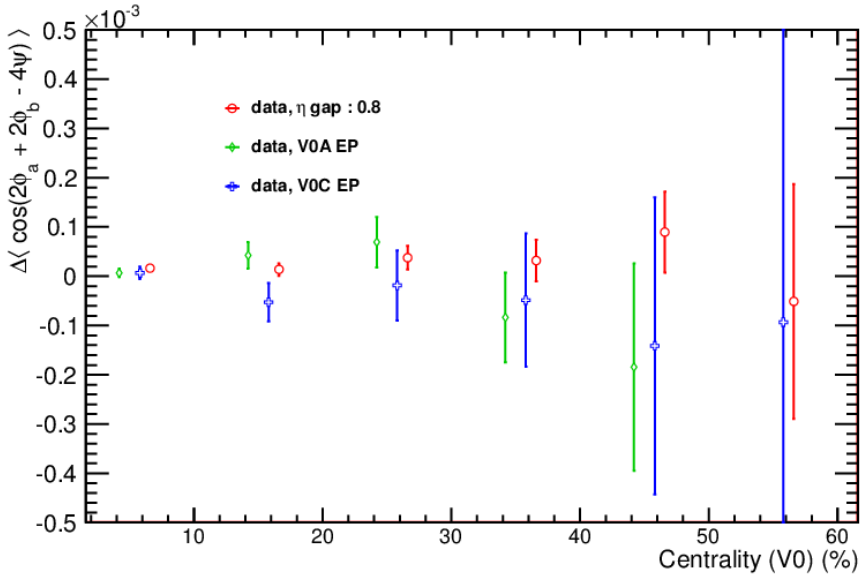

Figure 5.12: Charge-dependence of the fourth harmonic correlator ($\langle\cos(2\phi+2\phi-4\psi)\rangle_{\text{opp.}} - \langle\cos(2\phi+2\phi-4\psi)\rangle_{\text{same}}$) calculated with the VZERO event plane method and TPC Q-Cumulant methods (with and without pseudorapidity gaps)

Chapter 6

Systematic Errors

6.1 Sources of Systematic Errors

The results obtained from the analysis presented in this thesis would not be complete without the study of systematic uncertainties. These correspond to the various biases that arise from the analysis method, event and particle selection, and detector imperfections and acceptance effects. While there is no exact method to accurately calculate these effects, they can be estimated. The general method for systematic estimation is to perform the same calculation as for the main value of the final results, while varying some of the conditions under which those calculations are performed. For instance, different event or particle selection cuts can be chosen, a different centrality definition, or detector configuration. Several main sources of systematic errors have been identified in this analysis.

- Magnetic field polarization.

  The L3 solenoid magnet used for charged particles tracking is generally used in two configurations, which we will call *negative* and *positive*. These configurations are not exactly symmetrical, which can be due to an asymmetry in the field itself or in the acceptance of the tracking detector. This could results in significant differences in the correlators calculated in this analysis.

- Filter bits: particle selection cuts and tracking parameters The use of AOD track filters restricts the range of particle selection cuts that can be modified to study the associated systematic uncertainties. However, we can study the effect of a change of

filter configuration on the final results. We will look at the correlators obtained using filter bit 768, which corresponds to hybrid tracks, with global track parameters and ITS-calculated DCA when available.

- c-particle dependence.

  We define the charge-dependent second and fourth harmonics correlator with same-charge c-particle as

$$\frac{(\langle\langle\cos(\phi_+ + \phi_- - 2\phi_c)\rangle\rangle - 0.5\,(\langle\langle\cos(\phi_+ + \phi_+ - 2\phi_+)\rangle\rangle + \langle\langle\cos(\phi_- + \phi_- - 2\phi_-)\rangle\rangle))}{v_2}, \tag{6.1}$$

  and with opposite-charge c-particle

$$\frac{(\langle\langle\cos(\phi_+ + \phi_- - 2\phi_c)\rangle\rangle - 0.5\,(\langle\langle\cos(\phi_+ + \phi_+ - 2\phi_-)\rangle\rangle + \langle\langle\cos(\phi_- + \phi_- - 2\phi_+)\rangle\rangle))}{v_2}. \tag{6.2}$$

  The dependence on the charge of the c-particle doesn't affect the correlator with opposite-charge a and b particles, for symmetry reasons. However, it might affect the terms that involves same-charge a and b; this dependence appears when we select the c-particle to have the same charge (respectively opposite charge) as the two others. As shown in Figure 6.1, the results have a strong dependence on the charge of the c particle in $\langle\cos(\phi_a + \phi_b - 2\phi_c)\rangle$. We will estimate this dependence and discuss the methods used to reduce it, as well as the corresponding results. The c particle in the $\langle\cos(\phi_a + \phi_b - 2\phi_c)\rangle$ correlator plays a role similar to an event plane, and provides a way to determine the orientation of the magnetic field created by the colliding ions. As such, rejecting short range correlations with the two other particles is desirable to reduce the systematic errors that arise from this dependence, and we will introduce a pseudorapidity gap between the two sets of particles, i.e. we will confine the a and b particles to a smaller (0.4 units wide) rapidity region on one side of the TPC ($0.4 < \eta_{a,b} < 0.8$ and $-0.4 > \eta_{a,b} > -0.8$) and c on the other (respectively

$-0.4 > \eta_c > -0.8$ and $0.4 < \eta_c < 0.8$). Using a restricted pseudorapidity region will affect the main values of the correlators considering their dependence on $\Delta\eta$ (Figures 5.3, 6.2, 6.3).

- Centrality definitions.

  Since we are studying the centrality dependence of the correlators, our final results depend on the detectors used for centrality determination. The main results are obtained from VZERO, but we will estimate the corresponding systematic by looking at centralities obtained from TPC and SPD multiplicities.

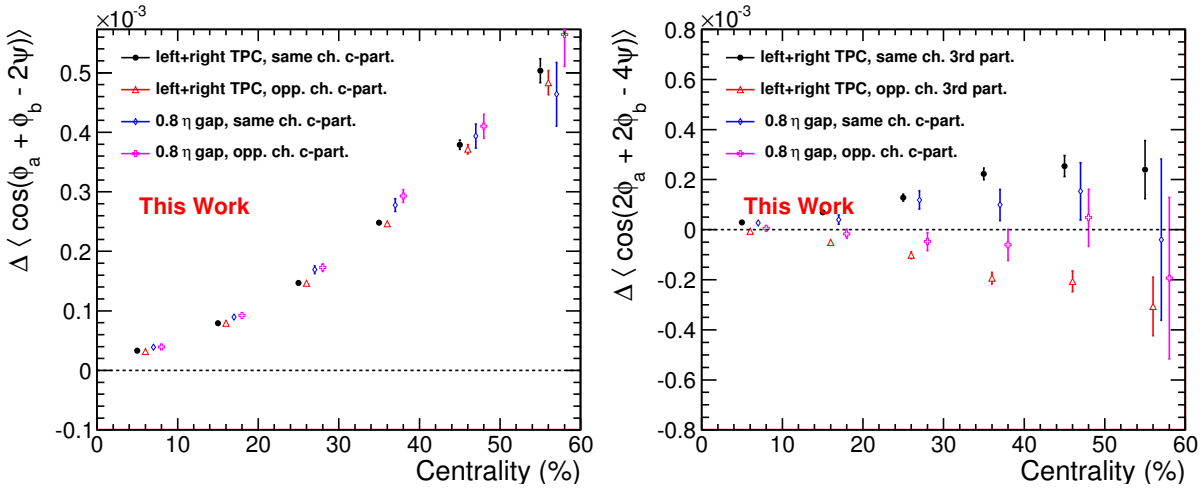

Figure 6.1: Influence of the charge of the c-particle on the values of $\langle\langle\cos(\phi_+ + \phi_- - 2\phi_c)\rangle\rangle/v_2 - 0.5\langle\langle\cos(\phi_+ + \phi_+ - 2\phi_c)\rangle\rangle/v_2 - 0.5\langle\langle\cos(\phi_- + \phi_- - 2\phi_c)\rangle\rangle/v_2$ (left panel) and $\langle\langle\cos(2\phi_+ + 2\phi_- - 4\phi_c)\rangle\rangle/v_2 - 0.5\langle\langle\cos(2\phi_+ + 2\phi_+ - 4\phi_c)\rangle\rangle/v_2 - 0.5\langle\langle\cos(2\phi_- + 2\phi_- - 4\phi_c)\rangle\rangle/v_2$ (right panel). In the graph labeled "Left + Right TPC", $0 < \eta_c < 0.8$ and $0 > \eta_{a,b} > -0.8$.

6.2 Methods for Systematic Error Calculations

In order to estimate the systematic errors, we will first calculate the charge-dependence of the fourth and second harmonic correlators, as well as their ratio, for the following configurations: $|Z_{\rm vtx}| < 10$ cm, filter bit 768 (hybrid), TPC and SPD centralities, positive and

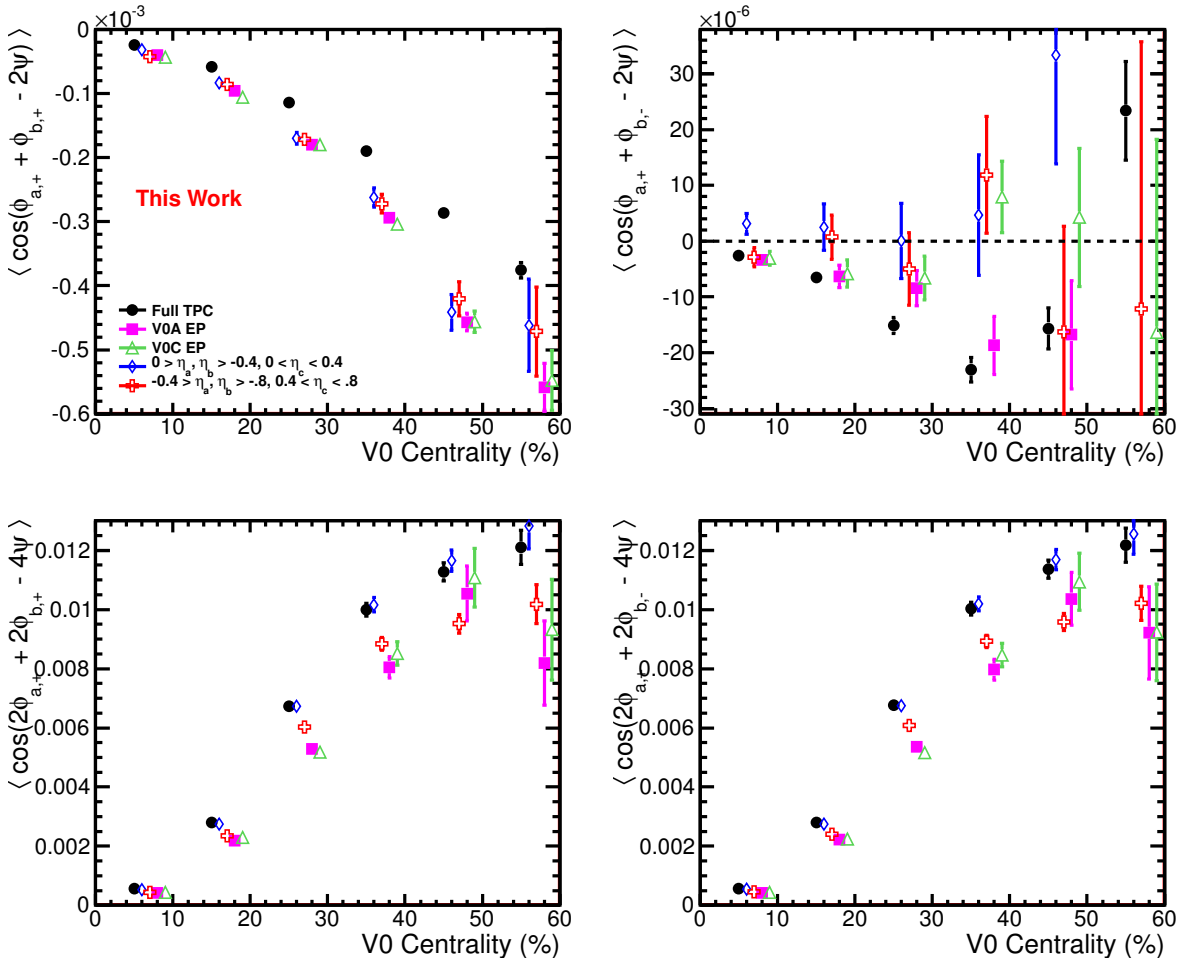

Figure 6.2: Comparison of the correlators calculated using various methods. Top-left panel: same-charge second harmonic correlator. Top-right panel: opposite-charge second harmonic correlator. Bottom-left panel: same-charge second fourth correlator. Bottom-right panel: opposite-charge fourth harmonic correlator.

negative magnetic field polarity event selections. We will also look at several selected combination of these settings to take into account the combined effect of these systematic error sources. For each of these settings, we will also look at the c-particle charge-dependence (except for the results obtained using VZERO event planes). The results of this investigation are shown on Figures 6.12 through 6.27. We observe that the most significant contributions to systematic errors come from c-particle charge dependence (when relevant) and filter bit configuration. This is easily understood when one considers that hybrid tracks contain global parameters instead of TPC-only, and have full azimuthal coverage with mixed track quality,

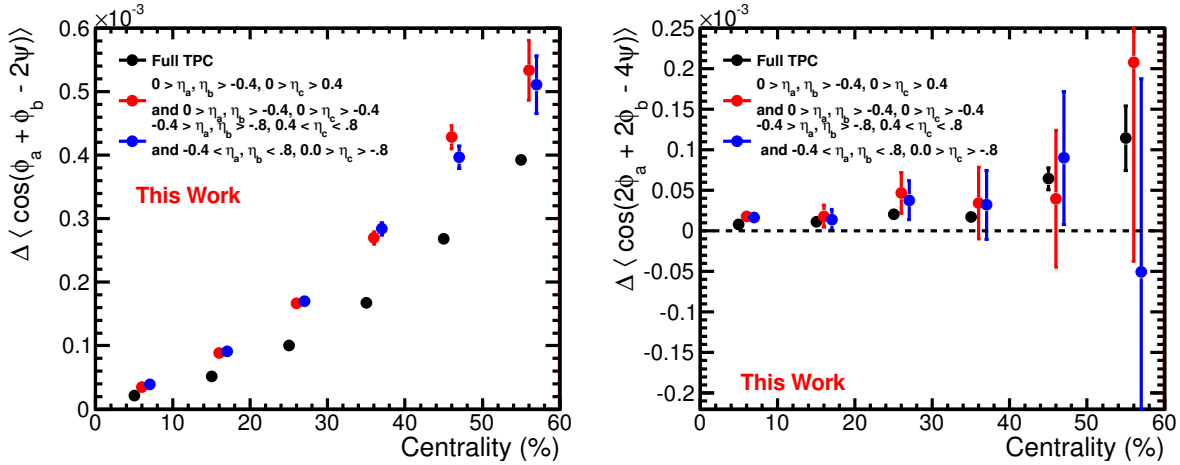

Figure 6.3: Charge-dependence of the second (left panel) and fourth (right panel) harmonic correlator calculated using Q-cumulants without several pseudorapidity range settings for the a, b and c particles $0 > \eta_{a,b} > -0.4, 0 < \eta_c < 0.4$ (averaged with the reversed range) is shown for comparison with a similar pseudorapidity range without the η gap, as the two regions are then contiguous.

the ITS covering the TPC blind zones.

For each centrality bin of the quantities that are calculated in this analysis we select the highest and lowest value of all the corresponding quantities obtained in these systematic errors studies; the set of highest values is our first estimate of the higher boundaries of the systematic errors, while the set of lower values gives the lower boundaries.

We expect the systematic errors to be a smooth function of centrality. However, statistical fluctuations of the quantities used for systematic error derivation give more irregular results; this is partially corrected using a second-order polynomial fit which is then used as the final estimation of the systematic errors (example provided on Figure 6.28).

6.3 Estimates of the Systematic Errors

Figures 6.29 and 6.30 show the second and fourth harmonic correlators with combined statistical and systematic errors, the latter having been estimated using the methods discussed in this chapter. The results from VZERO event plane give the best results for most centralities especially for the fourth harmonic correlator. The c-particle charge dependence

and strong filter bit dependence of the Q-cumulant based results give rise to much larger systematic errors. However, the fourth order event plane resolution gives rise to large statistical errors for the results based on VZERO event planes.

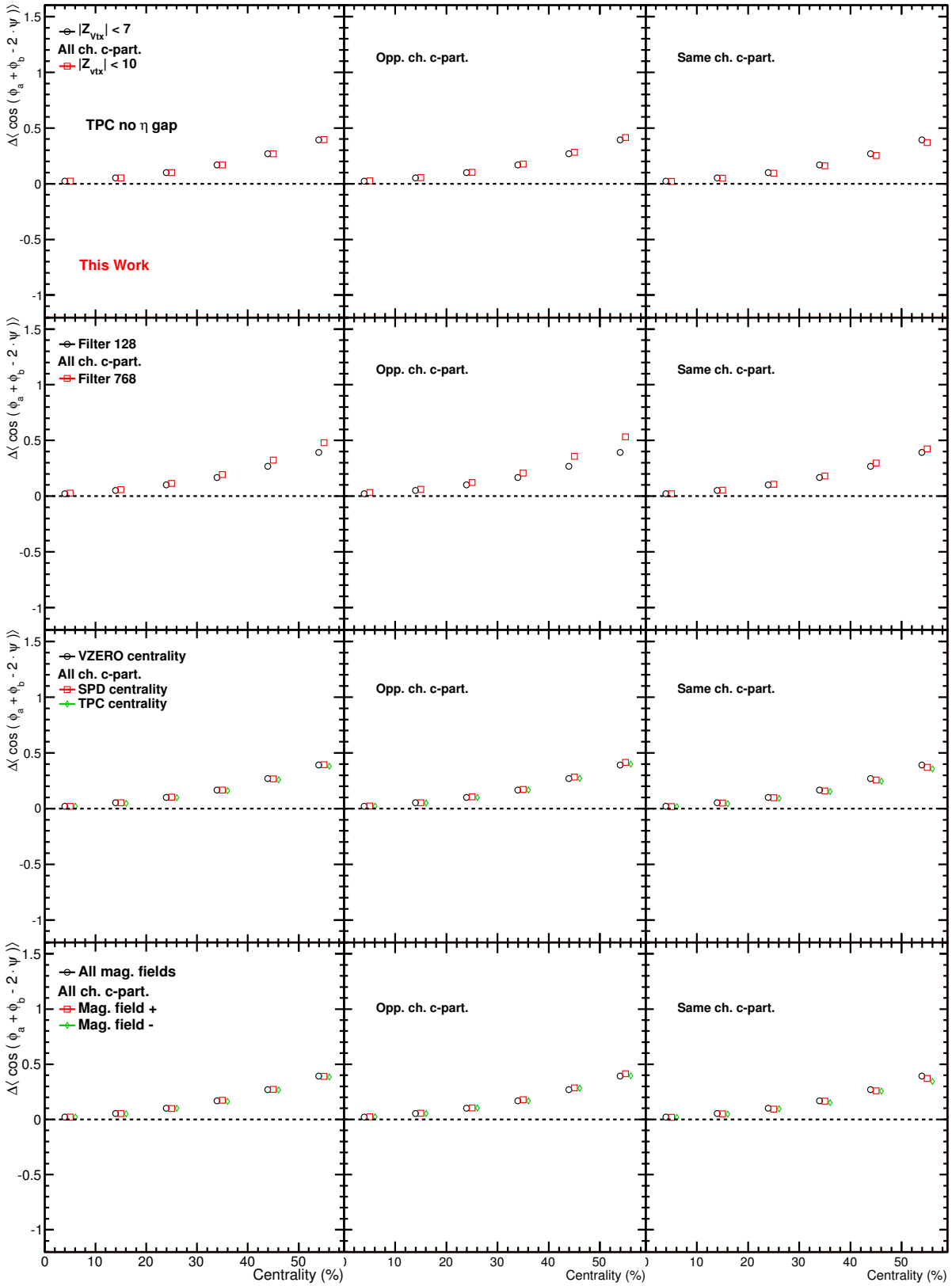

Figure 6.4: Charge-dependence of the second harmonic correlator calculated using Q-cumulants without pseudorapidity gaps for multiple event and particle cuts. Left panel is without restriction on the c-particle, central panel with same-charge c-particle and right panel with opposite-charge c-particle.

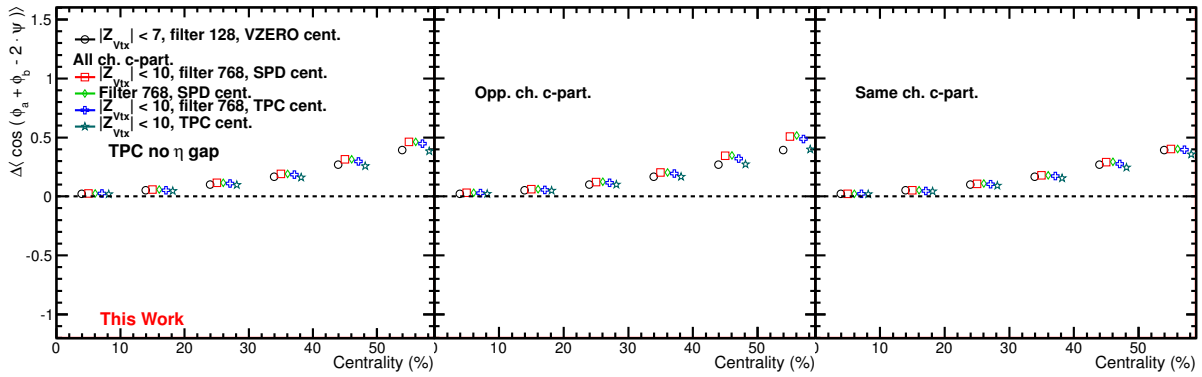

Figure 6.5: Charge-dependence of the second harmonic correlator calculated using Q-cumulants without pseudorapidity gaps for multiple event and particle cuts used simultaneously in different combinations. Left panel is without restriction on the c-particle, central panel with same-charge c-particle and right panel with opposite-charge c-particle.

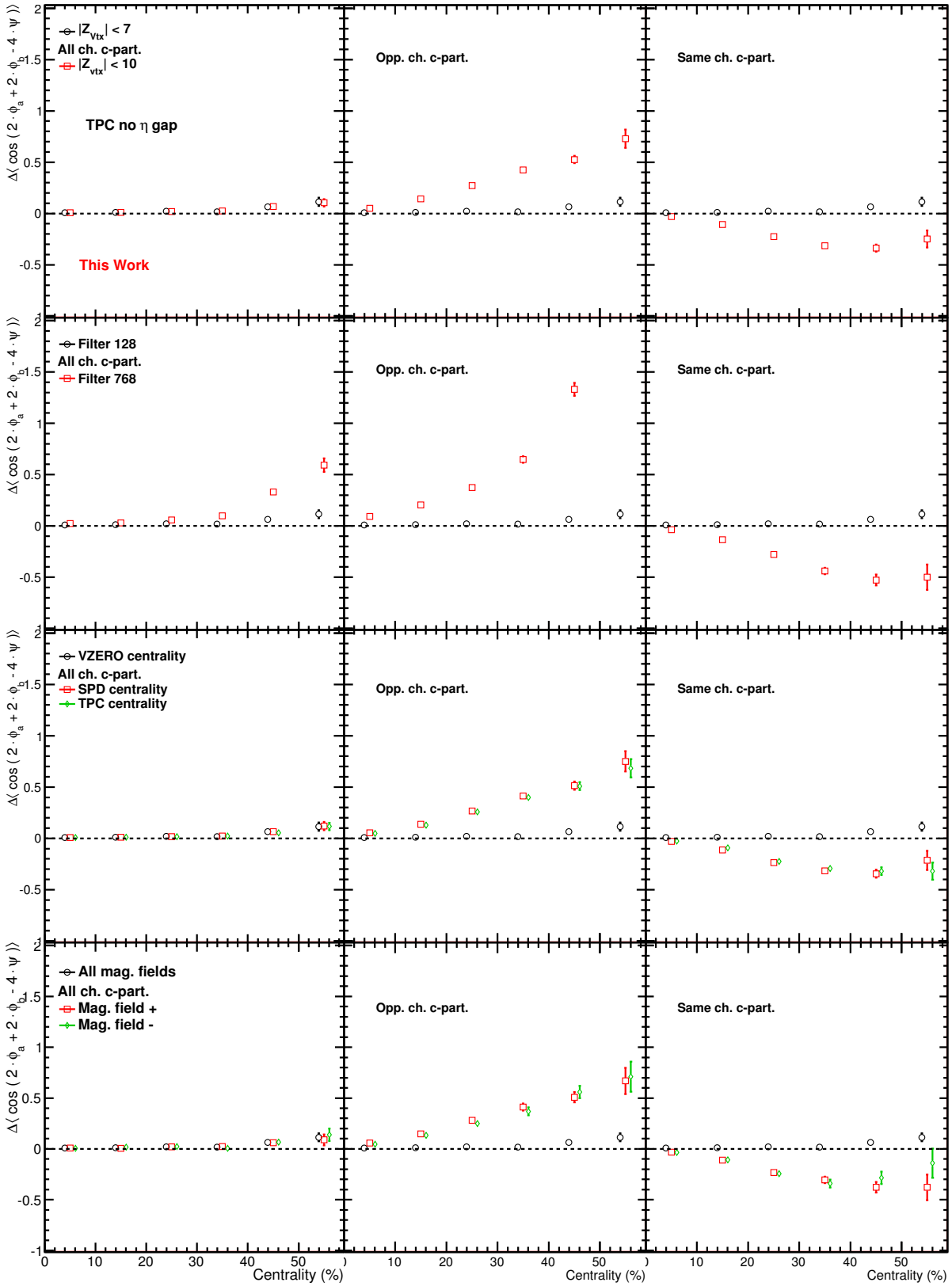

Figure 6.6: Charge-dependence of the Fourth harmonic correlator calculated using Q-cumulants without pseudorapidity gaps for multiple event and particle cuts. Left panel is without restriction on the *c*-particle, central panel with same-charge *c*-particle and right panel with opposite-charge *c*-particle.

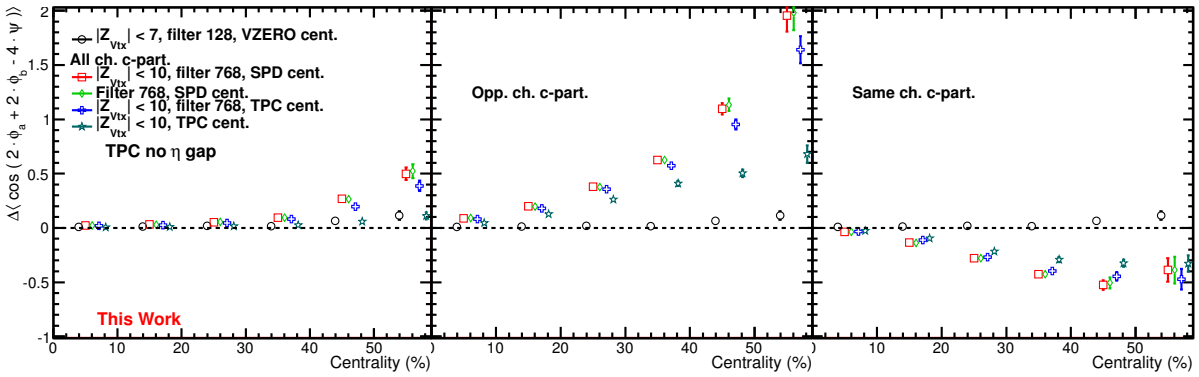

Figure 6.7: Charge-dependence of the Fourth harmonic correlator calculated using Q-cumulants without pseudorapidity gaps for multiple event and particle cuts used simultaneously in different combinations. Left panel is without restriction on the c-particle, central panel with same-charge c-particle and right panel with opposite-charge c-particle.

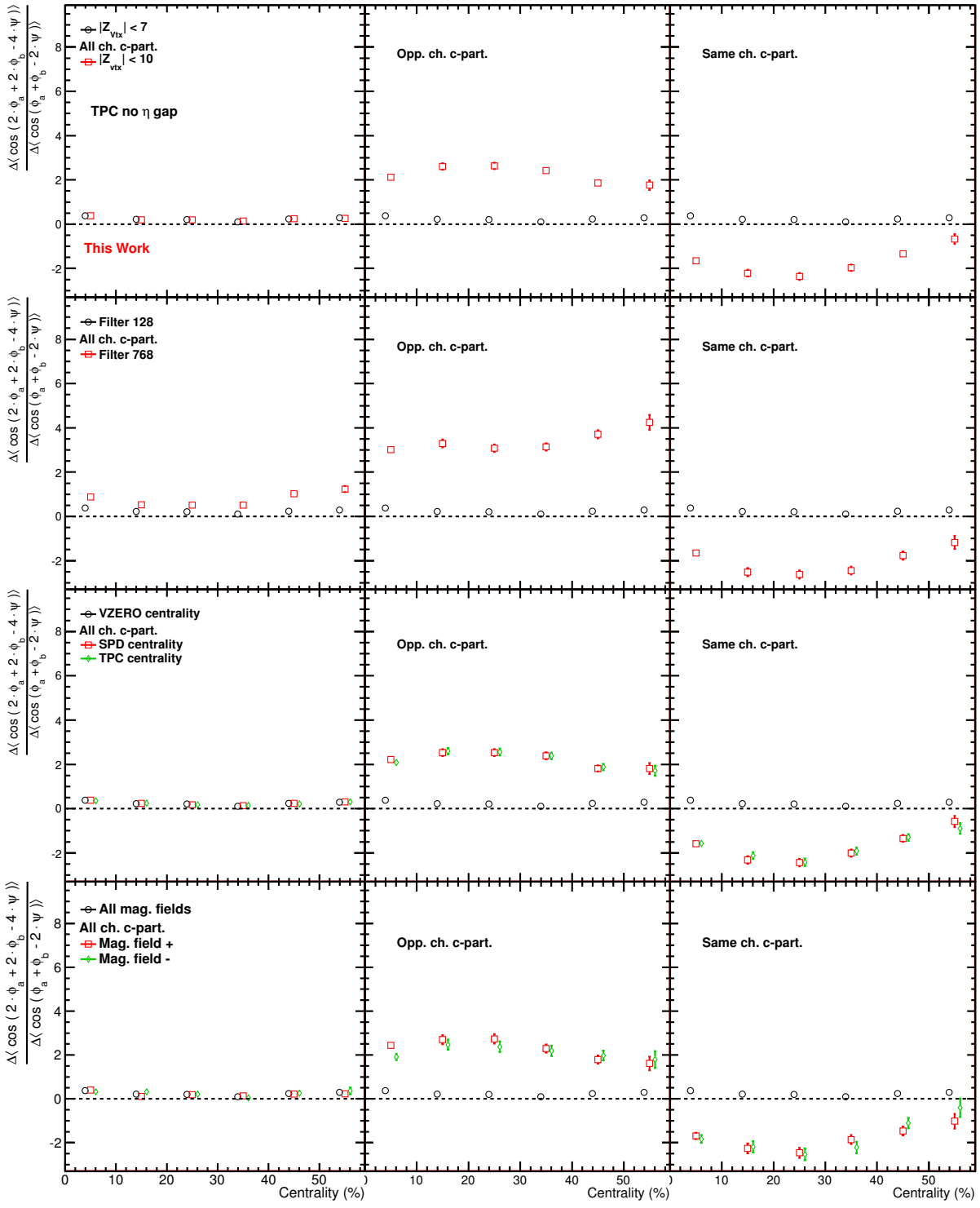

Figure 6.8: Ratio of the charge-dependence of the fourth and second harmonic correlators calculated using Q-cumulants without pseudorapidity gaps for multiple event and particle cuts. Left panel is without restriction on the c-particle, central panel with same-charge c-particle and right panel with opposite-charge c-particle.

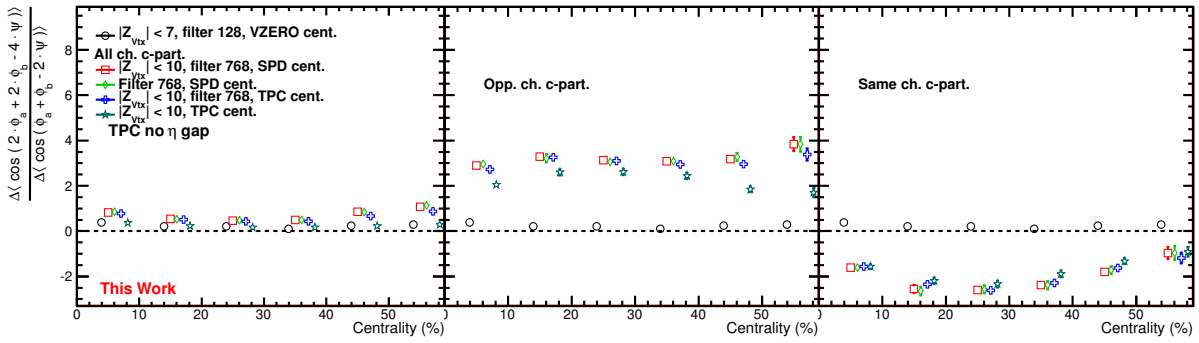

Figure 6.9: Ratio of the charge-dependence of the fourth and second harmonic correlators calculated using Q-cumulants without pseudorapidity gaps for multiple event and particle cut variations used simultaneously in different combinations. Left panel is without restriction on the c-particle, central panel with same-charge c-particle and right panel with opposite-charge c-particle.

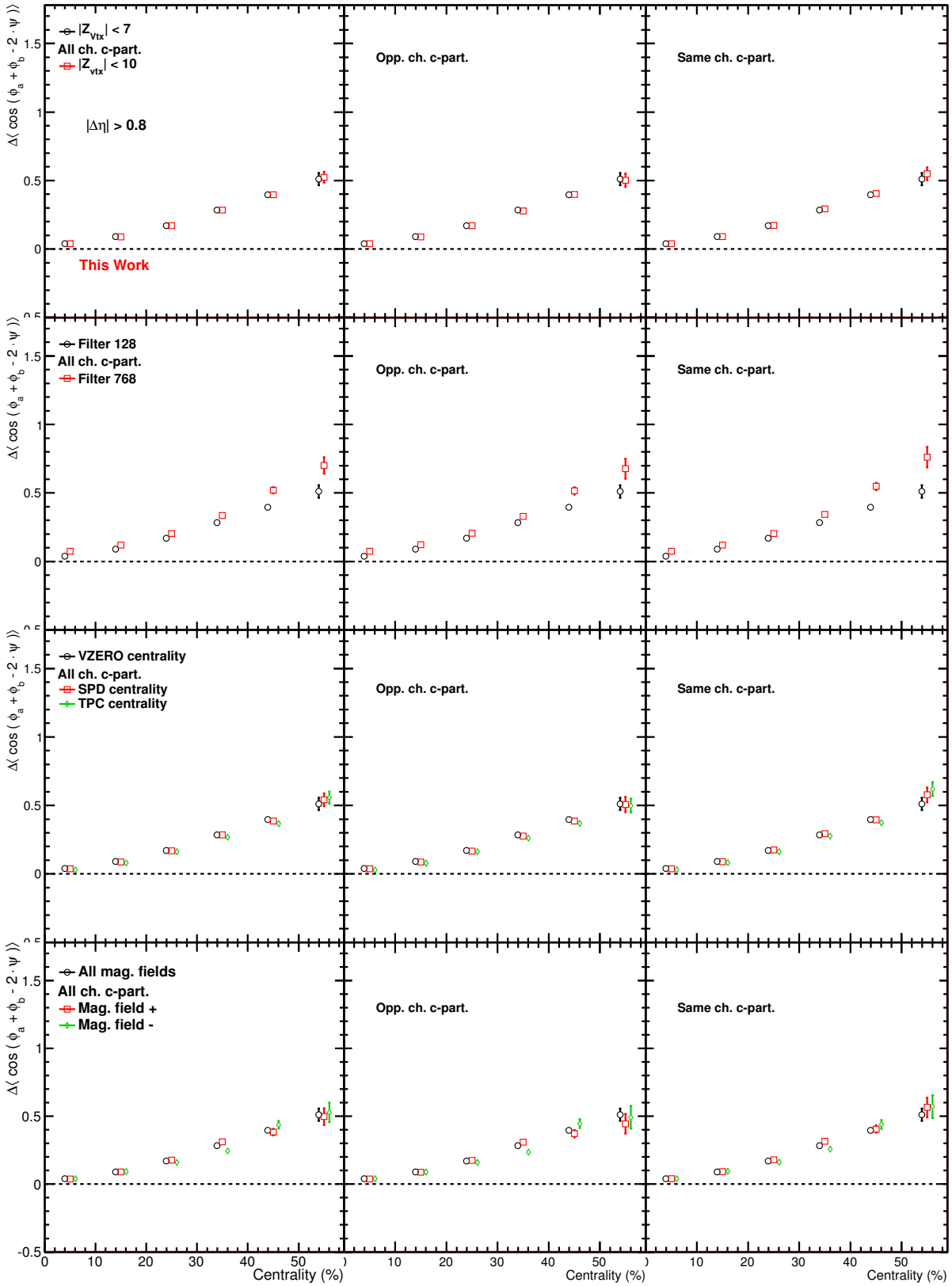

Figure 6.10: Charge-dependence of the second harmonic correlator calculated using Q-cumulants with pseudorapidity gaps for multiple event and particle cuts. Left panel is without restriction on the c-particle, central panel with same-charge c-particle and right panel with opposite-charge c-particle.

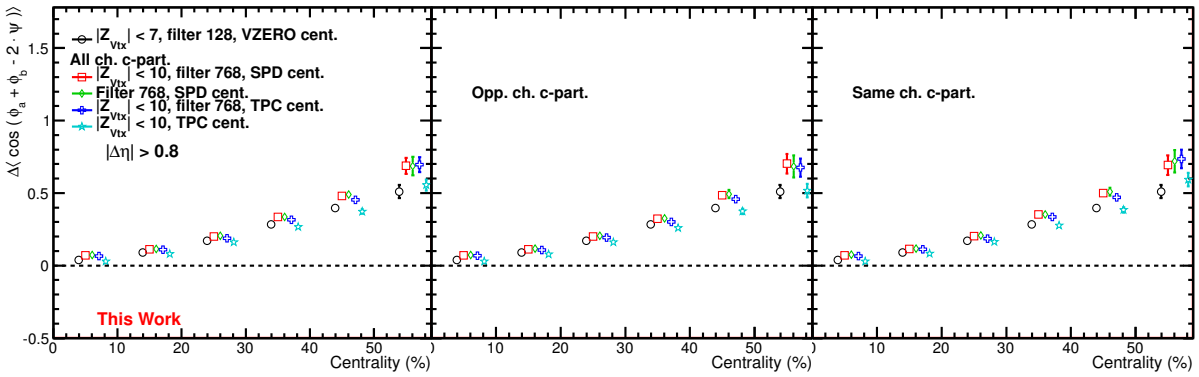

Figure 6.11: Charge-dependence of the second harmonic correlator with pseudorapidity gap for multiple event and particle cut variations used simultaneously in different combinations. Left panel is without restriction on the c-particle, central panel with same-charge c-particle and right panel with opposite-charge c-particle.

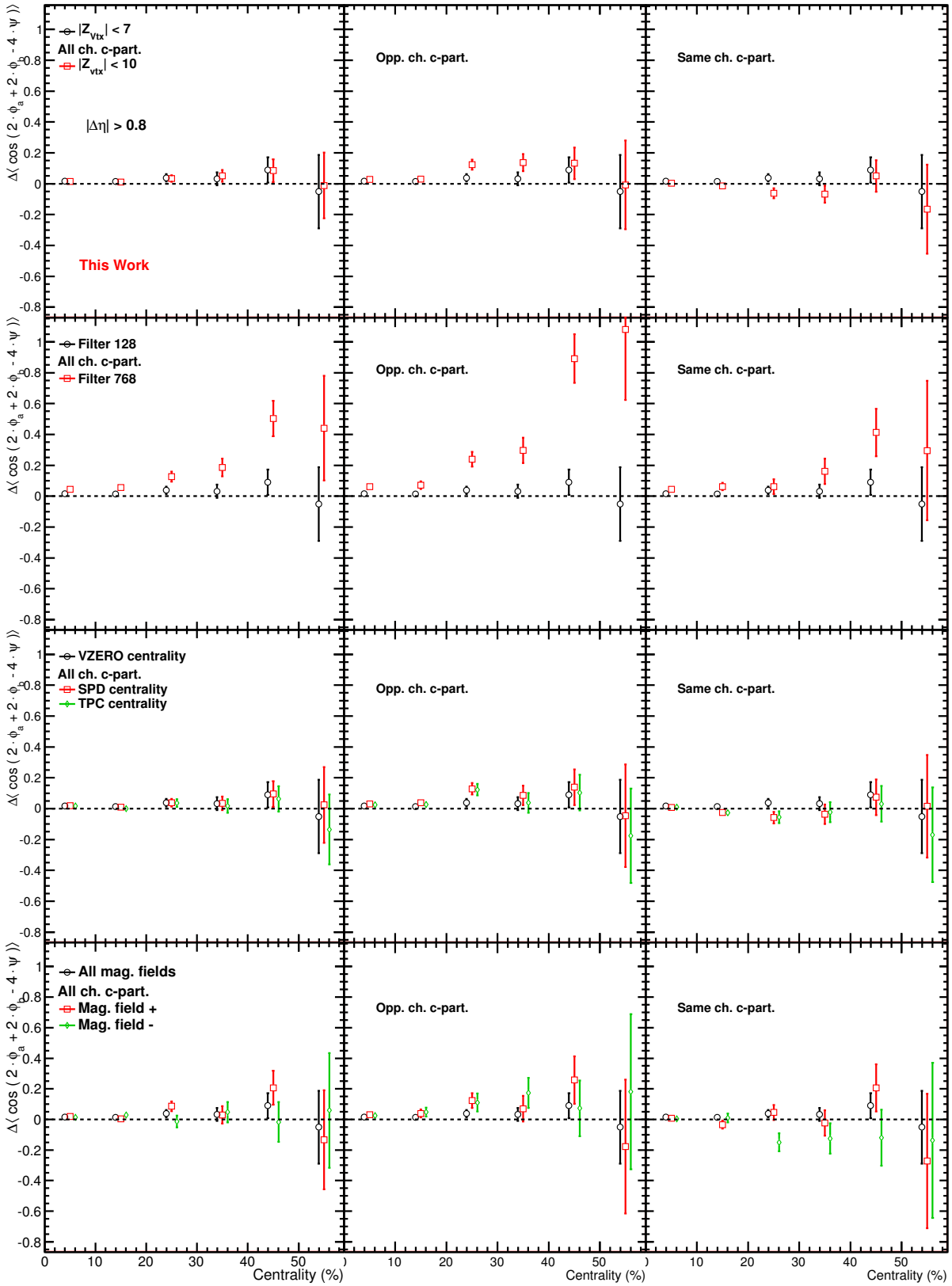

Figure 6.12: Charge-dependence of the fourth harmonic correlator calculated using Q-cumulants with pseudorapidity gaps for multiple event and particle cuts. Left panel is without restriction on the c-particle, central panel with same-charge c-particle and right panel with opposite-charge c-particle.

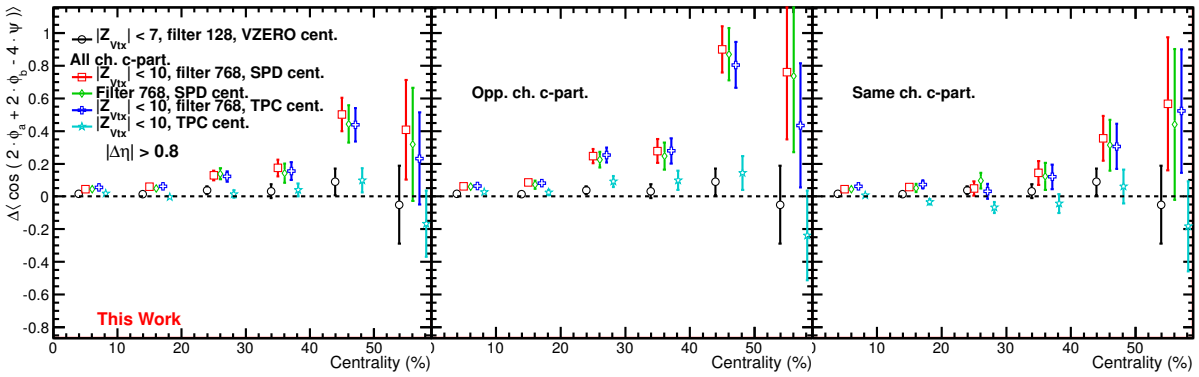

Figure 6.13: Charge-dependence of the fourth harmonic correlator with pseudorapidity gap for multiple event and particle cut variations used simultaneously in different combinations. Left panel is without restriction on the c-particle, central panel with same-charge c-particle and right panel with opposite-charge c-particle.

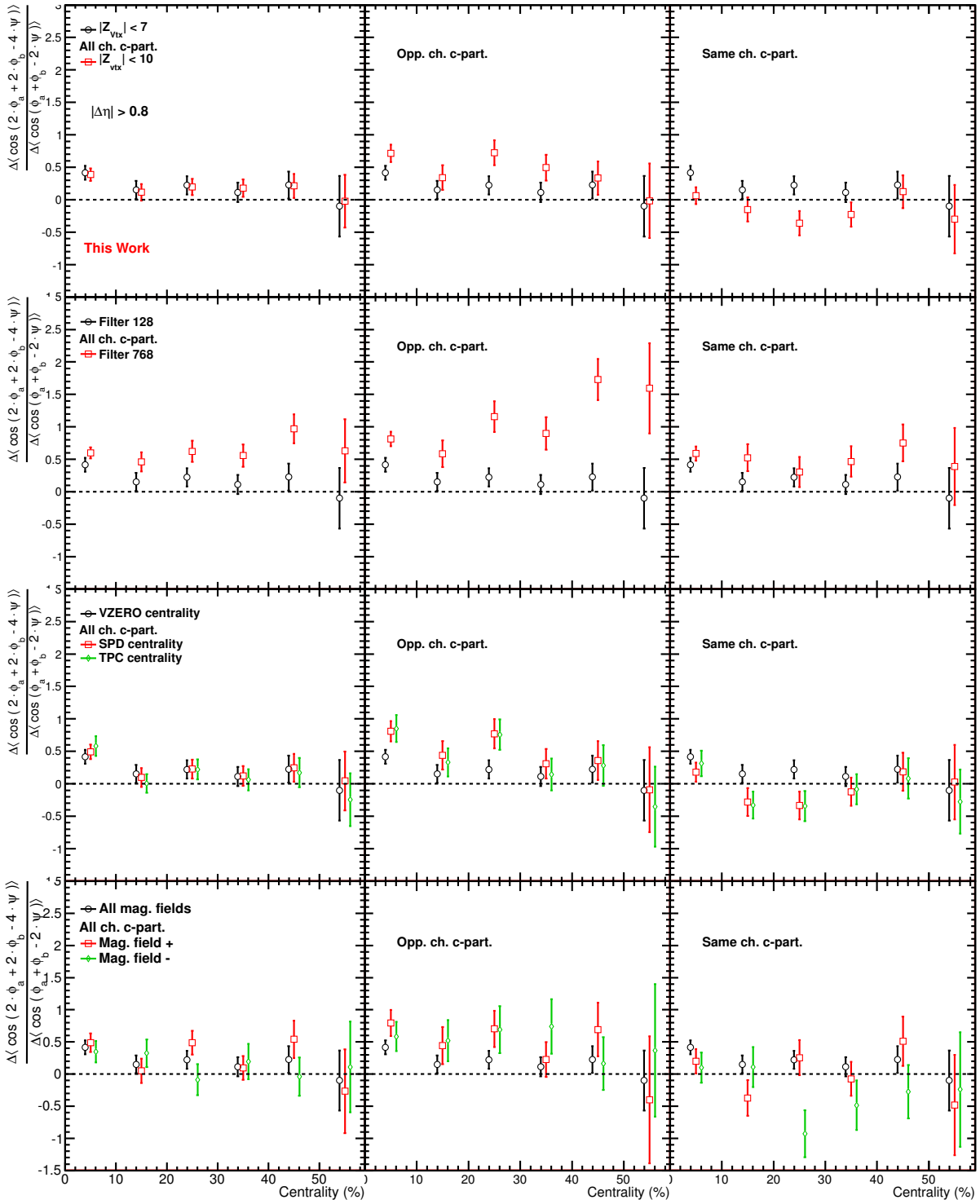

Figure 6.14: Ratio of the charge-dependence of the fourth and second harmonic correlators calculated using Q-cumulants with pseudorapidity gaps for multiple event and particle cuts. Left panel is without restriction on the *c*-particle, central panel with same-charge *c*-particle and right panel with opposite-charge *c*-particle.

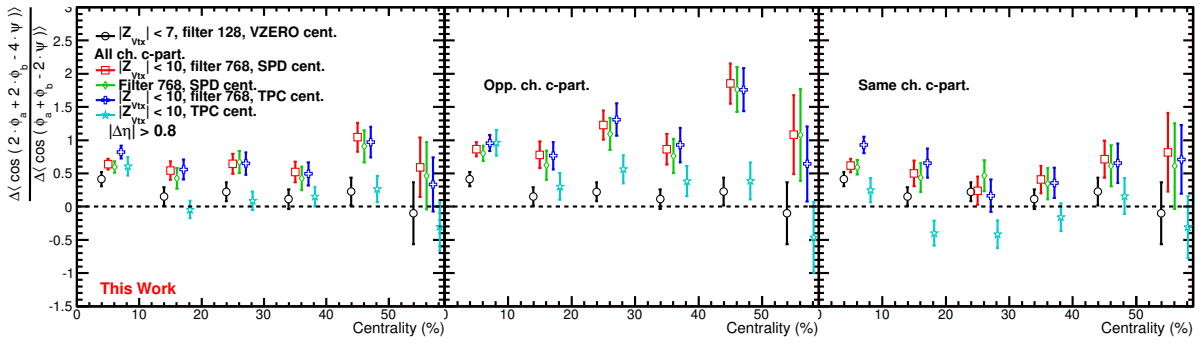

Figure 6.15: Ratio of the charge-dependence of the fourth and second harmonic correlators calculated using Q-cumulants with pseudorapidity gaps for multiple event and particle cut variations used simultaneously in different combinations. Left panel is without restriction on the c-particle, central panel with same-charge c-particle and right panel with opposite-charge c-particle.

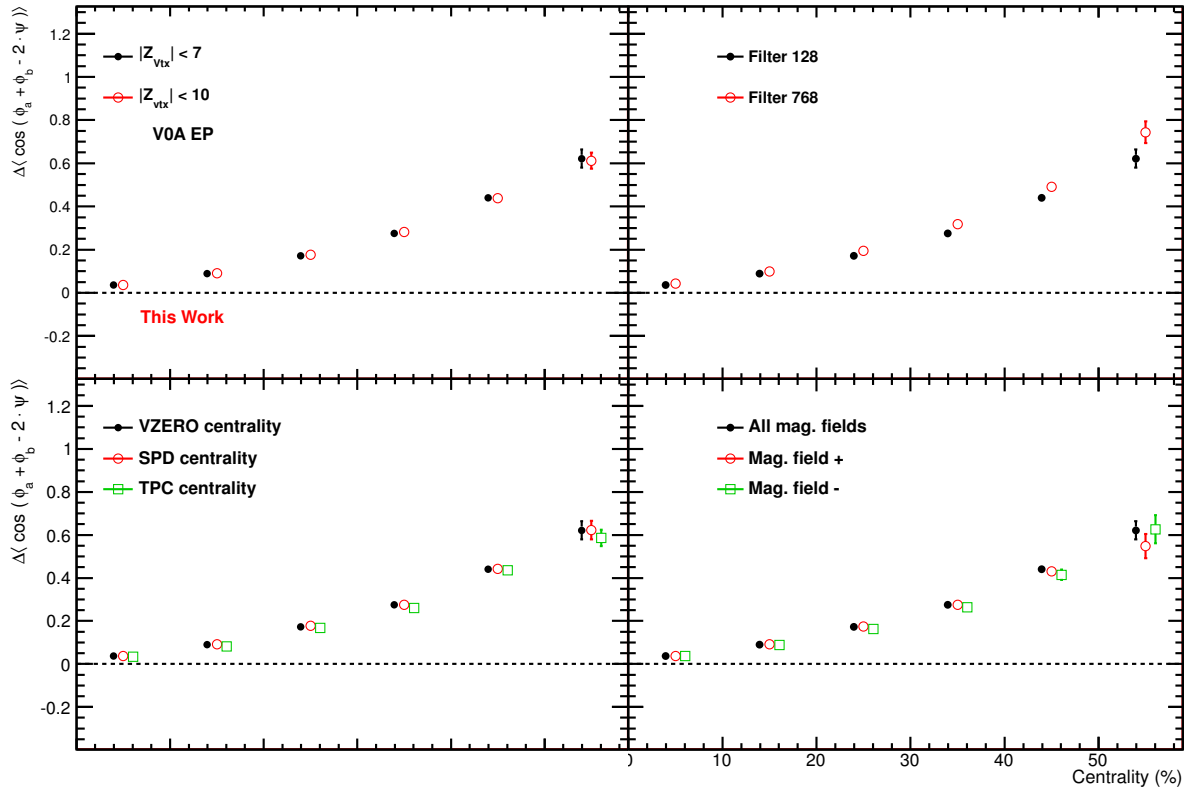

Figure 6.16: Charge-dependence of the second harmonic correlator calculated using VZEROA event planes for multiple event and particle cuts.

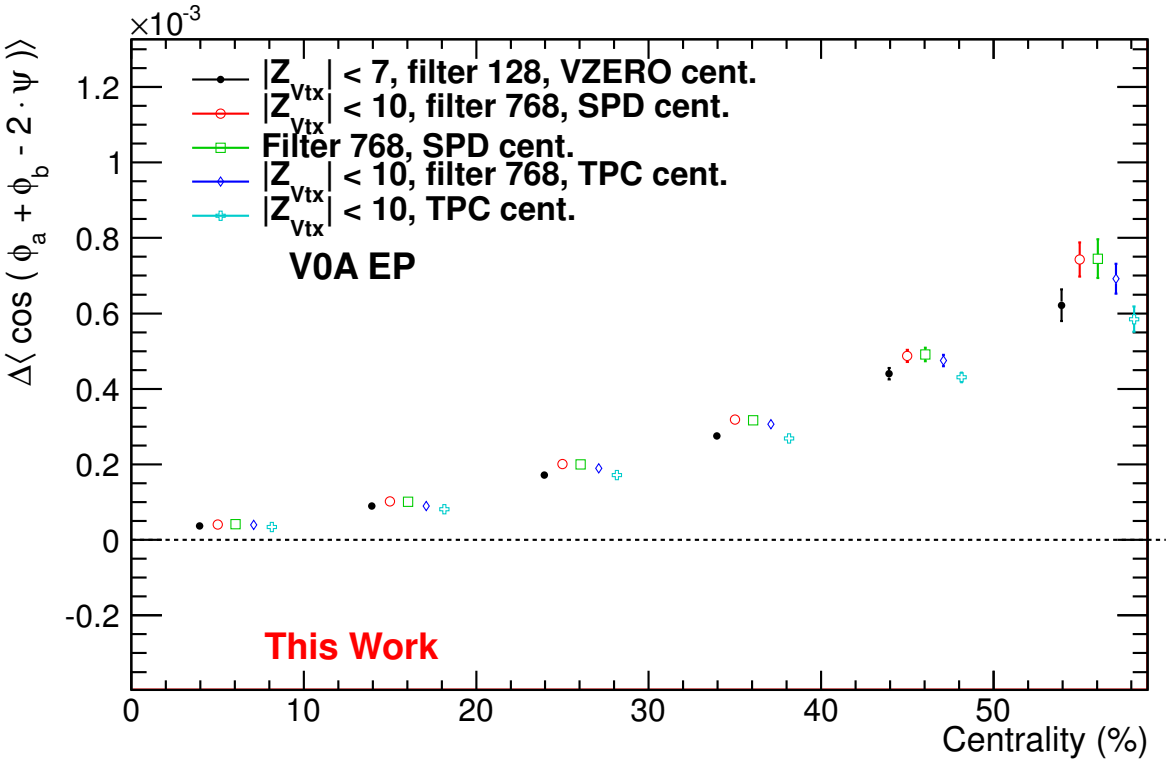

Figure 6.17: Charge-dependence of the second harmonic correlator calculated using VZEROA event planes for multiple event and particle cut variations used simultaneously in different combinations.

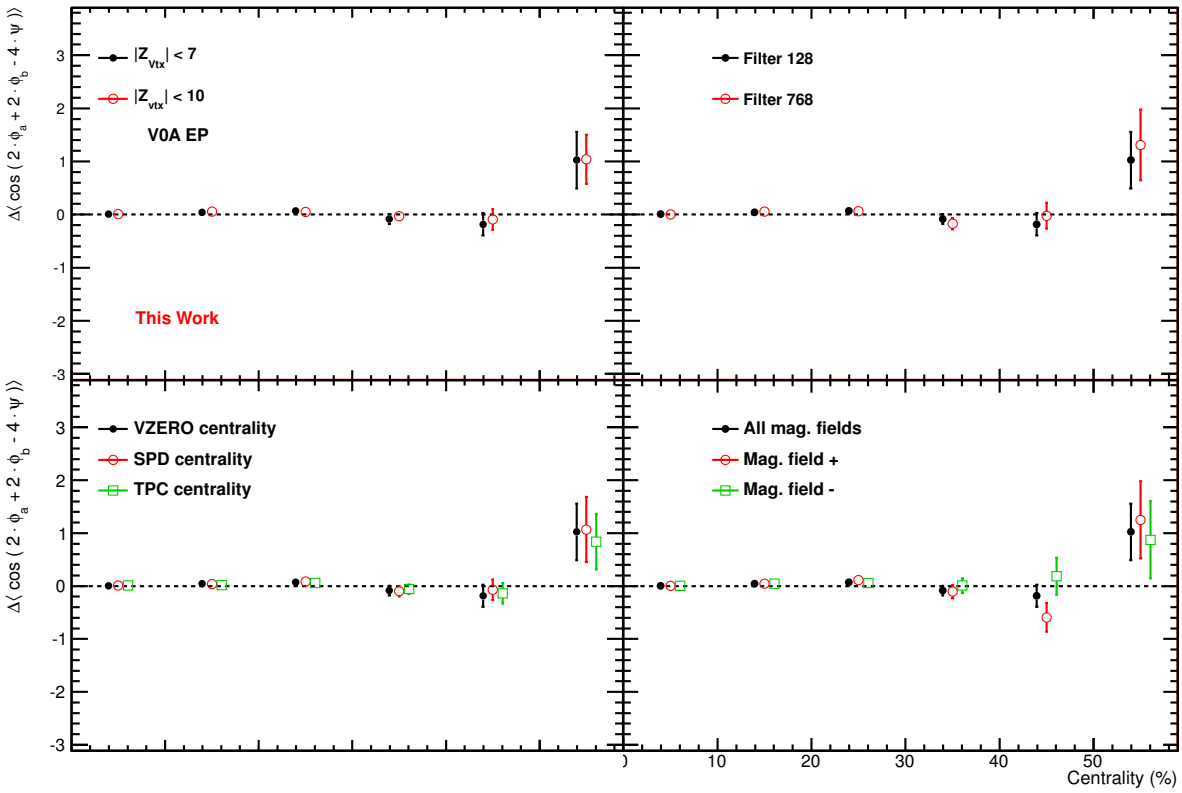

Figure 6.18: Charge-dependence of the fourth harmonic correlator calculated using VZEROA event planes for multiple event and particle cuts.

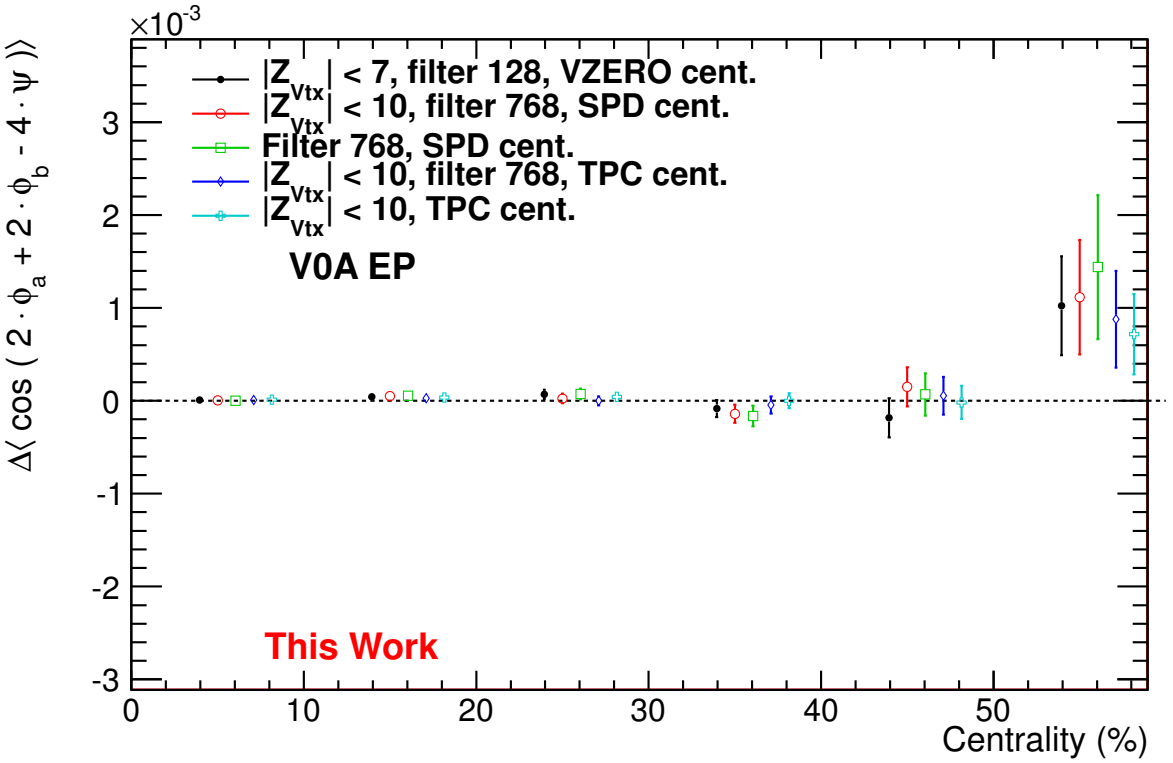

Figure 6.19: Charge-dependence of the fourth harmonic correlator calculated using VZEROA event planes for multiple event and particle cut variations used simultaneously in different combinations.

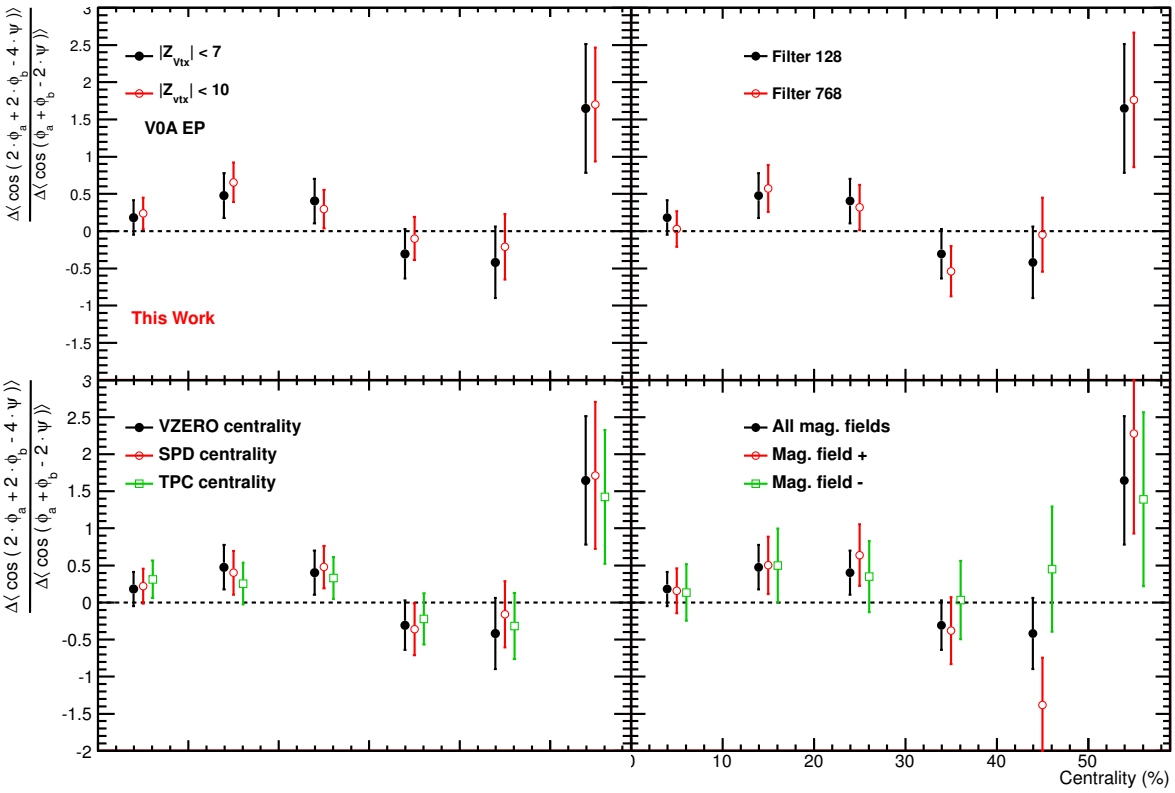

Figure 6.20: Ratio of the charge-dependence of the fourth and second harmonic correlators calculated using using VZEROA event planes for multiple event and particle cuts.

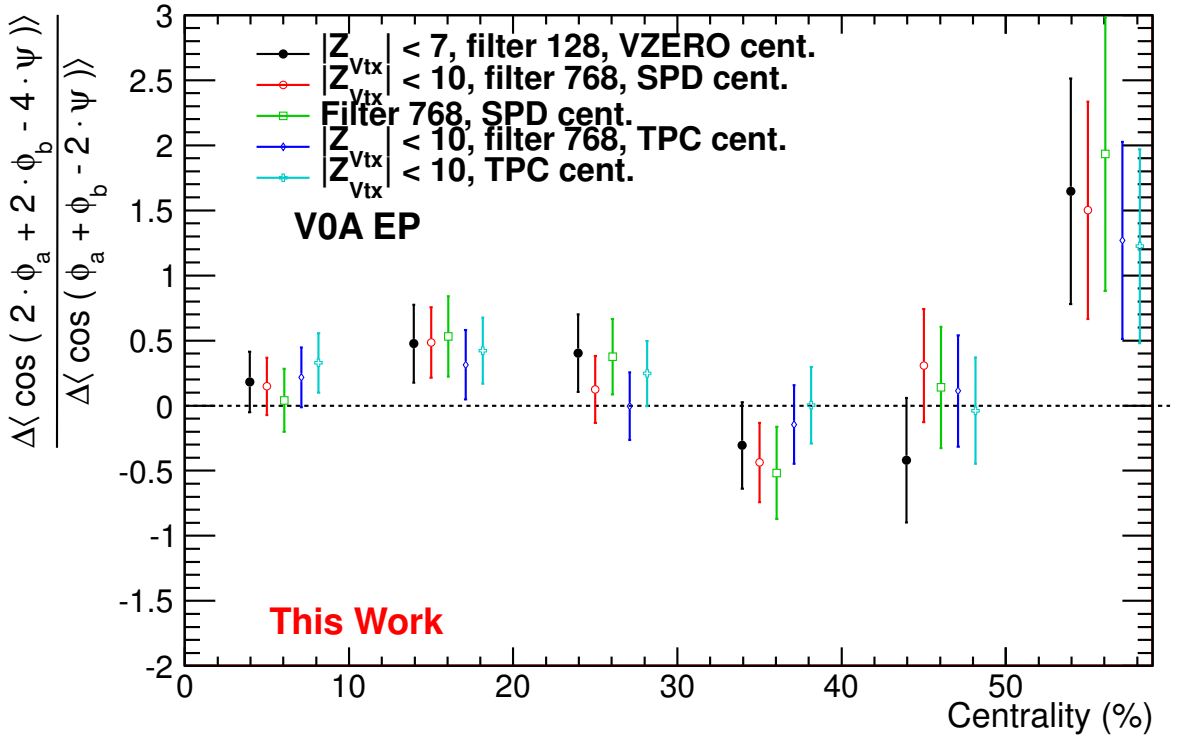

Figure 6.21: Ratio of the charge-dependence of the fourth and second harmonic correlators calculated using using VZEROA event planes for multiple event and particle cut variations used simultaneously in different combinations.

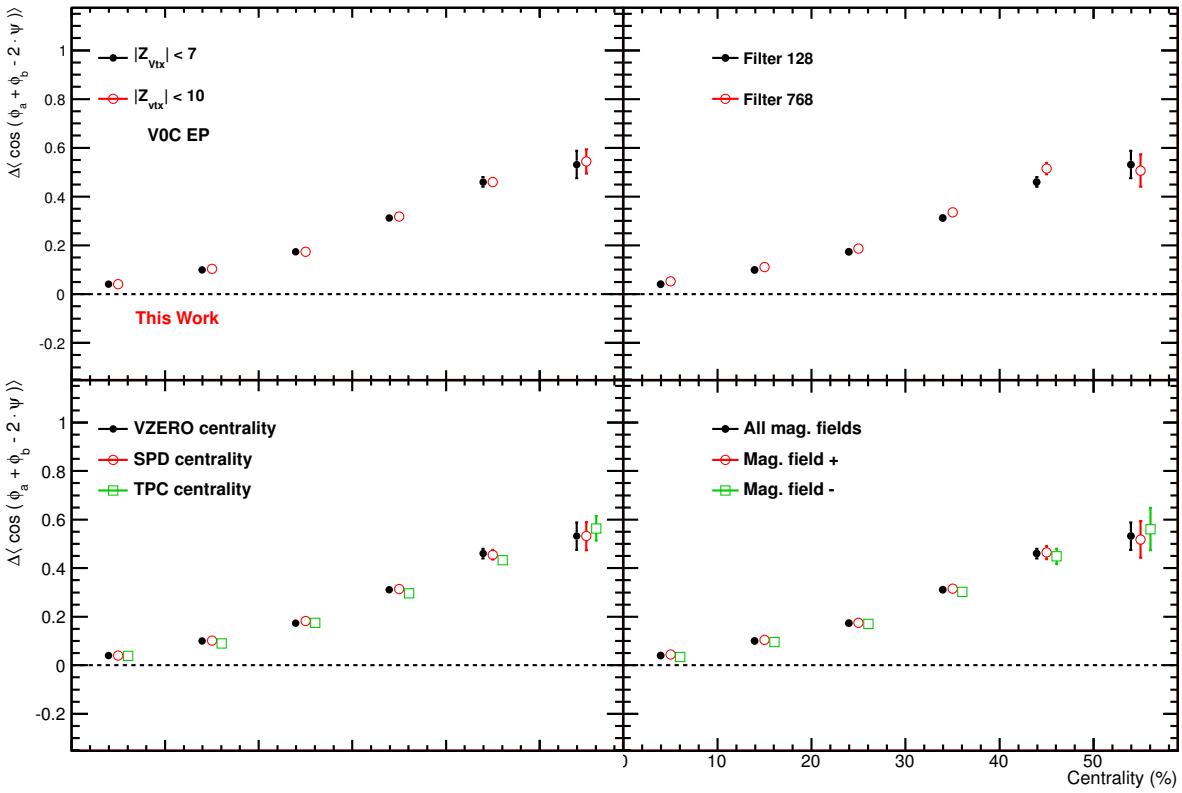

Figure 6.22: Charge-dependence of the second harmonic correlator calculated using VZEROC event planes for multiple event and particle cuts.

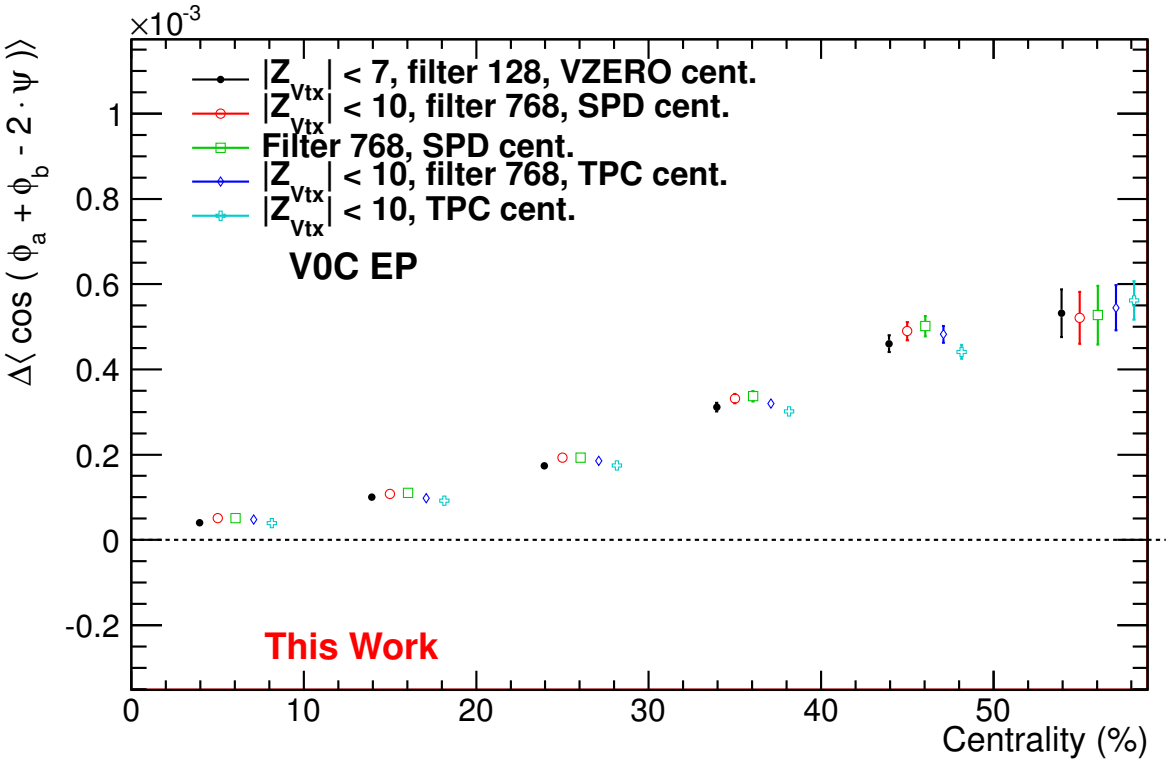

Figure 6.23: Charge-dependence of the second harmonic correlator calculated using VZERO event planes for multiple event and particle cut variations used simultaneously in different combinations.

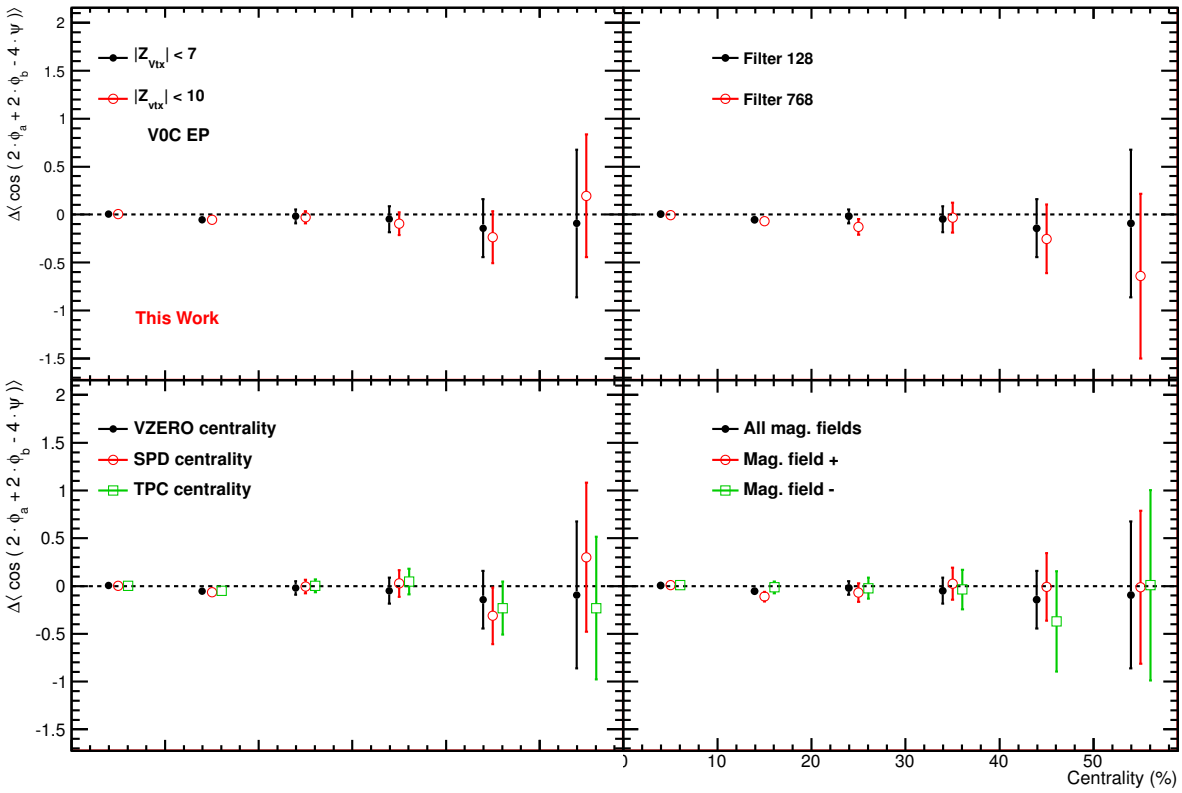

Figure 6.24: Charge-dependence of the fourth harmonic correlator calculated using VZEROC event planes for multiple event and particle cuts.

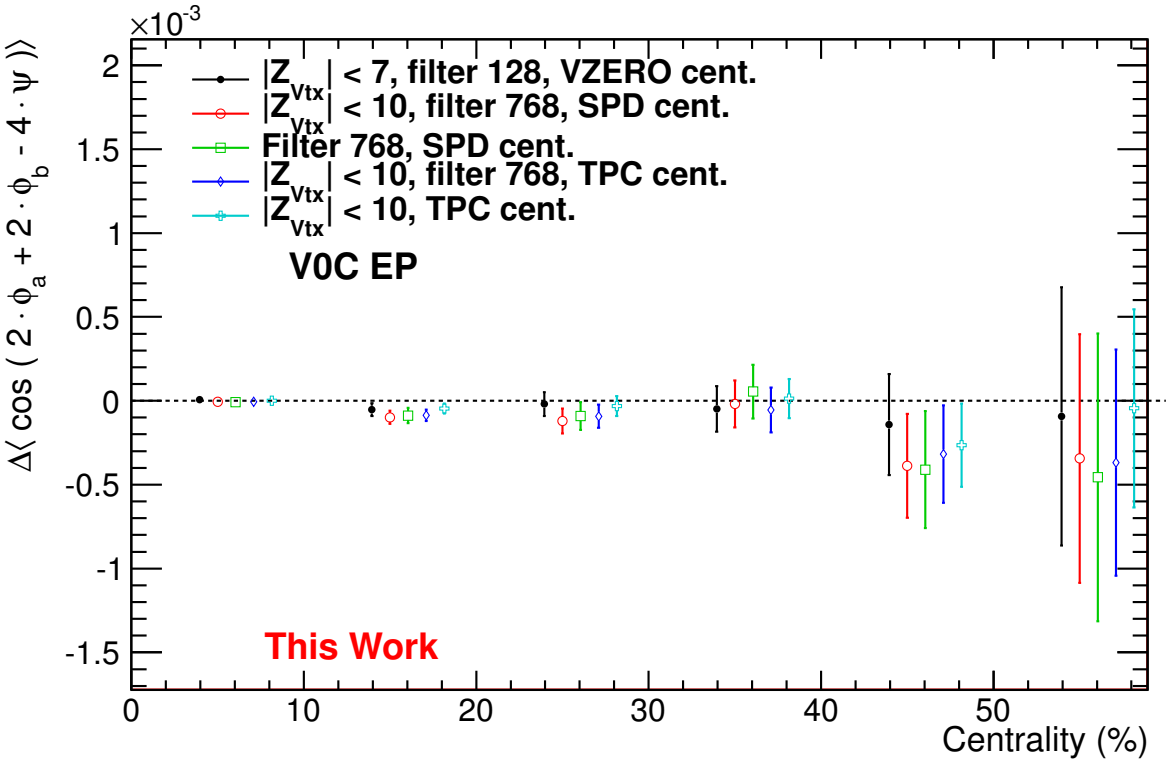

Figure 6.25: Charge-dependence of the fourth harmonic correlator calculated using VZEROC event planes for multiple event and particle cut variations used simultaneously in different combinations.

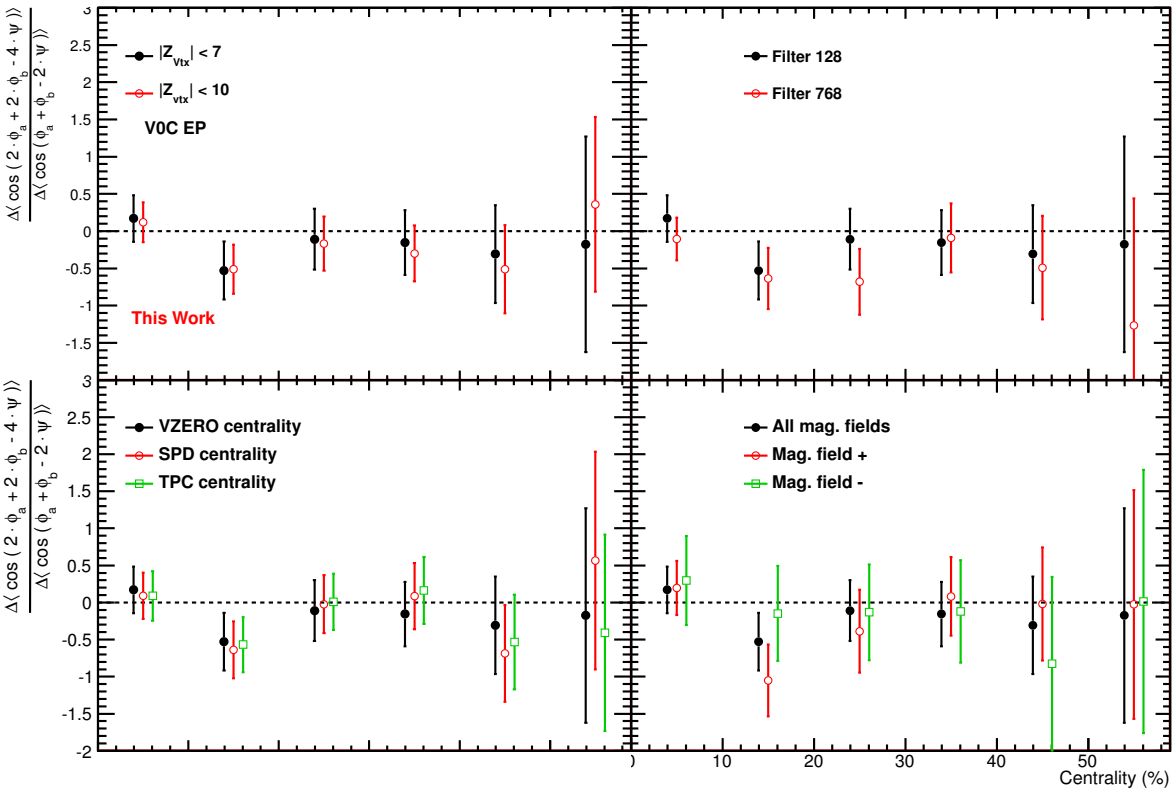

Figure 6.26: Ratio of the charge-dependence of the fourth and second harmonic correlators calculated using using VZEROC event planes for multiple event and particle cuts.

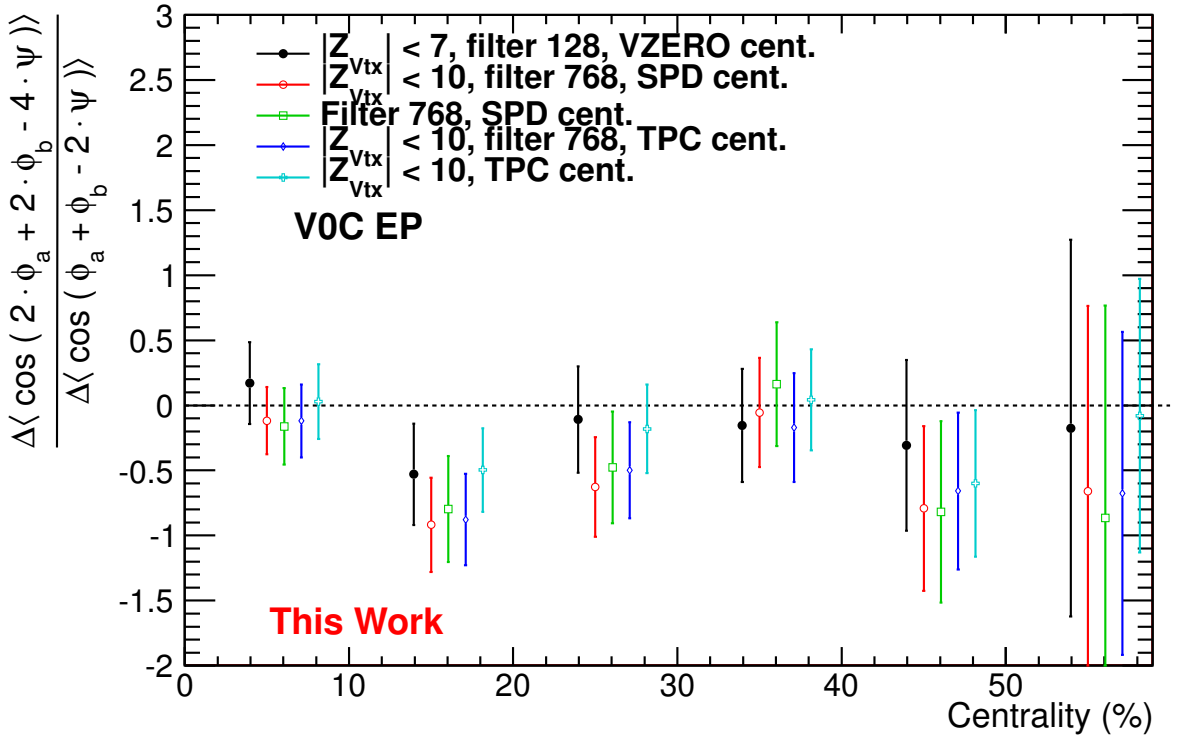

Figure 6.27: Ratio of the charge-dependence of the fourth and second harmonic correlators calculated using using VZEROC event planes for multiple event and particle cut variations used simultaneously in different combinations.

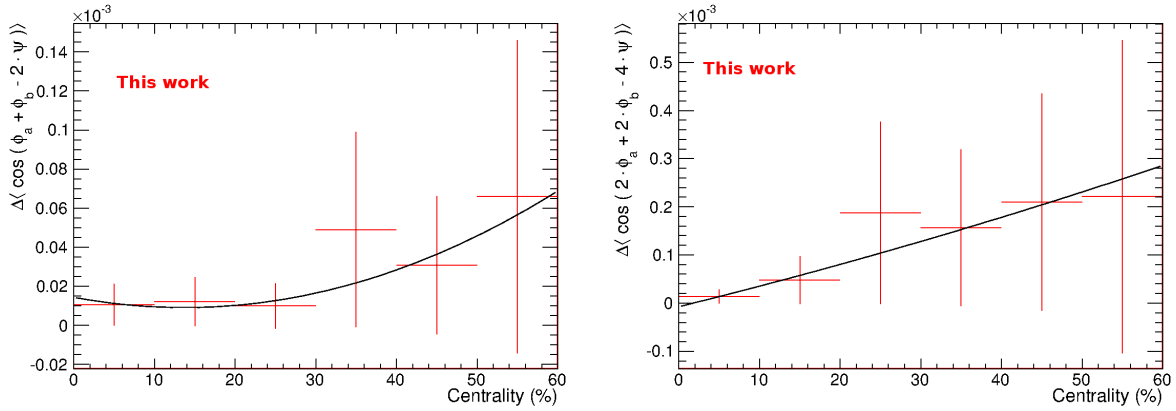

Figure 6.28: Fit of the estimated systematic errors for the second harmonic (left panel) and fourth harmonic (right panel) correlators calculated using Q-cumulants with pseudorapidity gaps

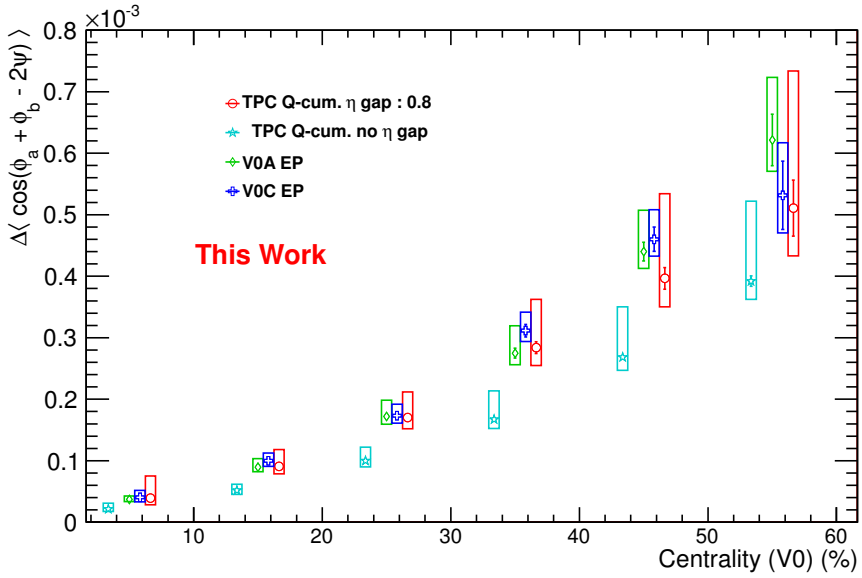

Figure 6.29: Charge-dependence of the second harmonic correlator ($\langle\cos(\phi+\phi-2\psi)\rangle_{\text{opp.}} - \langle\cos(\phi+\phi-2\psi)\rangle_{\text{same}}$) calculated with the VZERO event plane method and TPC Q-Cumulant methods (with and without pseudorapidity gaps), with systematic errors

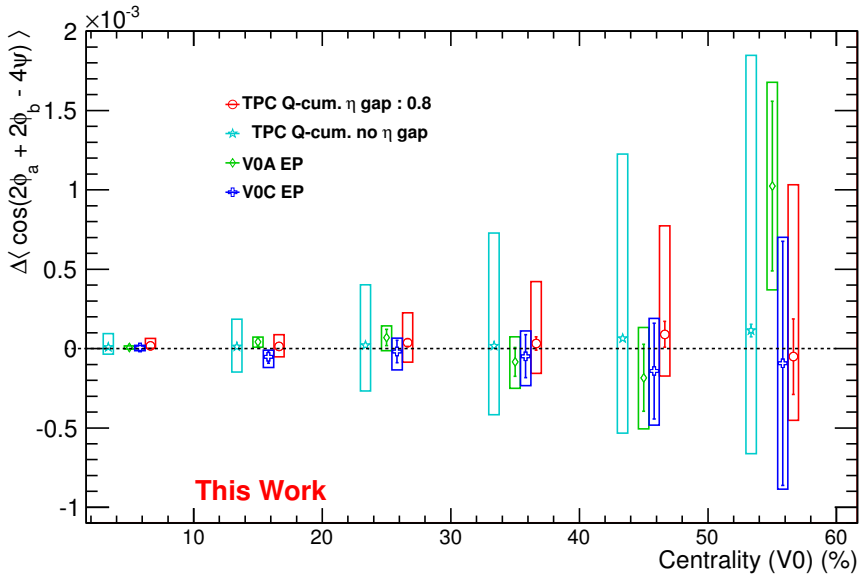

Figure 6.30: Charge-dependence of the fourth harmonic correlator ($\langle\cos(2\phi+2\phi-4\psi)\rangle_{\text{opp.}} - \langle\cos(2\phi+2\phi-4\psi)\rangle_{\text{same}}$) calculated with the VZERO event plane method and TPC Q-Cumulant methods (with and without pseudorapidity gaps), with systematic errors

Chapter 7

Comparison with Blast Wave Model Calculations

7.1 Introduction to the Blast Wave Model

In this section, we will try and compare the results obtained in the previous chapters with predictions derived from phenomenological models. To this end, we will use variants of the so-called "blast wave model" of particle distributions. It is based on a parametrization of the momentum and coordinate configurations at the kinetic freeze-out at constant proper time obtained in hydrodynamic models. Unlike the latters, the parameters are not directly derived from the equation of state but empirically determined from fit quantities (spectrum, flow) obtained from data. The blast wave equation is derived from the Cooper-Frye particle distribution at kinetic freeze-out:

$$E\frac{dN}{d^3p} = \int_\sigma f\left(\mathbf{x},\mathbf{p}\right) p^\mu d\sigma_\mu, \tag{7.1}$$

where σ is the freeze-out hypersurface, $d\sigma^\mu$ is an hypersurface element, p^μ is the momentum of particles within that element. $f\left(\mathbf{x},\mathbf{p}\right)$ is the phase space distribution, which we approximate as a boosted Boltzmann distribution $f\left(\mathbf{x},\mathbf{p}\right) = e^{-}u^\mu p_\mu/T_f$, and u_μ is a collective velocity perpendicular to the hypersurface that pushes the fluid elements outwards. Since we are mainly concerned with the azimuthal distribution of particles, we ignore the rapidity dependence in these equations, and the hypersurface will be described by an spherical

shell. We express the boost angle ϕ_b which is also, in this picture, the polar coordinate of an element of fluid. Using this coordinate, we introduce the transverse flow rapidity as $\rho_t = \left(\frac{r}{R}\right)^n (\rho_0 + \rho_2 \cos(2\phi_b) + \rho_4 \cos(4\phi_b))$. Similarly, we write the source azimuthal distribution as $\Omega = (1 + s_2 \cos(2\phi_b) + s_4 \cos(4\phi_b))$ [73]. One can recognize in this equation a harmonic expanson limited to even terms; this is how we introduce the anisotropy in the single-particle azimuthal distribution, both via an anisotropy in the "push" (ρ_t) and in the source of particles. The final blast wave equation we will used to parametrize the single-particle distribution is:

$$\frac{d^2N}{dp_t^2 d\phi} = \int_0^R r dr \int d\phi_b \Omega(\phi_b)\, e^{\alpha_t \cos(\phi_b - \phi)} K_1(\beta_t)\, m_t, \tag{7.2}$$

which we can rewrite as

$$\frac{dN}{p_t dp_t^2} = \int_0^R r dr \int d\phi_b \Omega(\phi_b)\, I_0(\alpha_t)\, K_1(\beta_t)\, m_t. \tag{7.3}$$

In these equations, $\alpha_t = \frac{p_t}{T}\sinh(\rho_t)$, $\beta_t = \frac{m_t}{T}\sinh(\rho_t)$, and $m_t = \sqrt{m^2 + p_t^2}$. We see that this equation relies on 7 parameters we will have to determine: the freeze-out temperature T, the maximum transverse radial push rapidity ρ_0, the anisotropy coefficient for the transverse push rapidity associated with the elliptic flow and quadratice flow ρ_2 and ρ_4, the corresponding source anisotropies s_2 and s_4 and the coefficient n introduced in the definition of ρ_t which describes the evolution of the transverse flow with respect to the radius. In section 7.2, we will see in details how to obtain the parameters that describe the heavy ion collisions analyzed in previous sections.

Our objective with blast wave model calculations is not to describe single-particle distributions but to calculate two-particle correlations and compare them with previous results. This is done by modifying the model and extrapolating the equations to a system of two particles. The assumption made is that both particles are created at the exact same coordinates. We will discuss in this section the required conditions for this approximation

and its consequences. Assuming the two particles are created at the same coordinates, we have [74]:

$$\begin{aligned}&\rho_2\left(\mathbf{p_{t,1}}, \mathbf{p_{t,2}}\right) = \\ &\int_0^R r dr \int d\phi_b \Omega\left(\phi_b\right) e^{\alpha_{t,1}\cos(\phi_b-\phi_1)} e^{\alpha_{t,2}\cos(\phi_b-\phi_2)} K_1\left(\beta_{t,1}\right) K_1\left(\beta_{t,2}\right) m_{t,1} m_{t,2}.\end{aligned} \tag{7.4}$$

We can interpret this equation in the following fashion: two particles are created close to one another, for instance, to a good approximation, 2 particles from the same binary nucleon-nucleon collision, and are subject to the same push from the collective motion in the medium. The final result emerges from the interplay of the initial correlation between the two particles and the contribution of the transverse flow, identical for both particles. In reality, not all pairs of particles in an event are created within the vicinity of each other. In fact, the majority of pairs are "unrelated", for instance because they originate from different binary collisions. This means we will need to introduce a correction to account for the proportion of pairs that do not have these short range correlations. This correction takes the form of a dilution factor D, defined as the ratio of pairs created at the same coordinates to the total number of pairs in the collision.

Using the Equations 7.3 and 7.4 for the 1- and 2-particle distributions, we can derive equations for related observables, such as flow coefficients and the mixed harmonic correlators. The differential flow coefficients are expressed as

$$\begin{aligned}v_n\left(p_T\right) &= \frac{\int_0^{2\pi} d\phi \int_0^R r dr \int d\phi_b \cos\left(\phi\right) \Omega\left(\phi_b\right) e^{\alpha_t \cos(\phi_b-\phi)} K_1\left(\beta_t\right) m_t}{\int_0^R r dr \int d\phi_b \Omega\left(\phi_b\right) I_0\left(\alpha_t\right) K_1\left(\beta_t\right) m_t} \\ &= \frac{\int_0^R r dr \int d\phi_b \Omega\left(\phi_b\right) I_n\left(\alpha_t\right) K_1\left(\beta_t\right) m_t}{\int_0^R r dr \int d\phi_b \Omega\left(\phi_b\right) I_0\left(\alpha_t\right) K_1\left(\beta_t\right) m_t},\end{aligned} \tag{7.5}$$

and the mixed harmonics are obtained from

$$\frac{1}{D}\langle\cos\left(n\left(\phi_a+\phi_b-2\psi\right)\right)\rangle = \frac{\int d\Gamma\cos\left(n\left(\phi_1+\phi_2\right)\right)\Omega\left(\phi_b\right)e^{\alpha_{t,1}\cos(\phi_b-\phi_1)}e^{\alpha_{t,2}\cos(\phi_b-\phi_2)}K_1\left(\beta_{t,1}\right)K_1\left(\beta_{t,2}\right)m_{t,1}m_{t,2}}{\int d\Gamma\Omega\left(\phi_b\right)e^{\alpha_{t,1}\cos(\phi_b-\phi_1)}e^{\alpha_{t,2}\cos(\phi_b-\phi_2)}K_1\left(\beta_{t,1}\right)K_1\left(\beta_{t,2}\right)m_{t,1}m_{t,2}}, \tag{7.6}$$

where $\int d\Gamma = \int_0^\infty dp_{t,1}\int_0^\infty dp_{t,2}\int_0^{2\pi}d\phi_1\int_0^{2\pi}d\phi_2\int_0^R rdr\int d\phi_b$.

We have previously defined the dilution factor as the ratio of the number of correlated pairs to the total number of pairs. We would usually have the average number of pairs produced in a single binary collision as the numerator, and the total number of pairs as the denominator. This can be approximated by

$$D = \frac{\langle n\left(n-1\right)\rangle}{\left(N_{\text{coll}}-1\right)\langle n\rangle^2+\langle n\left(n-1\right)\rangle}, \tag{7.7}$$

where n is the number of particles created in a nucleon-nucleon binary collision and N_{coll} is the number of those independent collisions. $N_{\text{coll}}\langle n\left(n-1\right)\rangle$ corresponds to the average number of correlated pairs and $N_{\text{coll}}\left(N_{\text{coll}}-1\right)\langle n\rangle^2$ the average number of uncorrelated pairs.

Our motivation for performing blast wave calculations is to estimate the value of the charge-dependence of the second order and fourth order mixed harmonic correlators $\langle\cos\left(\phi_+ + \phi_- - 2\psi\right)\rangle - 0.5\langle\cos\left(\phi_- + \phi_- - 2\psi\right)\rangle - 0.5\langle\cos\left(\phi_+ + \phi_+ - 2\psi\right)\rangle$ and $\langle\cos\left(2\phi_+ + 2\phi_- - 4\psi\right)\rangle - 0.5\langle\cos\left(2\phi_- + 2\phi_- - 4\psi\right)\rangle - 0.5\langle\cos\left(2\phi_+ + 2\phi_+ - 4\psi\right)\rangle$. An appropriate choice of dilution factor can reduce the calculation of these charge-dependence to a single calculation using Equation 7.6. Let us consider the charged particles created in a single nucleon-nucleon collision. We will assume that the only contribution to the charge-dependence of the mixed-harmonics correlators arises from local charge conservation (as we do not model the potential consequences of the CME). In this picture, the oppositely charged particles are created at freeze-out at the same coordinates and will be subjected to the same boost from the collective transverse expansion. If we consider all the particle pairs that can be chosen from this independent collision, oppositely charged pairs that were created to-

gether are on average more strongly correlated than other pairs. We distinguish three types of pairs in this collision:

1. Pairs that were created together, i.e. participate to local charge conservation. These are necessarily opposite-charge pairs

2. Opposite-charge pairs of particle that were created independently (but from the same nucleon-nucleon collision).

3. Same-charge pairs, which are always created independently.

The first two types of pairs both contribute to the opposite-charge mixed-harmonic correlators. If $2n$ charged particles are created in a binary collision, there are n pairs of the first type and $n\,(n-1)$ pairs of the second type. The third type of pairs, of which there are $n\,(n-1)$ as well, are the only contributions to the same-charge correlators. As a consequence, the charge-dependence $CD = \Delta\langle\cos\left(\phi_a + \phi_b - 2\psi\right)\rangle$ can be rewritten as:

$$\begin{aligned} CD &= \langle\cos\left(n\left(\phi_a + \phi_b - 2\psi\right)\right)\rangle_{\text{opp.}} - \langle\cos\left(n\left(\phi_a + \phi_b - 2\psi\right)\right)\rangle_{\text{same}} \\ &= \frac{1}{n^2}\sum_{\substack{a\in+,b\in-\\ \text{first type}}}\cos\left(n\left(\phi_a + \phi_b - 2\psi\right)\right)\rangle_{\text{opp.}} + \frac{1}{n^2}\sum_{\substack{a\in+,b\in-\\ \text{second type}}}\cos\left(n\left(\phi_a + \phi_b - 2\psi\right)\right)\rangle_{\text{opp.}} \\ &- \sum_{\substack{a\in+,b\in+\\ a\in-,b\in-}}\langle\cos\left(n\left(\phi_a + \phi_b - 2\psi\right)\right)\rangle_{\text{same}}. \end{aligned} \tag{7.8}$$

We use the indices "corr" and "uncorr" to qualify respectively the first types of pairs, and the second and third type of pairs. Equation 7.8 becomes:

$$\begin{aligned} CD &= \frac{1}{n}\langle\cos\left(n\left(\phi_a + \phi_b - 2\psi\right)\right)\rangle_{\text{corr}} + \frac{n\,(n-1)}{n^2}\langle\cos\left(n\left(\phi_a + \phi_b - 2\psi\right)\right)\rangle_{\text{uncorr}} \\ &- \langle\cos\left(n\left(\phi_a + \phi_b - 2\psi\right)\right)\rangle_{\text{uncorr}} \\ &= \frac{1}{n}\langle\cos\left(n\left(\phi_a + \phi_b - 2\psi\right)\right)\rangle_{\text{corr}} - \frac{1}{n^2}\langle\cos\left(n\left(\phi_a + \phi_b - 2\psi\right)\right)\rangle_{\text{uncorr}}. \end{aligned} \tag{7.9}$$

In Equation 7.9 we have made the assumption that the second and third types of pairs have identical contributions, on average, to their respective correlators, because any correlations

between them is presumed to be independent of their respective charges (unlike the first type of pairs); this contribution is $\langle\cos\left(n\left(\phi_a+\phi_b-2\psi\right)\right)\rangle_{\text{uncorr}}$. With values of $n > 5$ and assuming that $|\langle\cos\left(n\left(\phi_a+\phi_b-2\psi\right)\right)\rangle|_{\text{corr}} > |\langle\cos\left(n\left(\phi_a+\phi_b-2\psi\right)\right)\rangle|_{\text{uncorr}}$ (due to the stronger correlations arising from local charge conservation), we will neglect the second term of this equation so that the charge-dependence is now expressed as:

$$CD = \frac{1}{n}\langle\cos\left(n\left(\phi_a+\phi_b-2\psi\right)\right)\rangle_{\text{corr}}. \tag{7.10}$$

The correlation between the particles in the pairs that contribute to these averages is a spatial correlation as both particles were created at the same location and are subject to the same contribution from the anisotropic flow. We do not make any assumption as to the relative angle between these two particles and we neglect the effects from momentum conservation. This is exactly the condition corresponding to the two-particles distribution in Equation 7.6, and we can extrapolate our dilution factor to be $1/n$. We have defined n to be half the number of particles created in a single binary collision, or alternatively the number of pairs of the first type in that collision. However, we need to take into account the large number of pairs that are formed from particles originating from separate binary collisions in the dilution factor, as well as correlated pairs from every collision. To determine this quantity, we need to find the ratio of the number of pairs of particles created together to the total number of pairs. It is useful to extend the comments made on the number of pairs of each type to the entire event. In first approximation there are as many same-charge as opposite-charge uncorrelated pairs. When comparing the total number of opposite charge pairs to that of same charge pairs, the difference is made up from pairs affected by local charge conservation. This can be expressed by:

$$D = \frac{N_{+-} - N_{++} - N_{--}}{N_{+-} + N_{++} + N_{--}}. \tag{7.11}$$

This is the equation we will use to estimate the dilution factor in our blast wave calculations.

However, while it is necessary to use a dilution factor in the context of the calculation of a mixed-harmonic correlator, when calculating the ratio of the 4^{th} harmonic to the 2^{nd} harmonics, this quantity will appear both at the numerator and the denominator and thus cancel out. This eliminates the uncertainties that are otherwise associated to this factor and propagate to our final results.

7.2 Determination of the Parameters from Fits of v_2, v_4 and the Spectra of Charged Particles

The parameters used in the blast wave equation are chosen to best fit observables obtained from event-based data. In our parametrization, there are 7 such parameters, T, n, ρ_0, ρ_2, s_2, ρ_4, s_4, which can be classified in 3 categories: "isotropic"(T, n, ρ_0), elliptic flow-dependent (ρ_2, s_2), and quadrangular flow-dependent (ρ_4, s_4). In order to determine these parameters, we perform fits of transverse momentum spectra and differential elliptic flow $v_2\left(p_T\right)$ obtained from identified pions, kaons and protons to obtain the first five of these parameters, followed by a fit of $v_4\left(p_T\right)$ of unidentified charged particles to obtain the latter two. To reduce the uncertainty on the radial and elliptic flow-dependent parameters, we will perform the fit simultaneously on six histograms, corresponding to the spectra and differential elliptic flow of (negatively-charged) kaons, antiprotons and pions. This simultaneous fit uses the TMinuit minimization algorithm provided by the ROOT data analysis toolkit. We minimize a quantity, χ^2, that we calculate based on each bin of each histogram using the following equation:

$$\chi^2 = \sum_{\text{histograms}} \sum_{i \in \text{bins}} \left(\frac{g_{\text{BW}} - h\left(i\right)}{\sigma_{h(i)}} \right)^2 . \tag{7.12}$$

In Equation 7.12, $h\left(i\right)$ is the value of the i^{th} bin of one of the histograms, and g_{BW} is a blast wave-based "guess" function of p_T(for the spectrum or elliptic flow depending on the nature of h) obtained by using a set of parameters chosen by TMinuit. The parameters are varied by

the algorithm in order to obtain the minimum (or minima) of χ^2. Once the global minimum has been found, we have the set of parameters that describe the data the most appropriately. Each g_{BW} in the sum from Equation 7.12 differ by the particle mass used in the blast wave integral (equation 7.3) and enter this expression via the transverse mass m_T. It is not possible to directly (and accurately) fit an observable obtained from unidentified particles using this equation. In particular, as we lack a set of satisfying differential quadratic flow results for identified particles, we need to find a method to obtain the 4^{th} order parameters from unidentified charged particle data. This is done by considering that kaons, protons and pions constitute almost the entirety of the charged particles detected by the tracking system and that $v_{4,\text{unid.}}(p_T)$ is an average of the contributions from these three particle types. In other words, we will fit a single histogram and the χ^2 will be obtained from

$$\chi^2 = \sum_{i \in \text{bins}} \left(\frac{\frac{\frac{dN_\pi}{dp_T} g_{\text{BW},\pi} + \frac{dN_K}{dp_T} g_{\text{BW},K} + \frac{dN_{\bar{p}}}{dp_T} g_{\text{BW},\bar{p}}}{\frac{dN_\pi}{dp_T} + \frac{dN_K}{dp_T} + \frac{dN_{\bar{p}}}{dp_T}} - h(i)}{\sigma_{h(i)}} \right)^2, \tag{7.13}$$

where $g_{\text{BW},\pi}$ is the blast wave spectrum assuming pion mass, etc. In this context, we use an average of all three spectra weighted by their abundance at each value of $p_T$used in the calculation of χ^2. While we still expect large uncertainties from this method, they will be reduced compared to a calculation that would assume pion mass and estimate the parameters from a simple fit of this blast wave function.

Figures 7.1 and 7.2 show the fits for the pions, kaons and protons spectra and elliptic flow, respectively. Likewise, Figure 7.3 shows the results of the unidentified particles $v_4(p_T)$ fits using a linear combination of the pion-, kaon- and proton-mass blast wave integral. The resulting parameters are shown in Tables 7.1 to 7.6 and Figures 7.4 and 7.5.

Table 7.1: Blast Wave integral parameters obtained from the fitting of identified particle spectra, v_2 and charged particle v_4, 0-5% centrality

T	s_2	ρ_0	ρ_a	γ	s_4	ρ_b
0.094751	0.023206	1.274177	0.022661	1.106246	0.016024	0.018766
σ_T	σ_{s_2}	σ_{ρ_0}	σ_{ρ_a}	σ_γ	σ_{s_4}	σ_{ρ_b}
0.003067	0.000853	0.019462	0.001326	0.045886	0.009242	0.004514

	T	s_2	ρ_0	ρ_a	γ	s_4	ρ_b
T	0.000009	-0.000000	-0.000027	0.000001	-0.000021	0.000000	0.000000
s_2	-0.000000	0.000001	0.000008	-0.000000	0.000014	0.000000	0.000000
ρ_0	-0.000027	0.000008	0.000379	0.000008	0.000734	0.000000	0.000000
ρ_a	0.000001	-0.000000	0.000008	0.000002	0.000025	0.000000	0.000000
γ	-0.000021	0.000014	0.000734	0.000025	0.002106	0.000000	0.000000
s_4	0.000000	0.000000	0.000000	0.000000	0.000000	0.000085	-0.000040
ρ_b	0.000000	0.000000	0.000000	0.000000	0.000000	-0.000040	0.000020

Table 7.2: Blast Wave integral parameters obtained from the fitting of identified particle spectra, v_2 and charged particle v_4, 5-10% centrality

T	s_2	ρ_0	ρ_a	γ	s_4	ρ_b
0.098163	0.037253	1.241177	0.042123	1.067754	0.010268	0.015968
σ_T	σ_{s_2}	σ_{ρ_0}	σ_{ρ_a}	σ_γ	σ_{s_4}	σ_{ρ_b}
0.002600	0.000825	0.014209	0.001725	0.041225	0.001595	0.001009

	T	s_2	ρ_0	ρ_a	γ	s_4	ρ_b
T	0.000007	0.000001	-0.000007	0.000003	0.000011	0.000000	0.000000
s_2	0.000001	0.000001	0.000007	0.000000	0.000014	0.000000	0.000000
ρ_0	-0.000007	0.000007	0.000202	0.000011	0.000461	0.000000	0.000000
ρ_a	0.000003	0.000000	0.000011	0.000003	0.000043	0.000000	0.000000
γ	0.000011	0.000014	0.000461	0.000043	0.001700	0.000000	0.000000
s_4	0.000000	0.000000	0.000000	0.000000	0.000000	0.000003	-0.000002
ρ_b	0.000000	0.000000	0.000000	0.000000	0.000000	-0.000002	0.000001

Table 7.3: Blast Wave integral parameters obtained from the fitting of identified particle spectra, v_2 and charged particle v_4, 10-20% centrality

T	s_2	ρ_0	ρ_a	γ	s_4	ρ_b
0.102234	0.056070	1.211599	0.062219	1.078263	0.019090	0.011813
σ_T	σ_{s_2}	σ_{ρ_0}	σ_{ρ_a}	σ_γ	σ_{s_4}	σ_{ρ_b}
0.002426	0.000991	0.011962	0.002386	0.041592	0.001495	0.000929

	T	s_2	ρ_0	ρ_a	γ	s_4	ρ_b
T	0.000006	0.000001	0.000002	0.000004	0.000030	0.000000	0.000000
s_2	0.000001	0.000001	0.000008	0.000001	0.000020	0.000000	0.000000
ρ_0	0.000002	0.000008	0.000143	0.000017	0.000397	0.000000	0.000000
ρ_a	0.000004	0.000001	0.000017	0.000006	0.000070	0.000000	0.000000
γ	0.000030	0.000020	0.000397	0.000070	0.001730	0.000000	0.000000
s_4	0.000000	0.000000	0.000000	0.000000	0.000000	0.000002	-0.000001
ρ_b	0.000000	0.000000	0.000000	0.000000	0.000000	-0.000001	0.000001

Table 7.4: Blast Wave integral parameters obtained from the fitting of identified particle spectra, v_2 and charged particle v_4, 20-30% centrality

T	s_2	ρ_0	ρ_a	γ	s_4	ρ_b
0.107940	0.076585	1.176757	0.084202	1.129609	0.033239	0.004375
σ_T	σ_{s_2}	σ_{ρ_0}	σ_{ρ_a}	σ_γ	σ_{s_4}	σ_{ρ_b}
0.003486	0.002040	0.019107	0.005730	0.080217	0.002415	0.001465

	T	s_2	ρ_0	ρ_a	γ	s_4	ρ_b
T	0.000012	0.000006	0.000047	0.000018	0.000218	0.000000	0.000000
s_2	0.000006	0.000004	0.000035	0.000010	0.000138	0.000000	0.000000
ρ_0	0.000047	0.000035	0.000365	0.000097	0.001435	0.000000	0.000000
ρ_a	0.000018	0.000010	0.000097	0.000033	0.000424	0.000000	0.000000
γ	0.000218	0.000138	0.001435	0.000424	0.006438	0.000000	0.000000
s_4	0.000000	0.000000	0.000000	0.000000	0.000000	0.000006	-0.000003
ρ_b	0.000000	0.000000	0.000000	0.000000	0.000000	-0.000003	0.000002

Table 7.5: Blast Wave integral parameters obtained from the fitting of identified particle spectra, v_2 and charged particle v_4, 30-40% centrality

T	s_2	ρ_0	ρ_a	γ	s_4	ρ_b
0.110708	0.093759	1.140160	0.095938	1.184522	0.043160	0.000812
σ_T	σ_{s_2}	σ_{ρ_0}	σ_{ρ_a}	σ_γ	σ_{s_4}	σ_{ρ_b}
0.002362	0.001723	0.013673	0.003536	0.054693	0.004007	0.002312

	T	s_2	ρ_0	ρ_a	γ	s_4	ρ_b
T	0.000006	0.000002	0.000003	0.000006	0.000040	0.000000	0.000000
s_2	0.000002	0.000003	0.000016	0.000004	0.000061	0.000000	0.000000
ρ_0	0.000003	0.000016	0.000187	0.000028	0.000635	0.000000	0.000000
ρ_a	0.000006	0.000004	0.000028	0.000013	0.000135	0.000000	0.000000
γ	0.000040	0.000061	0.000635	0.000135	0.002992	0.000000	0.000000
s_4	0.000000	0.000000	0.000000	0.000000	0.000000	0.000016	-0.000009
ρ_b	0.000000	0.000000	0.000000	0.000000	0.000000	-0.000009	0.000005

Table 7.6: Blast Wave integral parameters obtained from the fitting of identified particle spectra, v_2 and charged particle v_4, 40-50% centrality

T	s_2	ρ_0	ρ_a	γ	s_4	ρ_b
0.112333	0.105013	1.072642	0.095329	1.139262	0.066358	-0.009745
σ_T	σ_{s_2}	σ_{ρ_0}	σ_{ρ_a}	σ_γ	σ_{s_4}	σ_{ρ_b}
0.002281	0.002159	0.016111	0.003257	0.067329	0.007543	0.003983

	T	s_2	ρ_0	ρ_a	γ	s_4	ρ_b
T	0.000005	0.000002	-0.000002	0.000005	0.000030	0.000000	0.000000
s_2	0.000002	0.000005	0.000024	0.000004	0.000103	0.000000	0.000000
ρ_0	-0.000002	0.000024	0.000260	0.000025	0.000950	0.000000	0.000000
ρ_a	0.000005	0.000004	0.000025	0.000011	0.000134	0.000000	0.000000
γ	0.000030	0.000103	0.000950	0.000134	0.004535	0.000000	0.000000
s_4	0.000000	0.000000	0.000000	0.000000	0.000000	0.000057	-0.000029
ρ_b	0.000000	0.000000	0.000000	0.000000	0.000000	-0.000029	0.000016

7.3 Integration of the Blast Wave Equation and Comparison with Reference v_2 and v_4

A possible test of the accuracy of our blast wave fits and calculation is to verify that we can reconstruct the reference v_2 and v_4 and compare them to the ones associated with the published differential $v_2(p_T)$ and $v_4(p_T)$ (Figures 7.6 and 7.7). Similarly, we can verify that the blast wave results for other common hydrodynamic variables, such as the mean collective motion tranverse rapidity ρ_t^2 (Figure 7.8), have reasonable values. The reference elliptic flow we obtain from the blast wave integral is very close to the publish v_2; the discrepancy is much larger in the case of quadratic flow ($\sim 10\%$). This is not unexpected, as these errors arise from fitting unidentified particles v_4 with mass-specific blast wave integrals. Using a linear combination of several particle-specific blast wave functions reduced this discrepancy but did not eliminate it entirely.

Figure 7.9 shows the dilution factor calculated by applying Equation 7.11 to TPC track pairs. Using this dilution factor, we estimate the charge-dependence of the second- and fourth-harmonic correlators, shown in Figures 7.10 and 7.11

7.4 Systematical Errors

Several sources of systematic error have been identified in our blast wave calculations. The most easily identifiable sources of systematic errors arise from the propagation of errors on the parameters, but as we have noted in a previous section, there is a significant discrepancy between the reference v_4 reconstructed from our blast wave model and the published quadratic flow. In order to take into account this discrepancy, we refit a modified set of$v_4(p_T)$, each scaled by the corresponding centrality bin of the ratio $\frac{v_{4,\mathrm{BWref}}}{v_{4,\mathrm{ref}}}$ (Figure 7.12). The newly obtained parameters are shown in Figure 7.13 Another source of systematic uncertainties comes from the choice of fitting range. We estimate the contribution to the

systematic error by performing the same spectra, v_2 and v_4 fits while increasing the fitting range by 0.5 GeV towards the high-p_T end. The results are plotted in Figures 7.14 and 7.15 The contribution of the uncertainty on the parameters is estimated by recalculating the blast wave observables, second and fourth harmonic, as well as their ratio, while varying the fitted parameters up and down by a value equal to their standard deviation (i.e. $\pm\sigma$). Several combinations of parameter variations are used, and Figures 7.16 and 7.17 are the resulting relative discrepancy. In each centrality bin, the lower and highest point are selected to form the lower and higher limits to systematic error contributions.

These three sources of systematic errors will be considered independent, corresponding to a "worst case scenario" approach, and added in quadrature to give the final systematic errors.

7.5 Results and Comparison with Data

Figures 7.18 and 7.19 show the comparison of the observed charge-dependence of the second and fourth harmonic correlators with their blast wave predictions. In the second harmonic case, the blast wave describes the observed results quite well, which contributes to validating the approach in this context and our choice of dilution factor. The fourth harmonic correlators from data and blast wave calculations are consistent with each other, but the uncertainties on both are rather large.

Similarly, the uncertainties on the ratio of the charge-dependence of the fourth harmonic to the charge-dependence of the second harmonic (Figures 7.20 and 7.21) make it difficult to conclude decisively one way or another. The blast wave results are consistent with the results obtained from Pb-Pb data, withing statistical errors, but further studies are required to control the systematic errors.

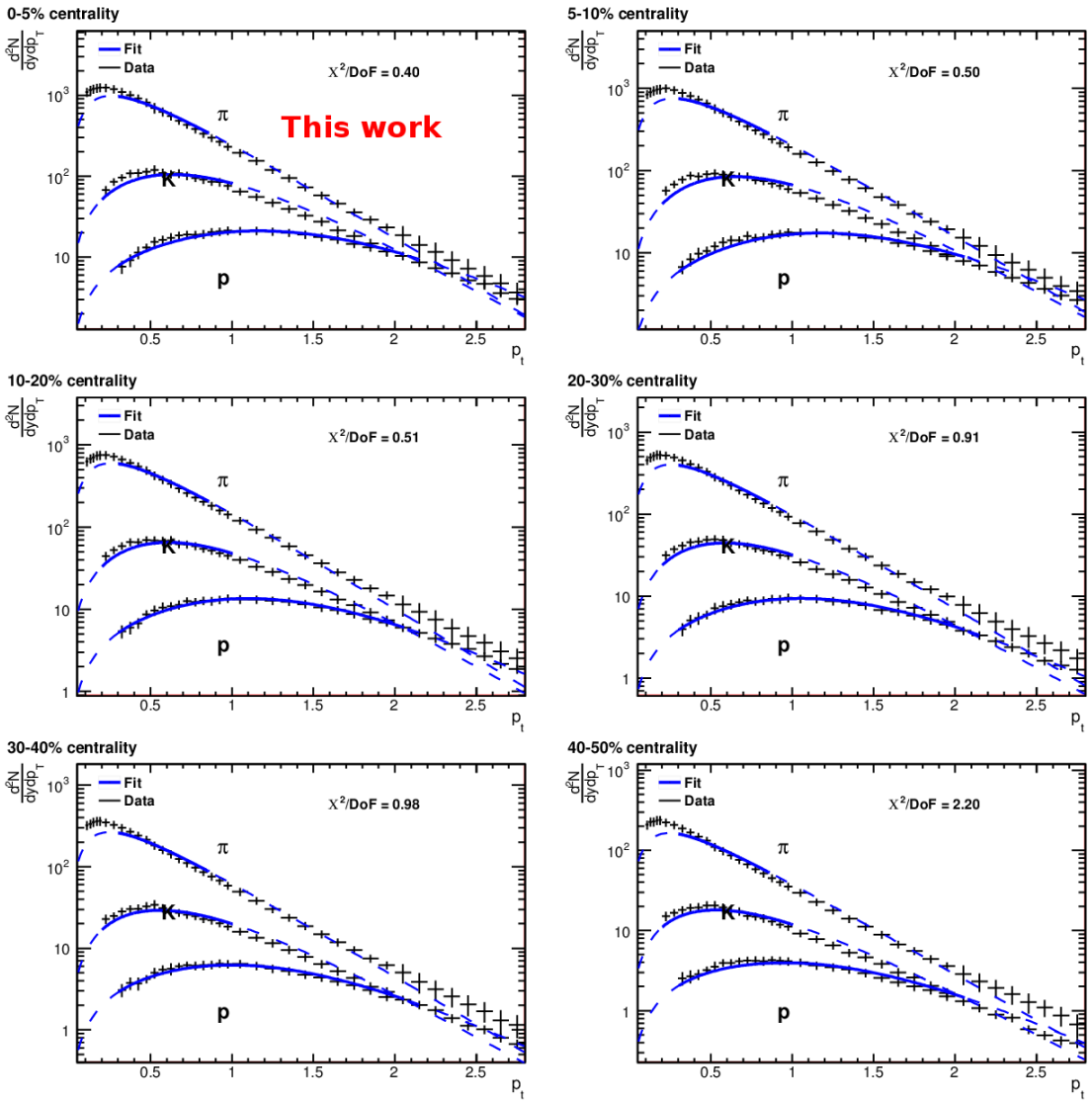

Figure 7.1: Fits of the kaons, protons and pions spectra from Pb–Pb at $\sqrt{s_{NN}} = 2.76$ TeV using a blast wave integral; dashed lines prolongate the fit function outside of the fitting domain. Black points from [29]

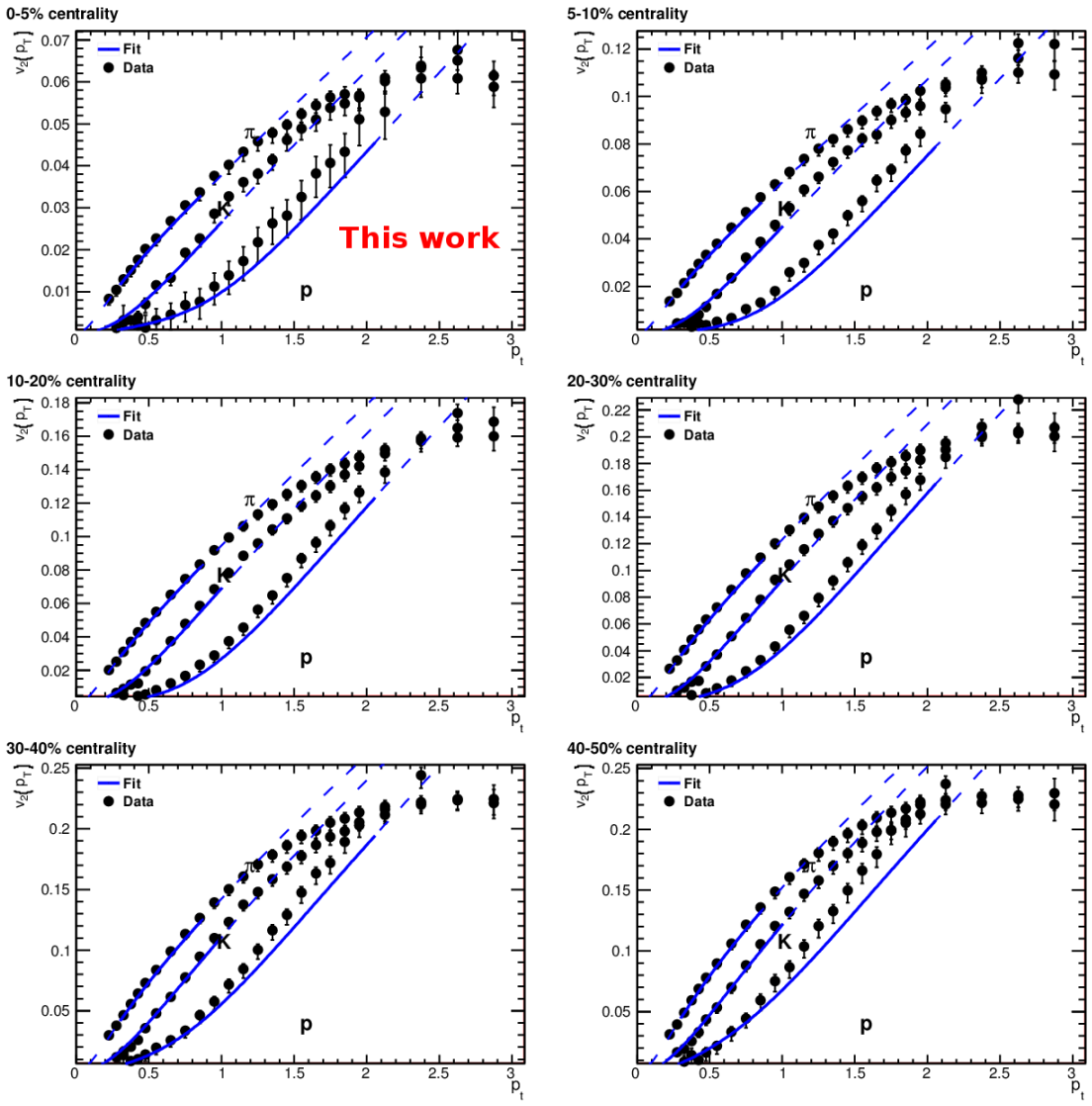

Figure 7.2: Fits of the elliptic flow of kaons, protons and pions from Pb–Pb at $\sqrt{s_{NN}}$=2.76 TeV using a blast wave integral; dashed lines prolongate the fit function outside of the fitting domain. Black points from [30]

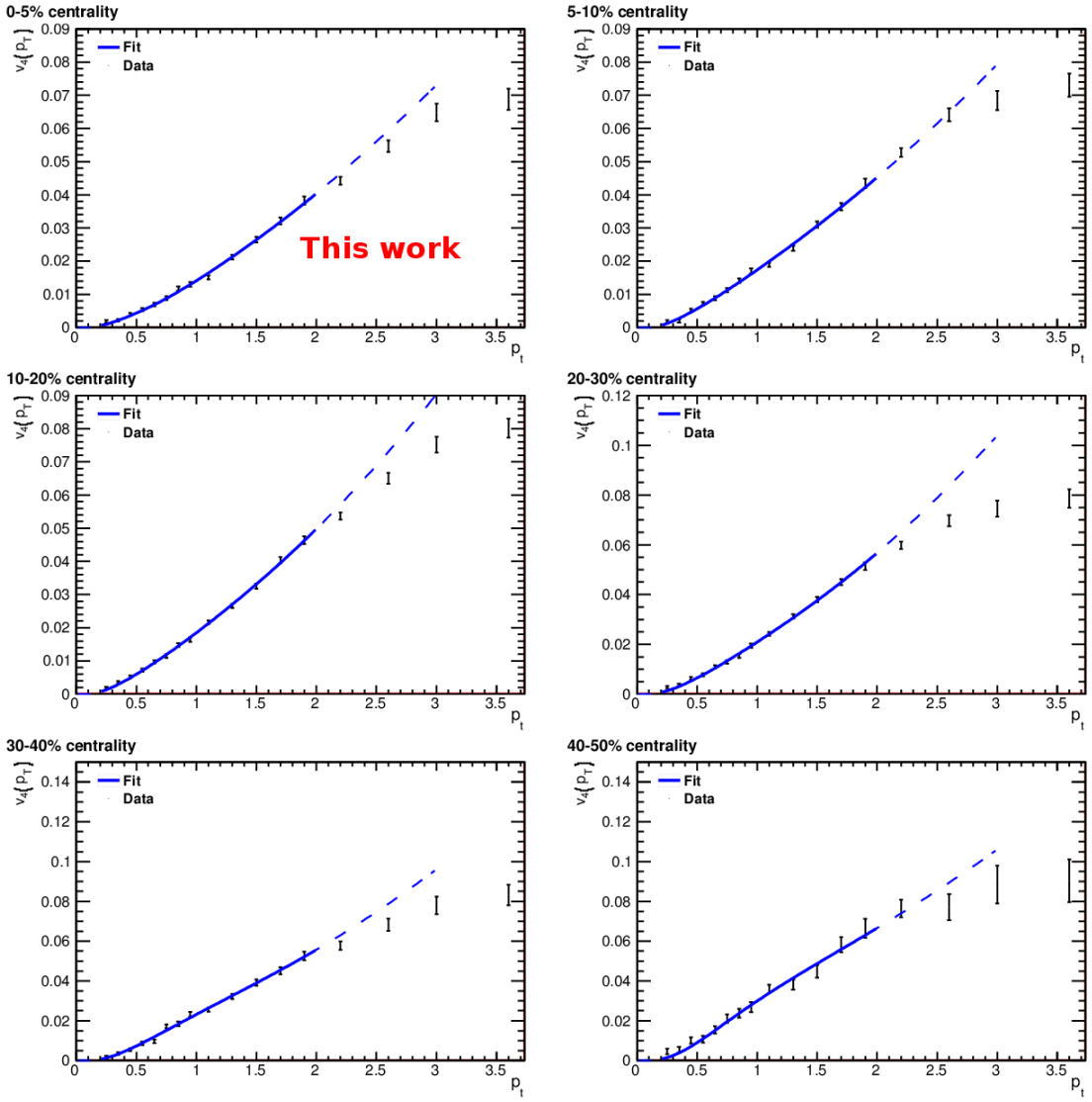

Figure 7.3: Fits of the elliptic flow of unidentified charged particles from Pb–Pb at $\sqrt{s_{NN}}$=2.76 TeV using a blast wave integral (using pion, kaon and proton mass with abundacy weights); dashed lines prolongate the fit function outside of the fitting domain. Black points from [31]

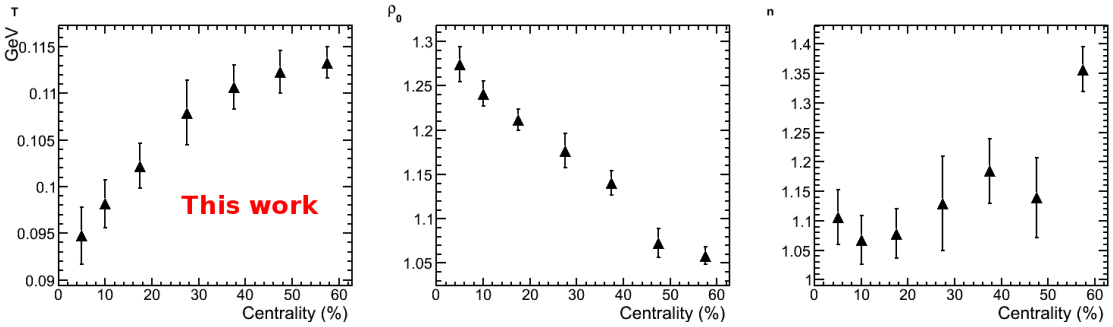

Figure 7.4: Parameters from Tables 7.1 to 7.6, obtained from fits of published identified particles (π, K, p) spectra and v_2.

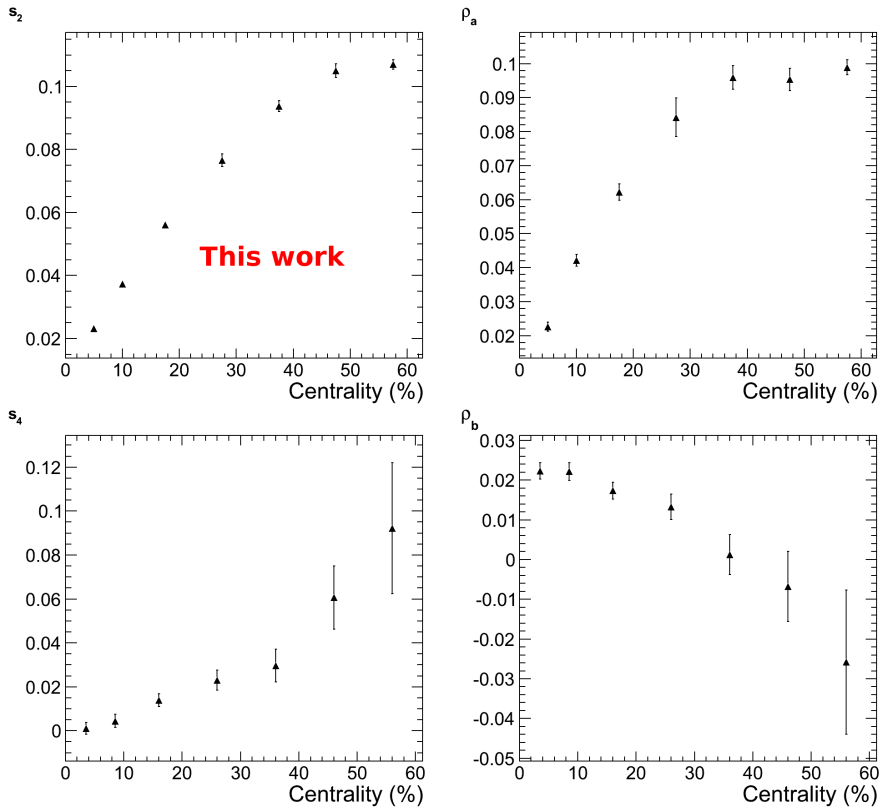

Figure 7.5: Parameters from Tables 7.1 to 7.6, obtained from fits of published charged (unidentified) particles v_4.

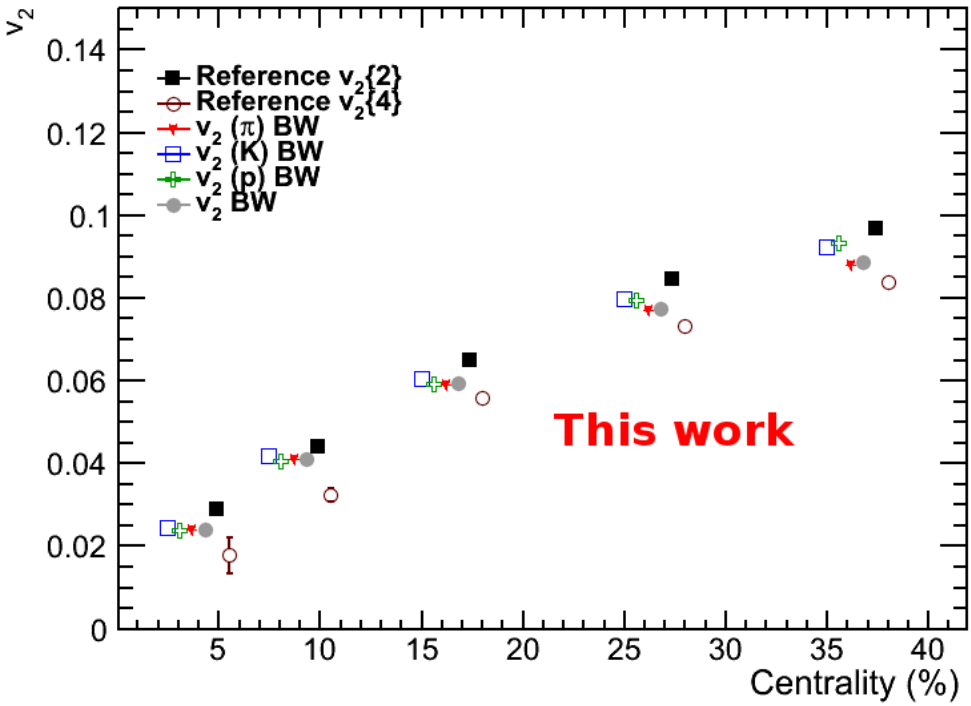

Figure 7.6: Reference $v_2\{2\}$ and $v_4\{2\}$ from [32] (ALICE Pb-Pb $\sqrt{s_{NN}} = 2.76$ TeV) compared with reference v_2 recalculated from the blast wave integral with the fitted parameters.

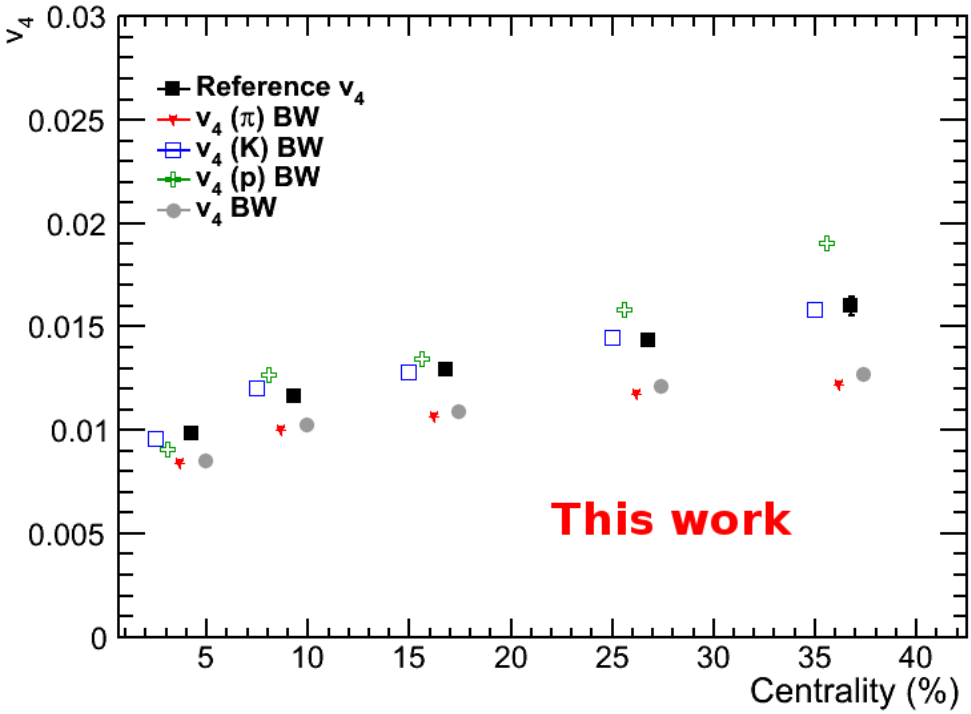

Figure 7.7: Reference $v_4\{2\}|\Delta\eta > 1|$ from [33] (ALICE Pb-Pb $\sqrt{s_{NN}} = 2.76$ TeV) compared with reference v_4 recalculated from the blast wave integral with the fitted parameters.

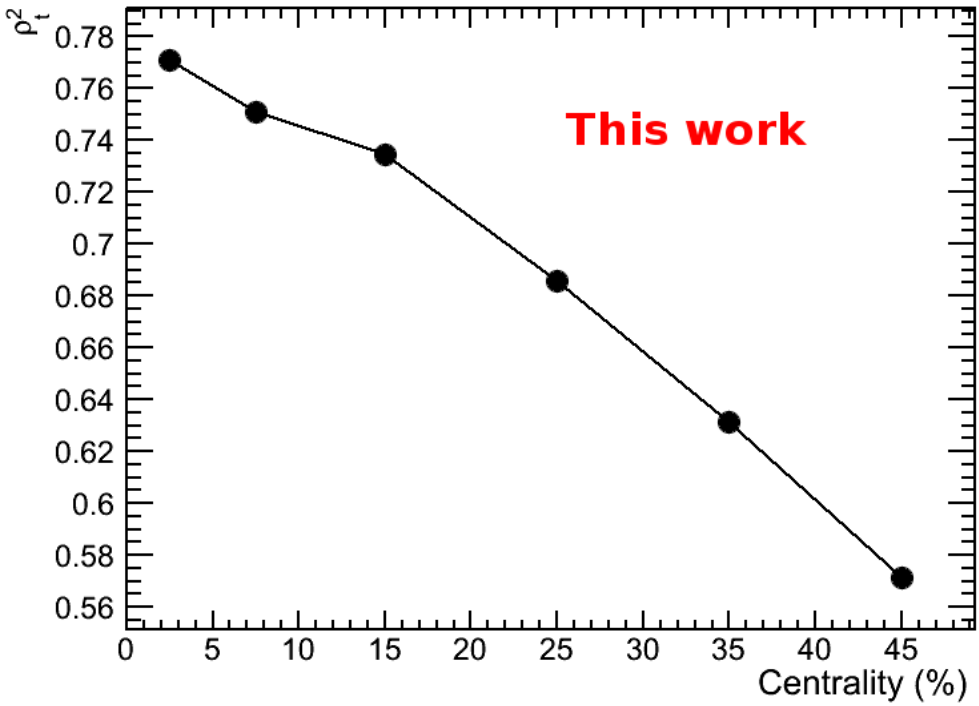

Figure 7.8: $\langle \rho_t^2 \rangle$ calculated from the blast wave integral. This corresponds to the magnitude of the transversal collective "push"

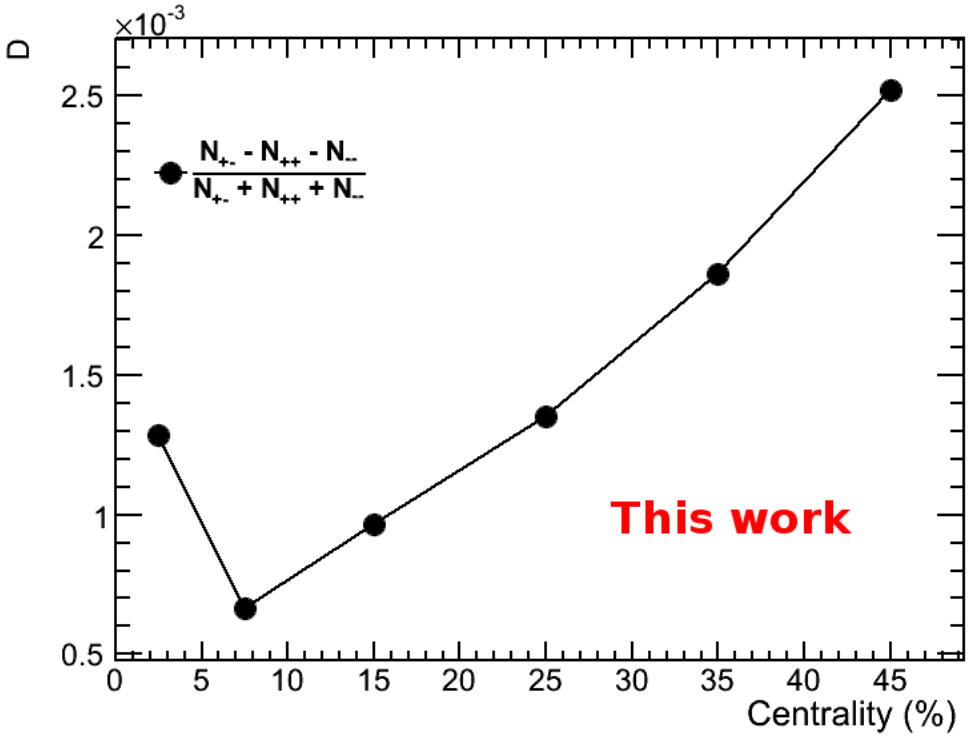

Figure 7.9: Dilution factor calculated from Equation 7.11 using Pb-Pb data at $\sqrt{s_{NN}} = 2.76$ TeV

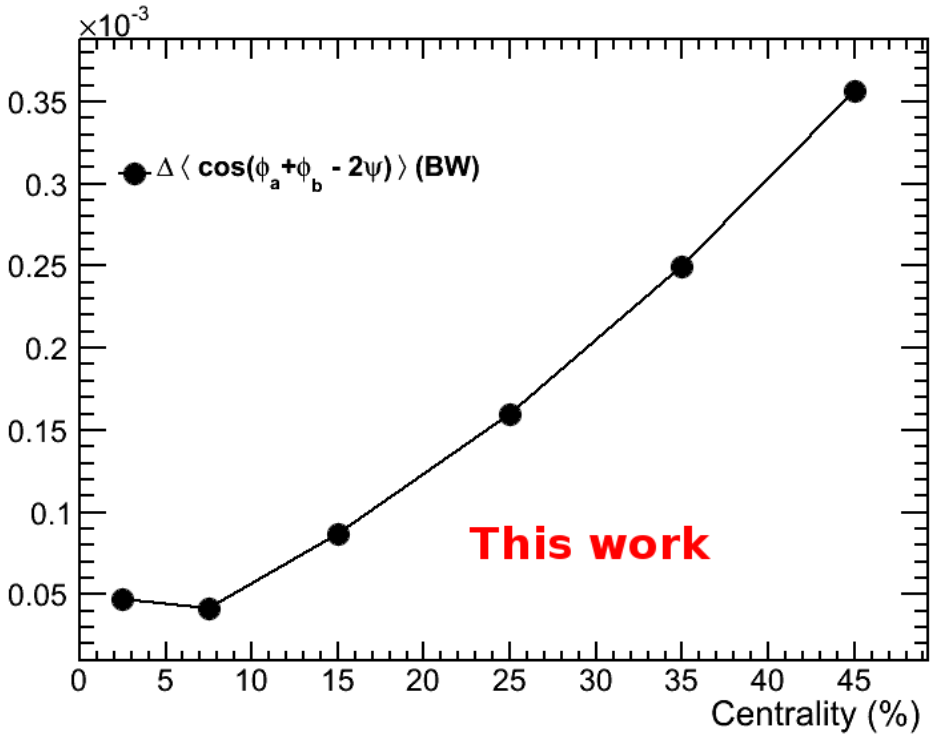

Figure 7.10: Second harmonic correlator with respect to the reaction plane, calculated using the blast wave integrals.

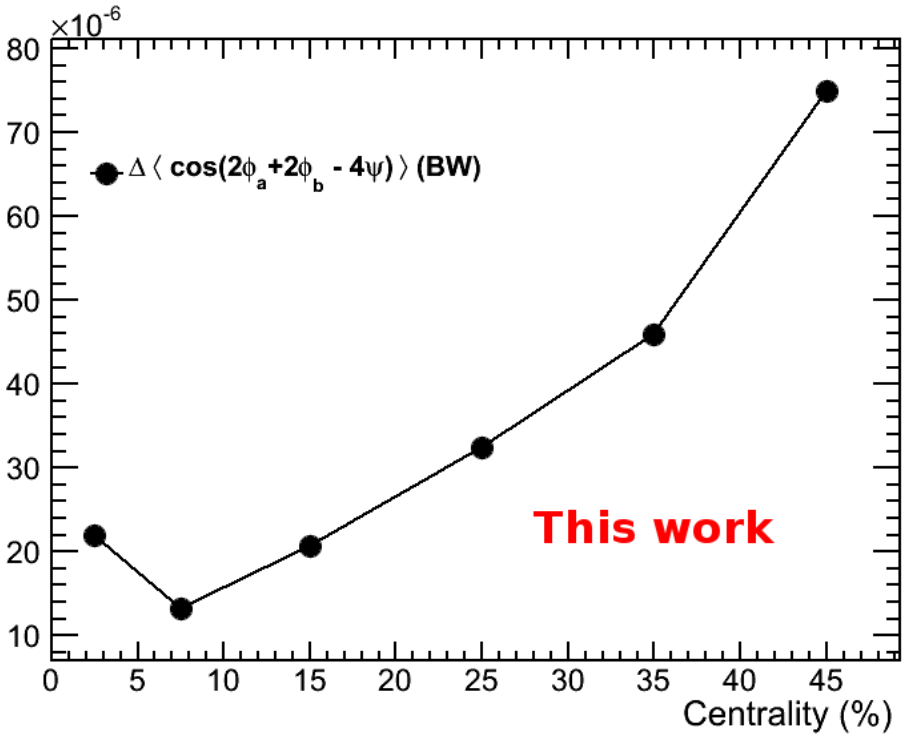

Figure 7.11: Fourth harmonic correlator with respect to the reaction plane, calculated using the blast wave integrals.

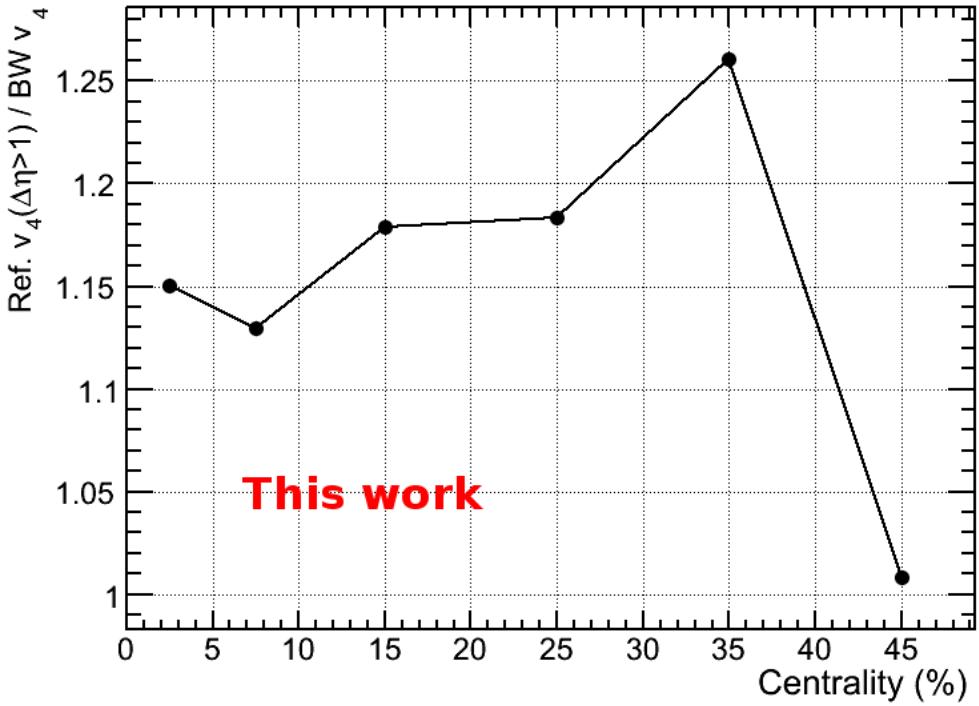

Figure 7.12: Ratio of the reference v_4 recalculated using the blast wave integral and the reference $v_4\{2\}$ from ALICE data from [33] (Pb–Pb, $\sqrt{s_{NN}} = 2.76$ TeV).

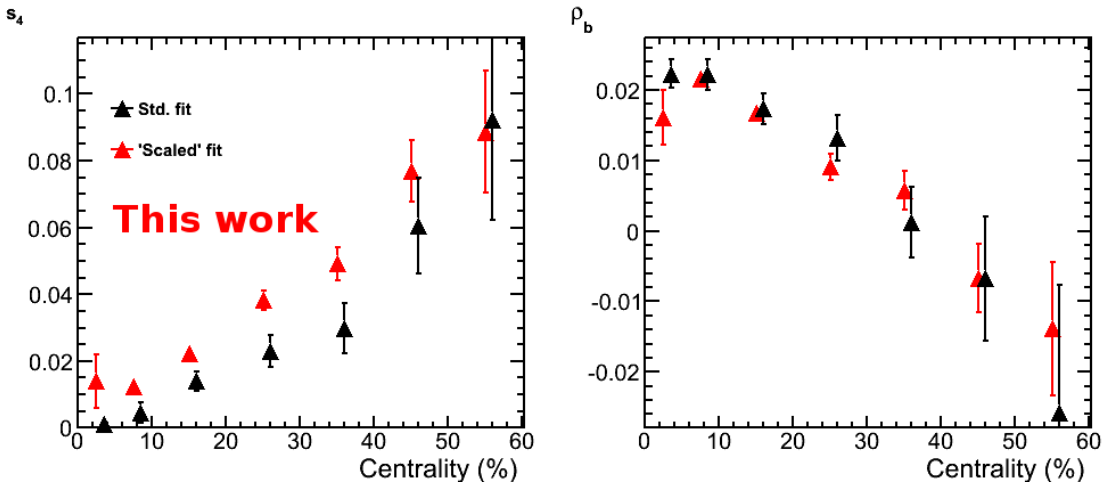

Figure 7.13: Anisotropy parameters obtained from fit v_4 rescaling.

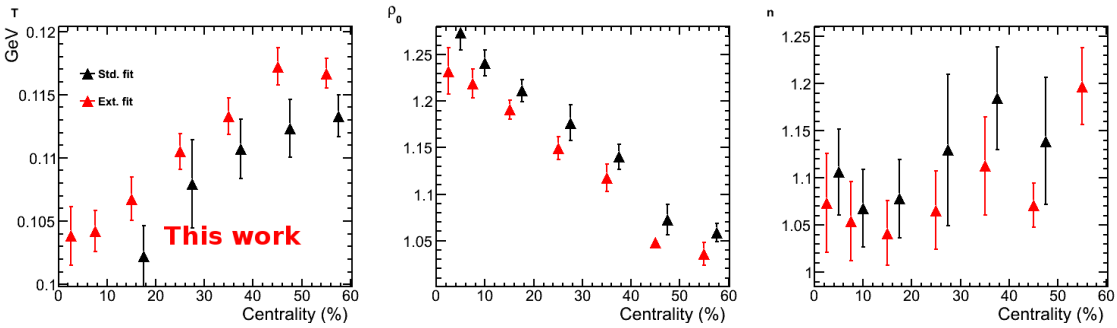

Figure 7.14: Parameters obtained from fit range extension.

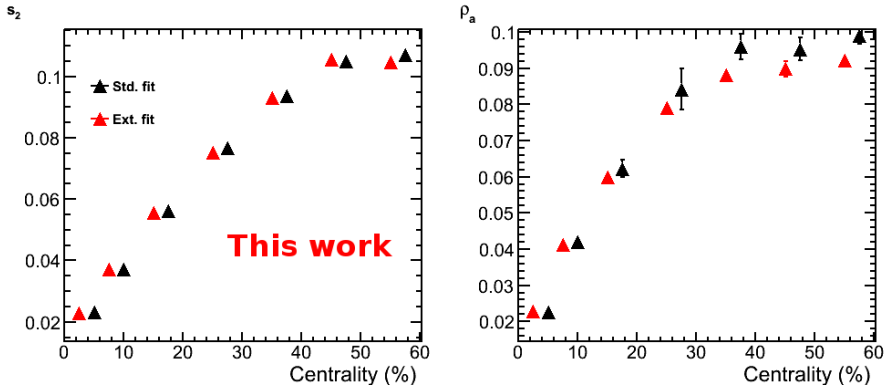

Figure 7.15: Anisotropy parameters obtained from fit range extension.

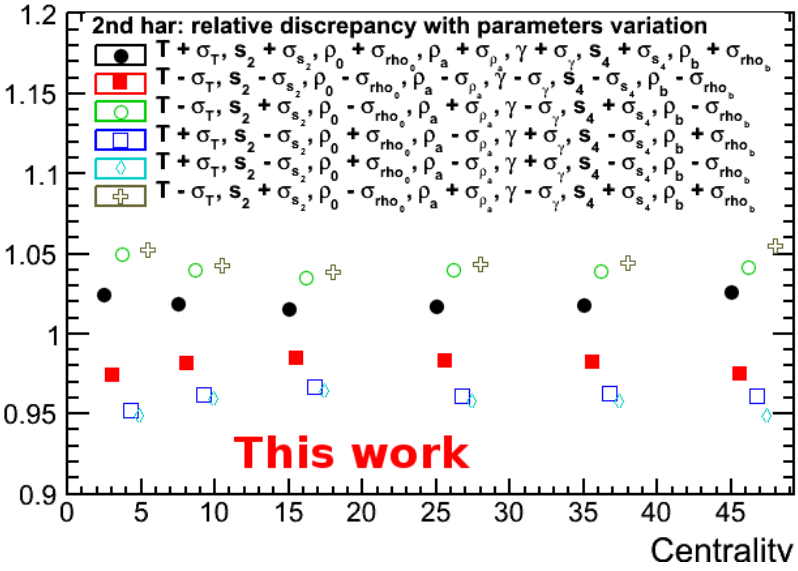

Figure 7.16: Relative discrepancy from the main blast wave value (second harmonic correlator)for various variations of the parameters.

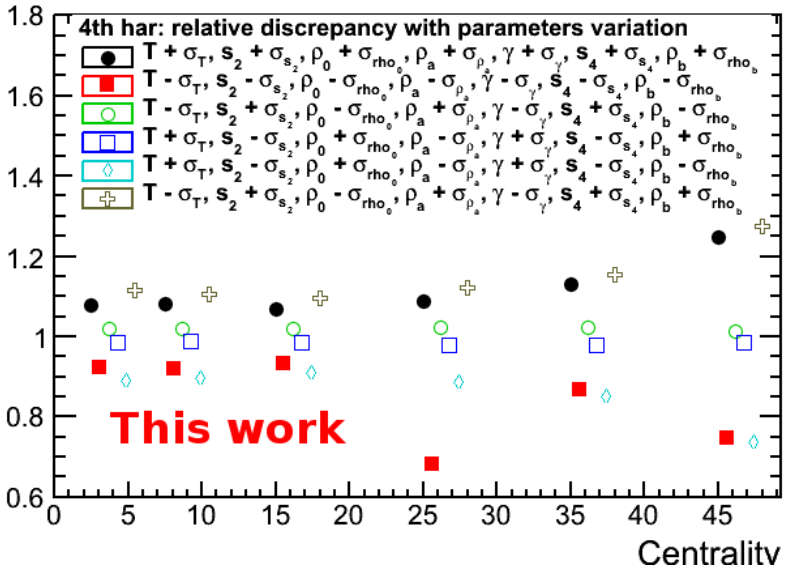

Figure 7.17: Relative discrepancy from the main blast wave value (fourth harmonic correlator)for various variations of the parameters.

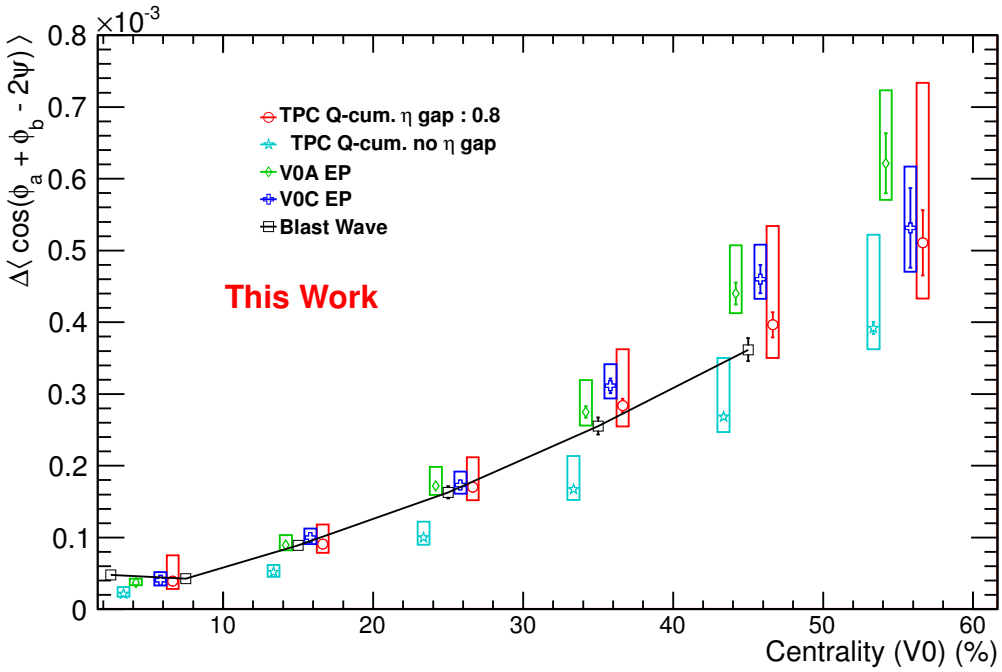

Figure 7.18: Comparison of the second harmonic correlators obtained from the VZERO EP method, TPC Q-Cumulants method with pseudorapidity gaps and blast wave predictions.

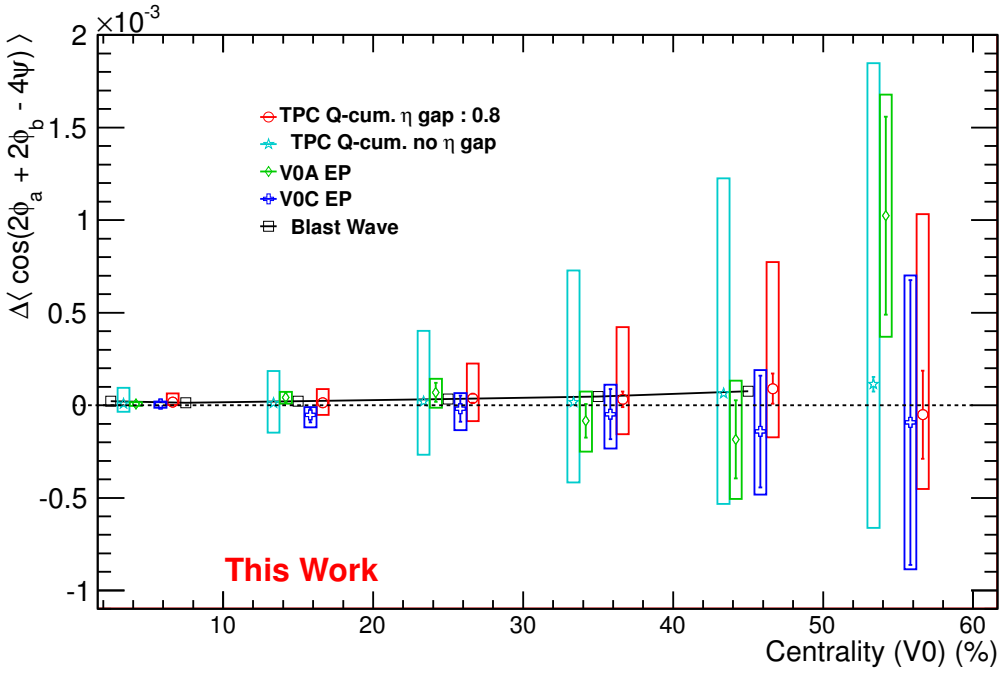

Figure 7.19: Comparison of the fourth harmonic correlators obtained from the VZERO EP method, TPC Q-Cumulants method with pseudorapidity gaps and blast wave predictions.

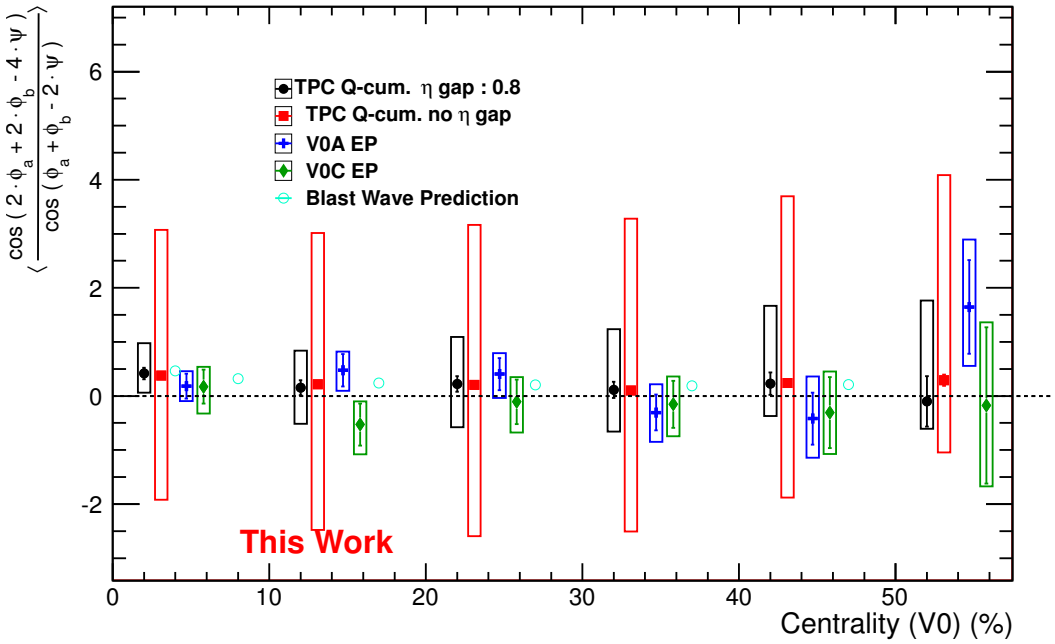

Figure 7.20: Comparison of the ratios of the fourth to second harmonic correlators obtained from the VZEROA and VZEROC EP, TPC Q-Cumulants method with pseudorapidity gaps and blast wave predictions. Wide vertical bars represent combined statistical and systematic errors.

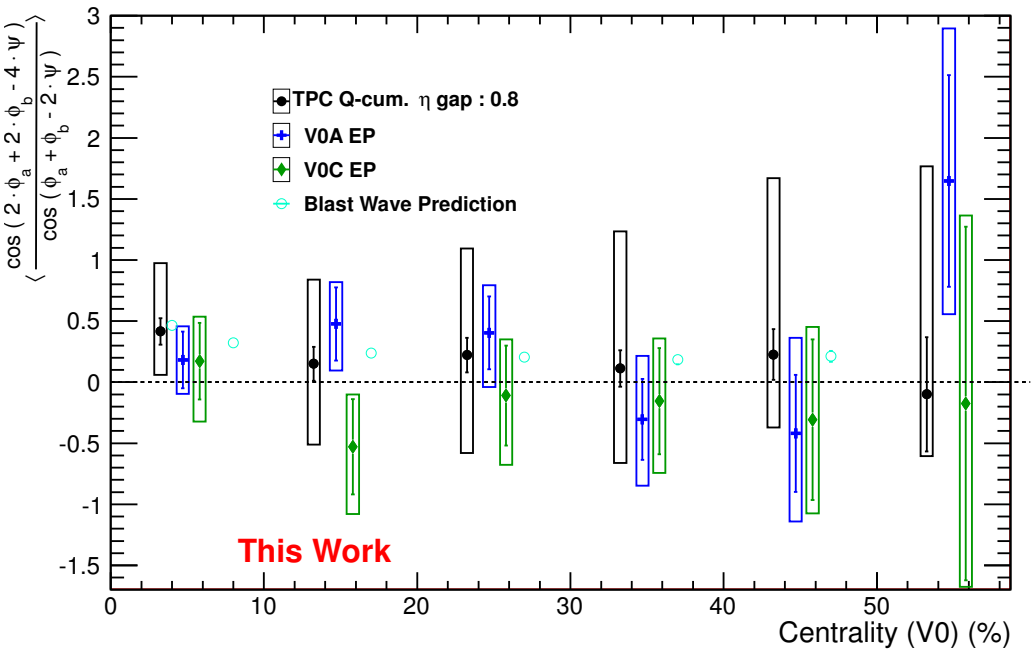

Figure 7.21: Comparison of the ratios of the fourth to second harmonic correlators obtained from the VZEROA and VZEROC EP, TPC Q-Cumulants method with pseudorapidity gaps and blast wave predictions. These results are identical to Figure 7.20 with magnification added for clarity. Wide vertical bars represent combined statistical and systematic errors.

Chapter 8

Summary and Conclusion

In this thesis, we have reported results of the charge-dependence of the second and fourth harmonic correlators $\Delta\langle\cos(\phi_a + \phi_b - 2\psi)\rangle$ and $\Delta\langle\cos(2\phi_a + 2\phi_b - 4\psi)\rangle$ and their ratio, calculated using data collected from Pb-Pb collisions at $\sqrt{s_{NN}} = 2.76$ TeV measured by the ALICE experiment. The charge-dependence of the second harmonic correlator is sensitive to the Chiral Magnetic Effect, a phenomenon in which the combination of possible local strong parity violation with the strong magnetic field perpendicular to the reaction place manifest itself as an anisotropy in the charged pion distribution with respect to that reaction plane. The combination of balancing charge pair creation with the collimation from anisotropic flow, called local charge conservation, contributes to both the second and fourth harmonic correlator charge dependences. The measurement of the fourth harmonic correlator charge-depedence can be used to estimate the contribution of the local charge conservation to the second harmonic. The results shown in this thesis are based on a Q-Vector method applied to TPC tracks, using a pseudorapidity gap to reduce the charge-dependence on the reference particles. The same-charge second harmonic correlators show a strong signal while the opposite-charge second harmonic correlators are significantly smaller up to 40% centrality, similarly to previously published results. Same- and opposite-charge fourth harmonic correlators have similar values with their difference consistent with zero, within statistical errors.

These results are compared with a blast wave model calculation of the charge-dependence of the fourth and second harmonic correlators, using parameters obtained from fits of charged particles spectra and second and fourth order flow coefficients. The ratio of the charge de-

pendence of the fourth and second harmonic correlators obtained from data has also been compared to the corresponding blast wave model calculation. These results are consistent with each other, but the large errors associated with the results obtained from data prevent us from drawing a definitive conclusion concerning the magnitude of local charge conservation. The systematical errors affecting the results obtained from Q-Vector calculations are dominated by the effects of the particle selection variation. Future analysis could achieve a significant reduction of these systematical errors using different selection cuts which lower the sensitivity of the correlators to a variation of the cuts' criteria. The results obtained using the VZERO event plane method have lower systematical errors, but the statistical errors that propagate from the fourth order event plane resolution are large due to the geometry of this detector. A different choice of forward rapidity detector, such as the ZDC, could provide a fourth order event plane with a better resolution while conserving a large pseudorapidity gap between reference and flow particles, which is necessary to remove the charge-dependent correlations between them. While an increase in the amount of data analyzed by this method could also improve these results, the number of collisions required to reduce the statistical errors by a large enough factor is significantly greater than the currently available 2010 and 2011 Pb-Pb data.

REFERENCES

[1] Go on a particle quest at the first cern webfest. `http://cds.cern.ch/record/1473657`.

[2] Origin of the elements. `http://www.lbl.gov/abc/wallchart/chapters/10/0.html`.

[3] Frithjof Karsch. Lattice results on QCD thermodynamics. *Nucl. Phys.*, A698:199–208, 2002.

[4] M.M. Aggarwal et al. An Experimental Exploration of the QCD Phase Diagram: The Search for the Critical Point and the Onset of De-confinement. 2010.

[5] Thomas Schäfer. Nearly perfect fluidity. *Physics*, 2:88, Oct 2009.

[6] Michal P. Heller, Romuald A. Janik, and R. Peschanski. Hydrodynamic Flow of the Quark-Gluon Plasma and Gauge/Gravity Correspondence. *Acta Phys.Polon.*, B39:3183–3204, 2008.

[7] The sound of the little bangs. `http://www.bnl.gov/rhic/inside/news.php?a=21795`.

[8] Bedangadas Mohanty. Exploring the QCD landscape with high-energy nuclear collisions. *New J.Phys.*, 13:065031, 2011.

[9] Raimond Snellings. Elliptic Flow: A Brief Review. *New J. Phys.*, 13:055008, 2011.

[10] C. Adler et al. Identified particle elliptic flow in Au + Au collisions at $\sqrt{s_{NN}} = 130$-GeV. *Phys. Rev. Lett.*, 87:182301, 2001.

[11] B.I. Abelev et al. Mass, quark-number, and $\sqrt{s_{NN}}$ dependence of the second and fourth flow harmonics in ultra-relativistic nucleus-nucleus collisions. *Phys. Rev.*, C75:054906, 2007.

[12] J. Adams et al. Transverse momentum and collision energy dependence of high p(T) hadron suppression in Au+Au collisions at ultrarelativistic energies. *Phys. Rev. Lett.*, 91:172302, 2003.

[13] J. Adams et al. Evidence from d + Au measurements for final state suppression of high p(T) hadrons in Au+Au collisions at RHIC. *Phys. Rev. Lett.*, 91:072304, 2003.

[14] G.S. Bali, F. Bruckmann, G. Endrodi, Z. Fodor, S.D. Katz, et al. The chiral magnetic effect from lattice QCD. 2014.

[15] Local strong parity violation and new perspectives in the experimental study of non-perturbative qcd. http://www.bnl.gov/rhic/inside/news.php?a=21588.

[16] Harmen Warringa. The chiral magnetic effect. http://staff.science.uva.nl/~sewm08/slides/warringa.pdf.

[17] Introduction to the large hadron collider at cern. http://sites.uci.edu/energyobserver/2012/11/28/introduction-to-the-large-hadron-collider-at-cern-2/.

[18] The alice experiment. http://aliceinfo.cern.ch/Public/en/Chapter2/Chap2InsideAlice-en.html.

[19] The present inner tracking system: Steps forward! http://alicematters.web.cern.ch/?q=ALICE_currentITS.

[20] Giacomo Contin. The Silicon Strip Detector (SSD) for the ALICE experiment at LHC: construction, characterization and charged particles multiplicity studies.

[21] The alice time projection chamber (tpc).

[22] B Cheynis. ALICE Vzero Detector. Sep 2013.

[23] F Carminati et al. ALICE: Physics performance report, volume I. *J.Phys.*, G30:1517–1763, 2004.

[24] Chiara Zampolli, Federico Carminati, and Alberto Colla. The shuttle: The ALICE framework for the extraction of the conditions data. *PoS*, ACAT2010:066, 2010.

[25] Alberica Toia. Bulk Properties of Pb-Pb collisions at $\sqrt{s_{NN}} = 2.76$ TeV measured by ALICE. *J.Phys.*, G38:124007, 2011.

[26] The analysis framework. http://aliweb.cern.ch/Offline/Activities/Analysis/AnalysisFramework/index.html.

[27] Aliroot documentation. http://aliweb.cern.ch/Offline/AliRoot/Manual.html.

[28] Panos Christakoglou. Charge dependent azimuthal correlations in Pb–Pb collisions at $\sqrt{s_{NN}} = 2.76$ TeV. *J. Phys.*, G38:124165, 2011.

[29] Roberto Preghenella. Identified-particle production and spectra with the ALICE detector in pp and Pb-Pb collisions at the LHC. *Acta Phys.Polon.*, B43:555, 2012.

[30] Mikolaj Krzewicki. Elliptic and triangular flow of identified particles at ALICE. *J.Phys.*, G38:124047, 2011.

[31] Betty Abelev et al. Anisotropic flow of charged hadrons, pions and (anti-)protons measured at high transverse momentum in Pb-Pb collisions at $\sqrt{s_{NN}}$=2.76 TeV. *Phys.Lett.*, B719:18–28, 2013.

[32] K Aamodt et al. Elliptic flow of charged particles in Pb-Pb collisions at 2.76 TeV. *Phys.Rev.Lett.*, 105:252302, 2010.

[33] K. Aamodt et al. Higher harmonic anisotropic flow measurements of charged particles in Pb-Pb collisions at $\sqrt{s_{NN}}$=2.76 TeV. *Phys.Rev.Lett.*, 107:032301, 2011.

[34] Jonathan L. Rosner. The Standard model in 2001. pages 1–56, 2001.

[35] Katherine Brading and Harvey R. Brown. Noether's theorems and gauge symmetries. 2000.

[36] Murray Gell-Mann. A Schematic Model of Baryons and Mesons. *Phys.Lett.*, 8:214–215, 1964.

[37] Francois Gelis, Tuomas Lappi, and Raju Venugopalan. High energy scattering in Quantum Chromodynamics. *Int.J.Mod.Phys.*, E16:2595–2637, 2007.

[38] Dmitri Diakonov. Foundations of the constituent quark model. *Prog.Part.Nucl.Phys.*, 36:1–18, 1996.

[39] M.Y. Han and Yoichiro Nambu. Three Triplet Model with Double SU(3) Symmetry. *Phys.Rev.*, 139:B1006–B1010, 1965.

[40] Chen-Ning Yang and Robert L. Mills. Conservation of Isotopic Spin and Isotopic Gauge Invariance. *Phys.Rev.*, 96:191–195, 1954.

[41] Y. Sumino. QCD potential as a 'Coulomb plus linear' potential. *Phys.Lett.*, B571:173–183, 2003.

[42] H. David Politzer. Asymptotic Freedom: An Approach to Strong Interactions. *Phys.Rept.*, 14:129–180, 1974.

[43] C.A. Dominguez and M. Loewe. Deconfinement and Chiral Symmetry Restoration at Finite Temperature. *Phys.Lett.*, B233:201, 1989.

[44] N. Cabibbo and G. Parisi. Exponential Hadronic Spectrum and Quark Liberation. *Phys.Lett.*, B59:67–69, 1975.

[45] John C. Collins and M.J. Perry. Superdense Matter: Neutrons Or Asymptotically Free Quarks? *Phys.Rev.Lett.*, 34:1353, 1975.

[46] M.A. Stephanov. QCD phase diagram: An Overview. *PoS*, LAT2006:024, 2006.

[47] Ulrich W. Heinz and Gregory Kestin. Jozso's Legacy: Chemical and Kinetic Freeze-out in Heavy-Ion Collisions. *Eur.Phys.J.ST*, 155:75–87, 2008.

[48] Yadav Pandit. Azimuthal Anisotropy in U+U Collisions at $\sqrt{s_{NN}}$ = 193 GeV with STAR Detector at RHIC. *J.Phys.Conf.Ser.*, 458:012003, 2013.

[49] Yadav Pandit. Azimuthal Anisotropy in U+U Collisions at $\sqrt{s_{NN}}$ = 193 GeV with STAR Detector at RHIC. *J.Phys.Conf.Ser.*, 458:012003, 2013.

[50] Gang Wang. Search for Chiral Magnetic Effects in High-Energy Nuclear Collisions. *Nucl.Phys.A904-905*, 2013:248c–255c, 2013.

[51] J.D. Bjorken. Highly Relativistic Nucleus-Nucleus Collisions: The Central Rapidity Region. *Phys.Rev.*, D27:140–151, 1983.

[52] B.I. Abelev et al. Systematic Measurements of Identified Particle Spectra in pp, d^+ Au and Au+Au Collisions from STAR. *Phys.Rev.*, C79:034909, 2009.

[53] A. Andronic, P. Braun-Munzinger, and J. Stachel. Hadron production in central nucleus-nucleus collisions at chemical freeze-out. *Nucl.Phys.*, A772:167–199, 2006.

[54] Peter Braun-Munzinger, Krzysztof Redlich, and Johanna Stachel. Particle production in heavy ion collisions. 2003.

[55] Arthur M. Poskanzer and S.A. Voloshin. Methods for analyzing anisotropic flow in relativistic nuclear collisions. *Phys. Rev.*, C58:1671–1678, 1998.

[56] K. Dusling and D. Teaney. Simulating elliptic flow with viscous hydrodynamics. *Phys.Rev.*, C77:034905, 2008.

[57] Raphael Granier de Cassagnac. J / psi production in PHENIX. *Eur.Phys.J.*, C49:365–369, 2007.

[58] C.S. Wu, E. Ambler, R.W. Hayward, D.D. Hoppes, and R.P. Hudson. Experimental Test of Parity Conservation in Beta Decay. *Phys.Rev.*, 105:1413–1414, 1957.

[59] T.D. Lee and Chen-Ning Yang. Question of Parity Conservation in Weak Interactions. *Phys.Rev.*, 104:254–258, 1956.

[60] Dmitri Kharzeev. Parity violation in hot QCD: Why it can happen, and how to look for it. *Phys.Lett.*, B633:260–264, 2006.

[61] Kenji Fukushima, Dmitri E. Kharzeev, and Harmen J. Warringa. The Chiral Magnetic Effect. *Phys.Rev.*, D78:074033, 2008.

[62] Dmitri E. Kharzeev, Larry D. McLerran, and Harmen J. Warringa. The Effects of topological charge change in heavy ion collisions: 'Event by event P and CP violation'. *Nucl.Phys.*, A803:227–253, 2008.

[63] Sergei A. Voloshin. Parity violation in hot QCD: How to detect it. *Phys.Rev.*, C70:057901, 2004.

[64] Soren Schlichting and Scott Pratt. Charge conservation at energies available at the BNL Relativistic Heavy Ion Collider and contributions to local parity violation observables. *Phys.Rev.*, C83:014913, 2011.

[65] Sergei A. Voloshin. Transverse radial expansion in nuclear collisions and two particle correlations. *Phys.Lett.*, B632:490–494, 2006.

[66] Scott Pratt. Alternative Contributions to the Angular Correlations Observed at RHIC Associated with Parity Fluctuations. 2010.

[67] B Alessandro, R Bala, G Batigne, S Beolé, E Biolcati, P Cerello, S Coli, Y Corrales Morales, E Crescio, P De Remigis, D Falchieri, G Giraudo, P Giubellino, R Lea, A Marzari Chiesa, M Masera, G Mazza, G Ortona, F Prino, L Ramello, A Rashevsky, L Riccati, A Rivetti, S Senyukov, M Siciliano, M Sitta, M Subieta, L Toscano, and F Tosello. Charge collection in the silicon drift detectors of the alice experiment. *Journal of Instrumentation*, 5(02):P02008, 2010.

[68] Alice offline bible. `http://aliweb.cern.ch/secure/Offline/sites/aliweb.cern.ch.Offline/files/uploads/OfflineBible.pdf`.

[69] Monalisa. `http://alimonitor.cern.ch/map.jsp`.

[70] Nicolas Borghini, Phuong Mai Dinh, and Jean-Yves Ollitrault. Flow analysis from multiparticle azimuthal correlations. *Phys. Rev.*, C64:054901, 2001.

[71] Ante Bilandzic, Raimond Snellings, and Sergei Voloshin. Flow analysis with cumulants: Direct calculations. *Phys. Rev.*, C83:044913, 2011.

[72] B.I. Abelev et al. Azimuthal Charged-Particle Correlations and Possible Local Strong Parity Violation. *Phys. Rev. Lett.*, 103:251601, 2009.

[73] Fabrice Retière and Michael Annan Lisa. Observable implications of geometrical and dynamical aspects of freeze-out in heavy ion collisions. *Phys. Rev.*, C70:044907, Oct 2004.

[74] Sergei A. Voloshin. Transverse radial expansion in nuclear collisions and two particle correlations. *Phys. Lett.*, B632:490–494, 2006.

ABSTRACT

MULTIPARTICLE CORRELATIONS IN PB–PB COLLISIONS AT $\sqrt{s_{NN}}$=2.76 TEV

by

JOCELYN MLYNARZ

May 2014

Advisor: Dr. Sergei A. Voloshin

Major: Physics

Degree: Doctor of Philosophy

Quantum Chromodynamics, which describes the interactions of quarks and gluons, has been found not to violate global parity symmetry. However, the possibility of local parity violations due to quark interactions with topologically non-trivial gluonic fields is not excluded. The effects of these parity violations could be measured in the hot and dense medium created in the ultrarelativistic heavy ion collisions experiment conducted at the Large Hadron Collider, called a Quark-Gluon Plasma, in which the quarks that compose most of ordinary matter are deconfined. In the strong magnetic fields which permeate the QGP in non-central collisions, parity violation would express itself as a charge asymetry with respect to the reaction plane, a phenomenon called the Chiral Magnetic Effect. The measurements of the charge-dependent correlations in a heavy-ion collisions allow to experimentally probe effects of the CME. These measurements are conducted via the use of the second harmonic two-particle correlator with respect to the reaction plane, $\langle\cos(\phi_a+\phi_b-2\psi)\rangle$. The background affecting these measurements is the consequence of an interplay of strong anisotropic flow and correlations unrelated to the CME. Correlations with respect to the fourth harmonic, $\langle\cos(2\phi_a+2\phi_b-4\psi)\rangle$, are insensitive to the CME and can be used to estimate the magnitude of these background effects. In this thesis, we present results from charge-dependent correlations with

respect to both the second and fourth harmonic event planes measured in Pb+Pb collisions at $\sqrt{s_{NN}} = 2.76$ TeV at the LHC using data from the ALICE detector. We also present the ratio of the fourth to second harmonic correlators, and compare it to calculations based on the blast wave model which serve as a baseline to understand how these background effects scale between one harmonic and another.

AUTOBIOGRAPHICAL STATEMENT

2000-2003	Classe Preparatoire aux Grande Ecoles Marcelin Berthelot, MPSI/MP
2003-2007	Master's Degree in Electronics and Nuclear Engineering at Ecole Nationale Superieure d'Ingenieurs de Caen (ENSI-Caen)
2006-2007	Master's Degree in Nuclear Physics at University of Caen-Basse Normandie
2008-2013	Graduate Research Assistant and Graduate Teaching Assistant at Wayne State University